Femtosecond pulse generation in solid-state lasers

by

Malini Paye

S.B., Massachusetts Institute of Technology (1990)
S.M., Massachusetts Institute of Technology (1990)

Submitted to the Department of Electrical Engineering
in partial fulfillment of the requirements for the degree of

Doctor of Philosophy

at the

MASSACHUSETTS INSTITUTE OF TECHNOLOGY

September 1994

© Malini Paye, 1994

The author hereby grants to MIT permission to reproduce and
to distribute copies of this thesis document in whole or in part.

Signature of Author .....
Department of Electrical Engineering
July 15, 1994

Certified by .....
James G. Fujimoto
Professor of Electrical Engineering
Thesis Supervisor

Accepted by .....
Frederic R. Morgenthaler
Chairman, Departmental Committee on Graduate Students

WITHDRAWN
FROM
MIT LIBRARIES

Femtosecond pulse generation in solid-state lasers

by

Malini Paye

Submitted to the Department of Electrical Engineering
on July 15, 1994, in partial fulfillment of the
requirements for the degree of
Doctor of Philosophy

Abstract

Femtosecond laser technology has seen rapid advances over the last five years due to the emergence of reliable, broad-band solid-state laser media in particular the Ti:sapphire gain medium. This thesis deals with various aspects of femtosecond pulse generation in solid-state lasers, with particular emphasis on the Ti:sapphire laser system.

A novel passive modelocking technique called Microdot mirror modelocking was implemented. It is a passive, all-solid-state, intracavity modelocking mechanism based on self-focussing due to the Kerr nonlinearity. This technique was applied to the modelocking of a medium power, laser-pumped Ti:sapphire system, to produce 190fs pulses. It was also extended to a higher power, arc-lamp-pumped Nd:YLF laser system to produce 2.3 ps pulses.

A numerical procedure for modeling the nonlinear behaviour of resonators was implemented. This iterative procedure solves for self-consistent nonlinear resonator modes using a description of self-focussing as a nonlinear scaling of the Gaussian beam q parameter. It was used to provide an exemplary, intuitive understanding of nonlinear effects in a simple resonator closely related to the high-repetition rate femtosecond source that was subsequently implemented.

A novel, compact, femtosecond, Kerr Lens Modelocked laser geometry was designed and implemented. 111 fs pulses were produced from a Ti:sapphire oscillator at a repetition rate of 1 GHz and 54 fs pulses at a repetition rate of 385 MHz. To realize this source, a novel method for dispersion compensation was conceived, analyzed and implemented. Negative dispersion was shown to be achievable using resonator geometries that enforce the spatial separation of propagation axes corresponding to monochromatic Gaussian modes that compose the total broad-band beam in a femtosecond oscillator. This work serves to demonstrate the scalability of Kerr lens modelocking techniques to very high repetition rates. The compact, high-repetition rate source has important implications for the construction of practical and reliable femtosecond laser systems.

Finally a femtosecond cavity-dumped, Kerr lens modelocked Ti:Sapphire laser was also implemented. The method of cavity-dumping was demonstrated as a viable technique for the generation of intermediate energy, femtosecond pulses at variable

repetition rates. 100 nJ, 50 fs pulses are generated at variable repetition rates as high as 1 MHz. The cavity dumped, Kerr-lens-modelocked source is an important alternative to more complex and expensive, high-energy, relatively low repetition-rate schemes for amplifying pulses from Ti:Al_2O_3 lasers.

Thesis Supervisor: James G. Fujimoto
Title: Professor of Electrical Engineering

Acknowledgements

I have long awaited the moment when I would sit down to write the acknowledgments to my doctoral thesis! This has been a long and challenging journey during which so many have helped me in so many ways. It is certainly a delight to have this opportunity to say just a few words of thanks.

I thank my advisor Professor James Fujimoto, for giving me the opportunity to work in one of the world's most prestigious femtosecond laser laboratories. His dedication to his work and the intensity of his efforts are truly extraordinary and I have learnt a great deal through my acquaintance with him. I would like to thank Professors Erich Ippen and Hermann Haus for their help over the years. In particular I thank Professor Ippen for graciously serving on more than one of my examination committees. Many thanks are also due to Professor Shaoul Ezekiel for serving on my thesis committee. I found his sense of humour and enthusiasm extremely refreshing. I would also like to thank my mentor at AT & T Bell Laboratories, Dr. Wayne Knox, for his concern and friendship. I have benefitted greatly from his advice and experience.

I have had the good fortune to work closely at MIT with several talented individuals, all of whom I am grateful to for their cooperation. I will remember Giusseppe Gabetta as an excellent experimentalist and a spirited individual with whom it was a real pleasure to work. I thank Joe Jacobson for giving me a glimpse of that all-important art of appearing confident in all situations. I would like to thank Joe Izatt for suffering on the Nd:YLF system with me, and Artur Gouveia-Neto for finally liberating me from it by making it work. Thanks are due to Nick Ulman for his help in constructing the cavity-dumped Ti:Sapphire laser and his memorable TTWPITW list that will never cease to delight me. Brett Bouma deserves thanks for discussing and clarifying several experimental and theoretical issues with me.

Many other people in the Optics Group have been a source of friendship over the past years. Keren Bergmen, Steve Cheng and Melissa, Jay Damask, Regula Fluck, Mike Hee, Antonio and Pina Mecozzi, and Chi Kuang Sun - all deserve my thanks for their friendship and support. I thank Cindy Kopf, Mary Aldridge and Donna Gale for their efficiency and organizational skills. I further thank Mary Aldridge for often livening up my afternoons with her ready wit. I also thank all the other members (past and present) of the group whom I have had the pleasure of knowing and spending a few years of my life with on the 3rd floor of building 36!

These years at MIT could not have been the same had it not been for a few wonderful friendships that I have been fortunate enough to develop here. I thank my dear friend Cathryn Shaw who has spent these many years together with me at MIT, for all her support and love. Cathryn, you are an incredible person and a cherished friend. Thank you from the bottom of my heart. I thank Kwabena Mensah Ofori-Tenkorang (John) for his unwavering friendship through my nine years at MIT. John, thank you for always being there when I needed you and for giving me the

good fortune of enjoying such a genuine friendship as the one we share. I thank Mark Andersson for the long-standing friendship we have enjoyed and for the wonderful years we shared together. Mark, I wish you the very best in all of your endeavours. Alice Lapierre has my thanks for her strong and wise views and her excellent and timely advice. Alice, Congratulations! Lynn Roberson has been a true source of counsel and friendship. Lynn, I hope you realize how much you have helped me. Thank you for being such an inspiring and caring person.

I thank my brother Rajan for being an inspiration and for the many times when he has supported and advised me. I also thank him for getting his PhD and thus proving to me that such a feat was not impossible. I thank my sister-in-law Marta, for sharing with me her wonderful sense of the important and her contagious enthusiasm for life. And I must thank my almost-one-year-old nephew, Pablo Ramaswamy, for his incredible charm that never failed to make me forget my thesis each time I held him in my arms.

Like me, my parents have also waited a long time to see this day! It is they who inspired in me the love of knowledge, the spirit of achievement and the belief in God that have sustained me over the last nine years. It is also they who have supported me at every turn, always trying their utmost to understand and help me. This is as much their achievement as it is mine.

Finally, I thank my husband Jérôme for his love, his patience and his wisdom. It is the source of my deepest joy that I have a lifetime over which to express the love and gratitude that I feel for him.

To Appa and Amma

July 15, 1994.

Contents

List of Figures

Chapter 1

Introduction

The invention of the ruby laser [67] in the 1960's signalled the beginning of a fascinating and multifaceted realm of science. The basic and unique properties of a laser source are the high degree of monochromaticity, coherence, directionality and brightness of the light it generates. These unique and useful properties have lead to the proliferation of continuous wave (CW) lasers in a wide variety of fields including communications, manufacture, medicine and spectroscopy [103, 111].

A further property of lasers that has stimulated much research and study over the past fifteen years is their ability to generate pulses of extremely short duration. Short pulses of light have been used as early as the 19th century for flash photography which sought to freeze the motion of rapidly moving objects. For the past three decades, modelocked lasers have been studied as sources of short pulses of light. These pulses have become the primary tool used in the study of ultrafast phenomena in nature [48]. Chemical reactions, semiconductor physics and biological processes are all examples of phenomena that happen on timescales that are too short to be studied using conventional high-speed electronics. Ultrashort pulses are suitable for these studies due to their fine temporal resolution and also their high peak powers which enhance non-linear effects. Recently, medical fields are also beginning to utilize ultrashort pulses for applications that benefit from high peak intensities.

Modelocking, or the coupling of longitudinal laser modes, was first implemented by Hargrove, Fork and Pollack in 1964 [32] when they acousto-optically modelocked a Helium-Neon laser. The first *passively* modelocked ruby laser was invented in 1965 by Mocker and Collins [74]. Actively modelocked continuous wave (CW) Nd:YAG lasers producing pulses in the 50 ps regime [16] and passively modelocked, flash-lamp pumped Nd:glass lasers [15], producing pulses in the 10 ps regime, were then developed and became the most common sources of ultrashort pulses. The next milestone in the field of short pulse generation came with the development of femtosecond CW dye lasers [82]. The passive modelocking of these lasers [45] eventually lead to the development of the Colliding Pulse Modelocked (CPM) dye laser [22, 117], capable of generating pulses as short as 28 fs, in the early 1980s. The shortest pulses ever, 6 fs, were generated in 1987 by external compression of pulses generated in a CPM dye laser [21].

Over the past five years, the field of femtosecond lasers has witnessed a revolution due to the emergence of reliable and convenient solid-state femtosecond lasers. The pace of progress has been truly remarkable. Additive pulse modelocking of the Ti:Al_2O_3 medium in 1989 sparked the interest of the entire community [30], following which much effort was put into the modelocking of Ti:Al_2O_3 lasers using intracavity, all-solid-state, bulk nonlinearities. This lead to several developments [95, 94, 96, 49], including the crucial identification of self-modelocking by Spence et. al. in 1991 [104]. Subsequent efforts were concentrated on simultaneously reducing pulse durations from the Kerr-lens modelocked (KLM) [107] oscillators [5, 3, 109] as well as amplification of pulses [108, 92, 10, 77, 88] in order to yield higher pulse energies. Extension of the available wavelengths from Ti:Al_2O_3 as well as the development of new solid-state femtosecond sources were also topics that were pursued intensively [61, 99, 19]. In recent months interest has shifted towards methods to improve compactness, practicality and reliability of femtosecond solid-state sources, as well as towards demonstrations of the applicability of these systems in commercial technology. This has lead

to concentration on diode-pumping schemes, monolithic devices and compact laser geometries.

The research into ultrashort pulse solid-state lasers presented in this thesis has spanned the last four years which have witnessed the exciting advances just described. The thesis itself reflects the rapidly evolving context it grew out of and the ideas demonstrated herein touch on various aspects of femtosecond pulse generation in solid-state lasers. The thesis begins with the demonstration of a novel technique for the passive modelocking of solid-state lasers. This technique (Microdot Mirror Modelocking) uses only intracavity, solid-state nonlinearities and its invention was almost simultaneous with the related and now popular technique of Kerr Lens Modelocking. It is demonstrated in both the Ti:Al_2O_3 [26] and the Nd:YLF [87] media.

As a part of the development and understanding of modelocking due to intracavity self-focusing, a numerical procedure for modeling the nonlinear behaviour of resonators has also been developed. This procedure which describes self-focusing by a nonlinear scaling of the Gaussian beam q parameter [40], is used to provide an exemplary, intuitive understanding of nonlinear effects in a simple resonator which is closely related to the gigahertz, femtosecond source that was subsequently implemented.

The most recent source developed in this thesis is the compact, gigahertz, femtosecond KLM Ti:Al_2O_3 source [89, 90]. To realize this source, a novel method for dispersion compensation was conceived, analyzed and implemented. The abovementioned iterative numerical model of self-focussing effects in simple resonators was an important input to this work. This work also serves to demonstrate the scalability of KLM techniques to very high repetition rates. The high-repetition rate source strongly reflects the current trend of the field towards compact, practical and reliable femtosecond sources.

The final chapter of the thesis deals with the enhancement of energies available directly from femtosecond Ti:Al_2O_3 oscillators. The method of cavity-dumping is

demonstrated as a viable technique for the generation of intermediate energy, femtosecond pulses at variable repetition rates [88, 86]. This source is an important alternative to more complex and expensive, high-energy, relatively low repetition-rate schemes for amplifying pulses from Ti:Al_2O_3 lasers.

The organization of the thesis is as follows:

Chapter 2 overviews the subject of modelocking, with particular attention to modelocking in solid-state laser media. Pulse shaping mechanisms are described and the master-equation formalism is used to predict the main characteristics of passively modelocked systems.

Chapter 3 reviews the analysis of resonator modes using the Gaussian beam q-parameter analysis and the ABCD matrix formalism. The phenomenon of self-focusing and its description as a non-linear scaling of the q parameter are explained and used to develop an iterative procedure for the solution of non-linear spatial modes in simple laser cavities.

Chapter 4 presents the technique of Microdot Mirror Modelocking as applied to Ti:Al_2O_3 and Nd:YlF systems.

Chapter 5 extends the technique of KLM to the high repetition rate regime, demonstrating the gigahertz operation of a KLM Ti:Al_2O_3 laser.

Chapter 6 presents the cavity-dumped femtosecond Kerr-lens-modelocked Ti:Al_2O_3 laser.

Chapter 7 summarizes the contributions of the thesis.

Appendix A contains a derivation related to the description of self-focusing as a non-linear scaling of the Gaussian beam q-parameter.

Appendix B lists the computer code for the iterative calcuation of non-linear cavity modes.

Appendix C provides details related to the estimation of group-velocity-dispersion in the GHz Ti:Al_2O_3 oscillator.

Chapter 2

Modelocking in solid-state lasers

2.1 Introduction

The process of "locking" the multiple oscillating longitudinal modes in a laser cavity into a definite relative phase relationship is known as modelocking. The temporal output of such a modelocked laser consists of a train of pulses, the widths of which are inversely proportional to the frequency bandwidth over which the longitudinal modes maintain a definite relative phase.

In order to design and construct the femtosecond laser systems described in this thesis it is essential to understand the basic operating principles of modelocked lasers. This chapter seeks to summarize the important principles relevant to the passive modelocking of lasers. The organization of this chapter is as follows. Section 2.2 provides a brief introductory description of the process of modelocking. Section 2.3 reviews passive modelocking techniques. Section 2.4 discusses fast saturable aborber modelocking. Pulse shaping mechanisms of fast-saturable-absorber action, self-phase modulation, group-velocity dispersion and gain-dispersion are discussed in Section 2.4.1. Section 2.4.2 uses these concepts to develop the master equation for fast-saturable-absorber modelocking which is used to describe the steady-state pulsed behaviour of passively modelocked systems. Section 2.5 describes the characteristics

of the Nd:YLF and Ti:Al_2O_3 gain media used in this thesis, and reviews the state-of-the-art for modelocking in these laser systems.

2.2 Modelocking

The most fundamental concept in this context is that of the existence of discrete axial or longitudinal laser frequencies. If T is the round trip time of the laser, then the frequency separation of axial modes in the laser cavity is given by:

$$\omega_{ax} = \omega_{n+1} - \omega_n \tag{2.1}$$

$$= \frac{2\pi}{T} \tag{2.2}$$

where the index n denotes mode number. To understand why the laser spectrum consists of such discretely spaced axial modes one need only recall that the total steady-state output of the laser after N round trips, $E^N(t)$, can be expressed as:

$$E^N(t) = E(t) \otimes \sum_0^N \delta(t - nT) \tag{2.3}$$

where E(t) is the periodic steady-state circulating electric field in the laser, the index n denotes number of round trips and T is the round trip time of the laser. Using basic Fourier transform theory one can immediately write that

$$\tilde{E}^N(\omega) = \frac{2\pi}{T}\tilde{E}(\omega)\sum_0^N \delta(\omega - n\frac{2\pi}{T}) \tag{2.4}$$

$$= \omega_{ax}\tilde{E}(\omega)\sum_0^N \delta(\omega - n\omega_{ax}) \tag{2.5}$$

where $\tilde{E}(\omega)$ is the Fourier transform of E(t) and ω_{ax} is the axial frequency separation defined in Equation 2.2. Thus the total output spectrum from the laser consists of discretely spaced axial components separated by ω_{ax}, the width of each component

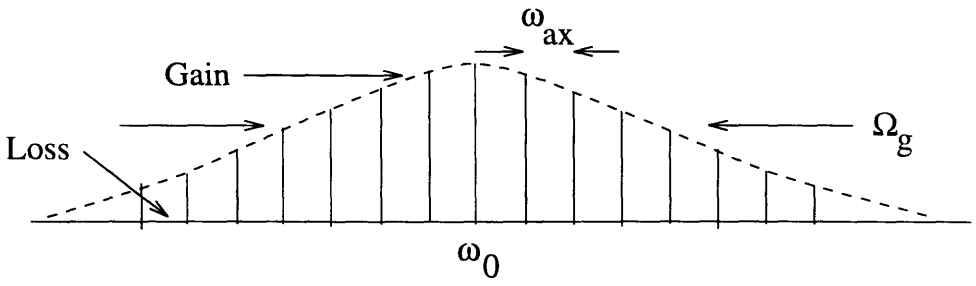

Figure 2-1: The axial modes in a laser cavity. The spectral bandwidth over which the dispersive gain exceeds the loss defines the window over which these modes will oscillate.

being proportional to the spectral bandwidth of $\tilde{E}(\omega)$. The actual number of such modes oscillating in the laser is limited by the spectral window where the frequency dependent laser gain exceeds the intracavity loss. Figure 2-1 depicts the situation graphically.

In general, in a continuous wave laser the above-described coexistent multiple axial modes oscillate with no well-defined phase with respect to one other. The resultant temporal output is therefore randomly varying in time though it repeats itself on every round trip in the steady state. However if the spectral components are somehow forced to oscillate with a fixed phase relationship with respect to each other the temporal duration of the pulse can be made extremely short.

To illustrate this [111, 103], let us analyze the case where there are 2N +1 axial frequency components oscillating with equal amplitude, E_0, and constant relative phase, ϕ, from each mode to the next. We then have,

$$E(t) = \sum_{-N}^{N} E_0 \; exp \; j[(\omega_0 + n\omega_{ax})t + n\phi] \tag{2.6}$$

where ω_0 is the frequency of the central mode. We can then write that

$$E(t) = A(t)\, exp\ (j\omega_0 t) \tag{2.7}$$

where

$$A(t) = \sum_{-N}^{N} E_0\, exp[\ jn(\omega_{ax} t + \phi)] \tag{2.8}$$

By executing a change of variables from t to t′ with.

$$\omega_{ax} t' = \omega_{ax} t + \phi \tag{2.9}$$

we have that

$$A(t') = E_0 \sum_{-N}^{N} exp\ (jn\omega_{ax} t') \tag{2.10}$$

$$= E_0 \frac{sin[(2N+1)\omega_{ax} t'/2]}{sin[\omega_{ax} t'/2]} \tag{2.11}$$

The resulting output intensity is:

$$I(t') \sim E_0^2 A^2(t') \tag{2.12}$$

$$= E_0^2 \frac{sin^2[(2N+1)\omega_{ax} t'/2]}{sin^2[\omega_{ax} t'/2]} \tag{2.13}$$

Figure 2-2 [111] plots Equation 2.13 for the case of seven such oscillating modes with equal amplitudes. It is clear that as a result of the phase locking condition the oscillating modes interfere to produce a train of light pulses. Successive pulses in this train are separated by a time τ_p where,

$$\tau_p = \frac{2\pi}{\omega_{ax}} \tag{2.14}$$

If one associates the FWHM, $\Delta\tau_p$ of the pulse with the time to the first null in Figure 2-2 we get that

$$\Delta\tau_p = \frac{2\pi}{(2N+1)\omega_{ax}} \tag{2.15}$$

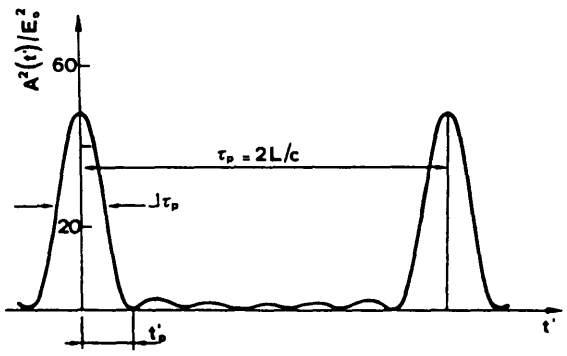

Figure 2-2: Temporal intensity resulting from seven longitudinal modes of equal intensity being locked together with a fixed phase relationship [111]. L is the laser cavity length, c the speed of light, $\Delta\tau_p$ the pulsewidth and τ_p the pulse separation time.

Since the total frequency range of oscillating modes spans the gain bandwidh, Ω_g of the laser this implies that

$$\Delta\tau_p = \frac{2\pi}{\Omega_g} \tag{2.16}$$

This relationship between pulsewidth and gain bandwidth is fundamental to all ultrashort pulsed lasers.

2.3 Passive modelocking techniques

Several techniques have been proposed for achieving the above-described definite phase relationship between axial laser modes. The schemes can be broadly classified into active modelocking schemes and passive modelocking schemes, both of which have been extensively studied and reviewed [103, 111, 48, 57, 42]. Since this thesis deals with ultrashort pulsed solid-state lasers, it is appropriate to limit the current discussion to that class of modelocking techniques which currently predominates in

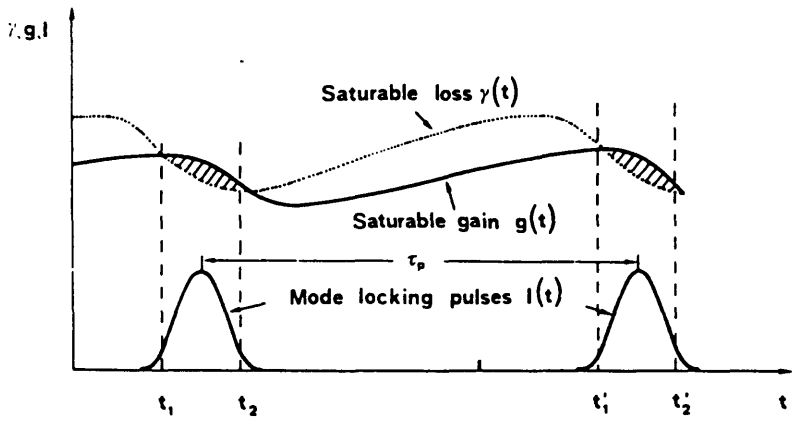

Figure 2-3: Slow saturable sbsorber action

the modelocking of solid-state lasers and is generally referred to as *passive*.

Passive modelocking encompasses those techniques where the periodic modulation of gain, necessary for pulse formation, is provided by the laser pulse itself. Passive modelocking can itself be divided into slow saturable absorber and fast saturable absorber categories. A saturable absorber is defined as an intensity dependent loss mechanism which preferentially transmits light of higher intensity. Slow saturable absorbers are not able to recover on the time scale of the circulating short pulse and consequently their transmission is a function of the integrated intensity of the pulse passing through. Fast saturable absorbers on the other hand respond instantaneously to the pulse intensity and the loss profile of the absorber essentially mimics the profile of the pulse itself.

Slow saturable absorber techniques have been widely used in the first generation of femtosecond lasers namely dye-lasers [45]. In combination with dynamic gain saturation in these media it transpired that absorbers with nanosecond recovery times could be successfully employed to generate sub-picosecond pulses [45, 100]. This is due to dynamic gain saturation which in conjunction with the saturation of the absorber

results in a narrow window of time which exhibits net intracavity gain. Consequently, pulse formation in this time-window is favored over continuous wave oscillation. The dynamics of this interaction are depicted in Figure 2-3 and have been discussed by several authors [42]. Slow saturable absorber modelocking techniques have been used to produce 28 fs pulses [117] directly from a colliding pulse modelocked (CPM) dye laser, as well as to study various phenomena related to femtosecond pulse generation.

After the era of the CPM laser, attention has turned in recent years to solid-state laser media which display very different properties from dye media. The properties of the particular media (Ti:Al_2O_3 and Nd:YLF) used in this thesis will be reviewed later in this chapter. However, the properties that generally distinguish solid-state gain media most prominently, in the context of viable modelocking techniques, are their relatively long upper-state lifetimes ($\sim \mu s$) and small gain crossections. Consequently, dynamic gain saturation critical for sub-picosecond pulse formation using slow saturable absorber action, does not occur in solid-state materials on the time scale of several nanoseconds which typically corresponds to the cavity round trip time. As a result fast saturable absorber techniques are essential for ultrashort pulse generation in solid-state media.

The action of a fast saturable absorber is illustrated schematically in Fig 2-4. The problem of course is to find absorbers that work on a femtosecond time scale. While real absorber dyes that are fast enough are hard to find, fortunately fast saturable absorber-like action can be engineered in several ways. Thus as will be described in subsequent sections and chapters , "artificial fast-saturable absorbers" can be incorporated into solid-state laser cavities to achieve femtosecond pulse generation.

Fast saturable absorber modelocking often relies critically on pulse shaping mechanisms other than saturable absorber action. These include self-phase-modulation (SPM), group-velocity dispersion (GVD) and gain dispersion. The role of SPM and GVD in modelocking were explored following the observation of residual chirp on pulses produced by dye-lasers and the introduction of adjustable negative intracavity

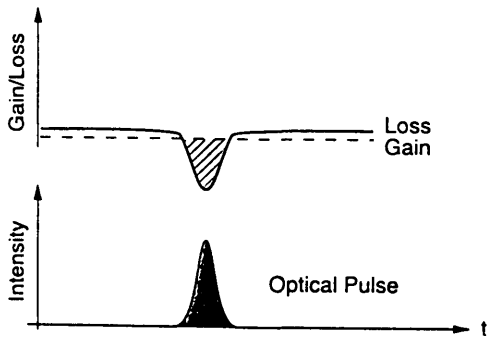

Figure 2-4: Fast saturable absorber action

dispersion using prism pairs [23]. The soliton-like pulse shaping mechanism set up by the interaction of SPM and negative GVD was identified and proven to result in the production of much shorter pulses than the amplitude modulation produced by saturable absorber action alone could produce. However SPM was observed also to strongly effect the stability of the laser pulses. Before attempting to explain these characteristics of FSA modelocking it is helpful to understand the origin and nature of the various pulse shaping mechanisms involved.

2.4 Fast saturable absorber modelocking

2.4.1 Pulse shaping mechanisms

Saturable absorber action

Saturable absorber action has already been defined in the preceding discussion. Mathematically, one expresses this intensity dependent loss as an effective change, ΔE in amplitude of a pulse passing through a fast saturable absorber medium. We then

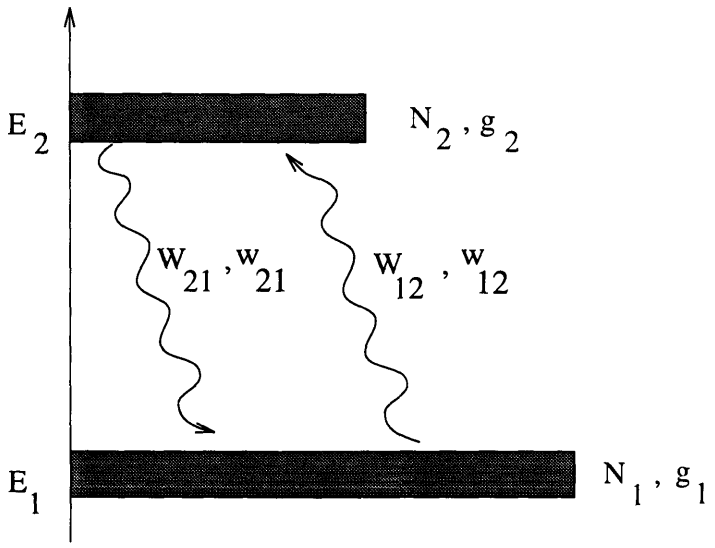

Figure 2-5: Two level atomic system

have,

$$\Delta E = -\gamma \ |E|^2 E \tag{2.17}$$

where E is the field amplitude and γ the fast saturable absorber cross section in units of 1/W.

Real saturable absorbers, consist of systems where the optical absorption of the medium actually saturates with increasing light intensity. The phenomenon of saturation can be understood by modeling the absorption in the two level atomic system shown schematically in Figure 2-5 [103]. If N represents the constant total system population, N_1 and N_2 the atomic populations of each level, W_{12} and W_{21} the stimulated transition rates, and w_{12} and w_{21} the relaxation rates, we can derive the following rate equation for the population difference $\Delta N = N_1 - N_2$,

$$\frac{d}{dt}\Delta N(t) = -(W_{12}+W_{21})\Delta\, N(t)+(W_{21}-W_{12})N-(w_{12}+w_{21})\left(\Delta\, N(t) - \frac{w_{21}-w_{12}}{w_{12}+w_{21}}N\right) \tag{2.18}$$

This equation can be simplified for non-degenerate systems where $W_{12} = W_{21}$, if we

define $w_{12} + w_{21} = 1/T_1$ and note that the thermal equilibrium population is

$$\Delta N_0 = \frac{w_{21} - w_{12}}{w_{12} + w_{21}} N. \tag{2.19}$$

Then we have

$$\frac{d}{dt}\Delta N(t) = -2W_{12}\Delta N(t) - \frac{\Delta\, N(t) - \Delta\, N_0}{T_1}. \tag{2.20}$$

and the steady state population difference, ΔN_{ss}, is given by:

$$\Delta N_{ss} = \Delta\, N_0 \times \frac{1}{1 + 2W_{12}T_1} \tag{2.21}$$

This steady state population difference is established based on the balance between the stimulated transition term which acts to transfer atoms from the more heavily populated lower energy level N_1 to the less populated upper energy level N_2 and the relaxation term which pushes the population difference towards its thermal equilibrium value. At high enough intensities (ie for $W_{12}T_1 \gg 1$) the two phenomena just balance each other and the two level populations equalize causing the net power absorbed to tend to zero. This is the phenomenon of absorption saturation.

While real saturable absorber dyes are attractive due to their simplicity they tend to be limited in speed. From the condition for saturation ie. $W_{12}T_1 \gg 1$, it is evident that in such systems speed is gained only at the expense of increased saturation intensity. This limits the use of real fast saturable absorbers to high intensity systems and also increases concerns regarding thermal damage to the absorber.

Artificial saturable absorbers are therefore an important modelocking alternative due to their speed, the fact that they do not dissipate power and their adjustable parameters. Artificial saturable absorbers provide an intensity dependent loss mechanism like real absorber dyes; however this does not originate from actual absorption saturation such as that described above. The artificial fast saturable absorber mechanism of primary interest in this thesis arises from the Kerr nonlinearity in a solid-state medium which has a response time on the order of a few femtoseconds [80].

The Kerr effect arises from the nonlinear polarization induced in media under the influence of a strong electric field. The polarization in a medium can in general be expressed as:

$$P = \chi_1 \epsilon_0 E + \chi_2 E^2 + \chi_3 E^3 + ... \tag{2.22}$$

The second order susceptibility, χ_2 exists only in non-centrosymmetric crystalline arrangements , but the third order susceptibility, χ_3 exists in any solid, liquid or gaseous medium. If we include the χ_3 term, we have that the electric displacement, D, is given by

$$\begin{aligned} D &= \epsilon_0[1 + \chi_1]E + \chi_3 E^3 && (2.23) \\ &= \epsilon_0[1 + \chi_1 + \epsilon_0^{-1}\chi_3 E^2]E && (2.24) \end{aligned}$$

Thus the complete nonlinear dielectric constant is

$$\epsilon = \epsilon_0(1 + \chi_1) + \epsilon_2 E^2 \tag{2.25}$$

where $\epsilon_2 = \chi_3$ and consequently the index of refraction of the medium, $n = \sqrt{\epsilon/\epsilon_0}$ is given by

$$n = n_0 + n_2 I \tag{2.26}$$

where n_0 and n_2 are defined as follows:

$$\begin{aligned} n_0 &= \sqrt{1 + \chi_1} && (2.27) \\ n_2 &= \frac{1}{2}\eta\frac{\chi_3}{\epsilon_0} && (2.28) \end{aligned}$$

where η is the impedance of the material.

Most condensed materials have $n_2 \sim 10^{-16} cm^2/W$. Some organic materials with long molecular chains may exhibit n_2 values about an order of magnitude higher than this. The Kerr effect becomes important in modelocked lasers at intensities where

the change in optical length brought about by the nonlinear refractive index becomes comparable to a wavelength. Using typical values for the Ti:Al_2O_3 gain medium (ie. $n_2 = 3 \times 10^{-16}$ cm^2/W, $\lambda = 800$ nm, L = 1cm) this translates to intensities on the order of 100 GW/cm^2. Peak intensities in typical femtosecond lasers usually reach several tens of GW/cm^2 and are therefore sufficient to render Kerr nonlinearities significant.

The most important consequence of the Kerr effect in the context of modelocking, is the resultant phenomena of self-focusing. Self-focusing occurs due to the non-uniform transverse spatial profile presented by a Gaussian pulse propagating through a Kerr medium. The central higher intensity portions of the beam modify the local refractive index by the Kerr effect while the peripheral low intensity portions do not. Consequently an intensity-dependent lens which counteracts the normal diffractive divergence of the propagating beam is set up. At a certain power defined as the critical power for self-focussing, P_{crit}, self-focusing exactly balances diffraction and the beam propagates in a collimated fashion. For powers in excess of the critical power the self-focusing process becomes catastrophic and the beam collapses to a singularity. Of course, higher order effects or damage in the propagation medium set in before this can happen in actuality.

The phenomenon of self-focusing is at the basis of the fast saturable absorber-like action obtainable in solid-state lasers. Stated very simply, Kerr induced self-focussing in nonlinear media results in the modification of intracavity beam profiles for high intensities in comparison with the low intensity profiles. Consequently at certain positions in a laser cavity, light of higher intensity may produce a narrower spatial profile than light of lower intensity. If a spatial aperture is placed at such a point to selectively transmit the high intensity profile, the result is precisely an intensity dependent loss mechanism, or saturable absorber.

Modelocking that utilizes artificial saturable absorber action due to self-focussing has been termed Kerr Lens Modelocking (KLM) [107, 83, 51] and is extremely popular

in current day solid-state lasers. The actual methods for analyzing KLM laser cavities and determining the effects of self-focussing on cavity modes as a function of power are complex and varied. These methods include numerical procedures and analytic solutions and will be reviewed in a Chapter 3. A numerical approach based on nonlinear transformation of the Gaussian beam q parameter to model the problem of self-focussing in simple laser resonators was implemented and used as a part of this thesis and will also be described in Chapter 3.

Self phase modulation

Self phase modulation is a temporal nonlinear effect also originating in the Kerr nonlinearity. As discussed previously a medium with a Kerr effect displays an intensity dependent refractive index, ie:

$$n = n_0 + n_2 I(t) \tag{2.29}$$

Thus in propagating a distance L in such a medium, a pulse defined initially by

$$E(z,t) = E(t)e^{j(\omega_0 t - kz)} \tag{2.30}$$

acquires a time varying phase shift $\phi(t)$ which can be expressed as

$$\phi(t) = -\frac{2\pi}{\lambda} L(n_0 + n_2 I(t)). \tag{2.31}$$

where λ is the wavelength in air. Thus the time rate of change of phase across the pulse will be a function of the intensity and we have that

$$\frac{d\phi(t)}{dt} = -\frac{2\pi}{\lambda} L n_2 \frac{dI(t)}{dt} \tag{2.32}$$

A time-dependence in the phase-derivative across a pulse corresponds in fact to "chirp", that is a variation in instantaneous frequency across the pulse. For the ma-

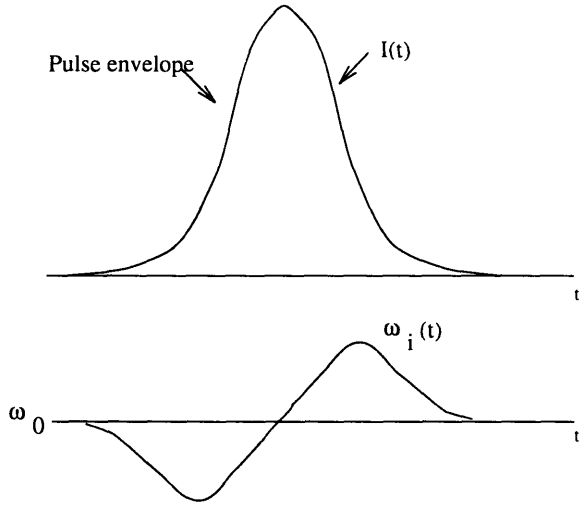

Figure 2-6: Frequency shift due to self-phase modulation

jority of materials since the nonlinear index n_2 is positive, the leading edge of the pulse with dI/dt $>$ 0 will experience a down shift in frequency (red shift) and the trailing edge of the pulse with dI/dt $<$ 0 will experience an up shift in frequency (blue shift). Figure 2-6 illustrates the idea schematically. ω_0 in this figure is the initially uniform carrier frequency of the unchirped pulse and $\omega_i(t)$ is the instantaneous frequency after propagation through the medium.

We can consider mathematically the effect of self-phase modulation on an initially unchirped Gaussian pulse [103]. We have

$$E(t) = E_0 e^{-at^2} e^{j\omega_0 t} \tag{2.33}$$

$$I(t) = I_0 e^{-2at^2} \tag{2.34}$$

where $I_0 = E_0^2/\eta$ and η is the impedance of the material. Assuming for simplicity that the pulse shape remains constant, after propagation over a length L of a Kerr

medium the instantaneous frequencies across the pulse will be described by

$$\omega_i(t) = \frac{d\phi}{dt} \tag{2.35}$$

$$= \omega_0 - \frac{2\pi n_2 L}{\lambda}\frac{dI}{dt} \tag{2.36}$$

$$= \omega_0 - \frac{4\pi a n_2 L I_0}{\lambda} \times te^{-2at^2} \tag{2.37}$$

$$\sim \omega_0 - \frac{4\pi a n_2 L I_0}{\lambda} \times t \tag{2.38}$$

Clearly to first order, SPM results in the addition of a linear frequency chirp to the initially unchirped pulse. It is easily proven that the time-bandwidth product of the pulse will increase by a factor of $\sqrt{2}$ when the condition

$$\frac{4\pi n_2 I_0 L}{\lambda} = 1 \tag{2.39}$$

is met. Assuming typical operating parameters for the Ti:Al_2O_3 laser, (10 W of average intracavity power, a 10 ns round-trip time, a 10 fs pulse and a 30 μm focussed beam waist in the crystal, the peak focussed intensity in the crystal is approximately $I_0 \sim 35$ GW/cm^2. Using Equation 2.39 with $n_2 \sim 3 \times 10^{-16}$) and $\lambda = 800$ nm, we find therefore that a crystal length, L, of 1.2 cm is required for the accumulation of significant amounts of SPM. Crystal lengths in KLM Ti:Al_2O_3 lasers range anywhere from 2 mm to 2 cm and SPM must therefore be considered an important mechanism in these lasers.

SPM is thought of as a spectral broadening mechanism since it generates new frequencies by red-shifting the leading edge of the pulse and blue-shifting the trailing edge. In any medium exhibiting dispersion these newly generated frequency components propagate at different velocities and consequently affect pulse duration. In a medium with positive dispersion (blue travelling slower than red) the blue-shifted trailing edge of the pulse will fall further and further back with respect to the red-shifted leading edge and the pulse will tend to broaden. On the other hand in a

medium with negative dispersion (blue travelling faster than red) the blue-shifted trailing edge of the pulse will "catch up" with the main part of the pulse and the red-shifted leading edge will "fall back" to the main part of the pulse; consequently the pulse will undergo compression. This latter compressive effect on pulses, arising from the interplay between SPM and GVD is at the basis of soliton generation and propagation [36] . Consequently this interaction is termed soliton-like pulse shaping. It plays a critical role in femtosecond pulse generation from a variety of sources.

Group velocity dispersion

Intracavity group velocity dispersion is an important pulse broadening mechanism to contend with in the formation of an ultrashort light pulse. A dispersive medium is defined as one having a frequency dependent propagation constant $\beta(\omega)$ which can be expanded in a Taylor series around the central freqency ω_0 to give

$$\beta(\omega) = \beta(\omega_0) + \beta'(\omega)|_{\omega_0}(\omega - \omega_0) + 1/2 \;\; \beta''(w)|_{\omega_0}(\omega - \omega_0)^2 + ... \tag{2.40}$$

In order to define the concept of GVD and to understand its effects on pulse width it is instructive to follow the development of Siegman [103] where a Gaussian pulse is propagated through a dispersive medium. The input pulse is written in the time domain as

$$E_0(t) = exp(-\Gamma_0 t^2 + j\omega_o t) \tag{2.41}$$

where $\Gamma_0 = a_0 - jb_0$ is a complex gaussian parameter describing the initial pulse. Taking the Fourier transform, in the frequency domain we can write that

$$\tilde{E}_0(\omega) = exp\left[-\frac{(\omega - \omega_0)^2}{4\Gamma_0}\right] \tag{2.42}$$

Note that the pulsewidth and time bandwidth product for this pulse are given by

$$\tau_p = \sqrt{\frac{2ln2}{a_0}} \tag{2.43}$$

$$\Delta f_p \tau_p = 0.44 \times \sqrt{1 + (b_0/a_0)^2} \tag{2.44}$$

After propagation through a distance z in this medium we have that

$$\tilde{E}(z,\omega) = \tilde{E}_0(\omega) \times exp\ [\ -j\beta(\omega)z] \tag{2.45}$$

$$= \tilde{E}_0 exp\left[-j\beta(\omega_0)z - j\beta' z(\omega-\omega_0) - \left(\frac{1}{4\Gamma_0} + \frac{j\beta'' z}{2}\right)(\omega-\omega_0)^2\right] \tag{2.46}$$

To retrieve the temporal form of the output pulse we Fourier transform back into the time domain using

$$E(z,t) = \int_{-\infty}^{+\infty} E(z,\omega) e^{j\omega t}\, d\omega. \tag{2.47}$$

Rearranging terms and bringing the frequency independent carrier terms outside the integral yields

$$E(z,t) = \frac{e^{j[\omega_0 t - \beta(\omega_0)z]}}{2\pi} \int_{-\infty}^{+\infty} exp\left[\frac{-(\omega-\omega_0)^2}{4\Gamma_{(z)}} + j(\omega-\omega_0)(t-\beta' z)\right]\, d(\omega-\omega_0) \tag{2.48}$$

where

$$\Gamma(z) = 1/\Gamma_0 + 2j\ \beta''(\omega)|_{\omega_0}\ . \tag{2.49}$$

By changing variables to $\omega' = \omega - \omega_0$ and $t' = t - \beta' z$ we can write that

$$E(z,t) = \frac{e^{j[\omega_0 t - \beta(\omega_0)z]}}{2\pi} \int_{-\infty}^{+\infty} exp\left[\frac{-\omega'^2}{4\Gamma_{(z)}} + j\omega' t'\right]\, d\omega'. \tag{2.50}$$

The integral term is then easily recognized as the Fourier transform of a Gaussian pulse ie.

$$\int_{-\infty}^{+\infty} e^{\frac{-\omega'^2}{4\Gamma(z)}} e^{j\omega' t'}\, d\omega' = exp[-\Gamma(z)t'^2] \tag{2.51}$$

$$= exp[-\Gamma(z)\ (t - \beta'(\omega)|_{\omega_0}\ z)^2] \tag{2.52}$$

Thus the total output field is

$$E(z,t) \sim exp[j\omega_0(t - \beta(\omega_0)z)] \times exp[-\Gamma(z) \times (t - \beta'(\omega)|_{\omega_0}\ z)^2] \tag{2.53}$$

$$\sim exp[j\omega_0(t - \frac{z}{v_\phi(\omega_0)}) \times exp[-\Gamma(z) \times (t - \frac{z}{v_g(\omega_0)})^2] \tag{2.54}$$

where $\Gamma(z)$ is the modified gaussian pulse parameter after propagation defined by 2.49 and the phase and group velocities of the pulse, v_ϕ and v_g are defined as

$$v_\phi(\omega_0) = \omega_0/\beta(\omega_0) \tag{2.55}$$

$$v_g(\omega_0) = 1/\ \beta'(\omega)|_{\omega_0} \tag{2.56}$$

respectively.

The concepts of group velocity and phase velocity are familiar from the propagation of electromagnetic waves and wave packets. With the above definition of group velocity, the definition of group velocity dispersion is clear. Group velocity dispersion per unit length, β'', merely describes the frequency dependence of the group velocity ie:

$$\beta''(\omega) = \frac{d}{d\omega}\frac{1}{v_g(\omega)} \tag{2.57}$$

The important point to note regarding propagation in the presence of GVD is that while the output pulse of Equation 2.54 is indeed Gaussian it is characterized by a *modified* complex Gaussian beam parmeter which is proportional to the total group-velocity dispersion (GVD) experienced by the pulse . We have that

$$\frac{1}{\Gamma(z)} = \frac{a_0}{a_0^2 + b_0^2} + j(\frac{b_0}{a_0^2 + b_0^2} + 2\beta''z) \tag{2.58}$$

$$= \frac{1}{a(z) - jb(z)} \tag{2.59}$$

$$= \frac{a(z)}{a(z) - jb(z)} + \frac{jb(z)}{a^2(z) + b^2(z)} \tag{2.60}$$

The real part of $1/\Gamma(z)$ which describes the bandwidth of the pulse remains constant. The quantity $\sqrt{1 + [b(z)/a(z)]^2}$ which describes the time-bandwidth product increases, with increasing propagation distance, corresponding to an increasingly chirped pulse.

In general, propagation through an arbitrary dispersive optical system results in a frequency dependent phase shift, $\phi(\omega)$ and the GVD of the system is described by $d^2\phi/d\omega^2$. Using standard relations between frequency and wavelength and the chain rule for derivatives it is easily proven that for a medium of length l, with a constant refractive index, n(λ),

$$\frac{d^2\phi}{d\omega^2} = \frac{\lambda^3}{2\pi c^2} \frac{d^2 n(\lambda) l}{d\lambda^2} \tag{2.61}$$

More generally for a medium with varying refractive index we can write

$$\frac{d^2\phi}{d\omega^2} = \frac{\lambda^3}{2\pi c^2} \frac{d^2 P(\lambda)}{d\lambda^2} \tag{2.62}$$

where P(λ), the optical path length of the medium of physical length l, is given by

$$P(\lambda) = \int_0^l n(\lambda) dz \tag{2.63}$$

This latter definition of GVD is a useful one which will be used in subsequent analysis.

Gain dispersion

Gain dispersion is the term used to describe a frequency dependent laser gain. Gain dispersion is a fundamental concept arising from the lineshapes of atomic transitions involved in laser action. Lineshapes account for the fact that the atomic energy levels involved in laser action are not infinitely sharply defined but rather have finite bandwidths arising from a variety of physical phenomena. The exact mathematical

form of the lineshape is dependent on the specific broadening processes involved. However we can classify gain media into those that are homongenously broadened and those that are inhomogeneously broadened.

Homogeneous Broadening arises when every atom involved in laser action possesses the same atomic lineshape and frequency response. Consequently each atom in an ensemble of atoms composing the laser medium responds identically to an applied signal. The derivation of the Lorentzian frequency dependence of the lineshape is routine [103] and will only be quoted here as

$$G_L(\omega) \sim \frac{1}{(\omega - \omega_0)^2 + \left(\frac{\Omega_g}{2}\right)^2} \tag{2.64}$$

where Ω_g is the homogeneous linewidth of the transition and ω_0 its central frequency. Various effects in laser gain media give rise to homogenous broadening. These include the finite lifetime of the upper-state, the interruption of the radiative process by collisions between radiating particles, or the coupling to thermal vibrations in a host crystal lattice

Inhomogeneous broadening arises when the center frequencies (or energies) of individual radiating atoms become displaced from one another due to certain phenomena. Considering the ensemble of atoms then, one finds a variation in the resonant transition frequency from atom to atom and consequently the individual responses to applied signals cannot be treated identically. This kind of broadening gives rise to a Gaussian line shape i.e.:

$$G_g(\omega) \sim exp\ (-\ \frac{(\omega - \omega_0)^2}{\Omega_i^2}) \tag{2.65}$$

where Ω_i, the inhomogeneous linewidth, is large compared to the homogeneous linewidth Ω_g. Doppler broadening in gas lasers is an example of an ihomogeneous broadening process. In solid-state lasers, random crystal imperfections due to lattice strain or dislocations can give rise to a small degree of inhomogeneous broadening which tends

to be important only at low temperatures in the absence of homogenous broadening due to lattice vibrations.

An important difference between homogeneously and inhomogeneously broadened media lies in their saturation behaviour. For the same reasons why absorption saturates, laser gain is also subject to saturation at intensities that are high enough to deplete the initial population inversion through stimulated transitions to the lower level. Homogeneous broadening causes gain to saturate uniformly over its entire bandwidth while for strong enough signals, inhomogeneous media can saturate only over a fraction of the gain bandwidth thus creating spectral "hole-burning" effects.

For the Ti:Al_2O_3 laser which is the primary focus of this thesis, we can assume a homogeneously broadened line and the consequent Lorentzian line shape. Close to the gain center we can then use the approximation of a parabolic gain profile to write that

$$G(\omega) = g\left[1 - \frac{(\omega - \omega_0)^2}{\Omega_g^2}\right] \tag{2.66}$$

where g is the gain at the linecenter, ω_0 is the central frequency and Ω_g describes the gain bandwidth. Using the properties of the Fourier transform we can write this in the time domain as:

$$g_L(t) = g\left[1 + \frac{1}{\Omega_g^2}\frac{d^2}{dt^2}\right] \tag{2.67}$$

Gain dispersion acts effectively as a bandwidth limiting frequency filter which tends to broaden pulses that pass through it. Indeed as will be discussed shortly, it is an important parameter in determining the pulsewidth attainable from a fast saturable absorber modelocked laser.

2.4.2 The master equation for fast saturable absorber modelocking

Having understood the origin of the primary pulse shaping mechanisms in FSA modelocked lasers we can now describe the process of modelocking mathematically. The

master equation for FSA modelocking (in the steady state and under conditions of small changes per pass through the laser elements) has been developed by Haus [34]. It arises from the simple fact that in the steady state the complex pulse amplitude E(t) must reproduce itself after each round trip in the laser. Describing each pulse-shaping mechanism with an appropriately linearized operator, this condition can be translated mathematically into a differential equation in the time domain namely:

$$\left[g - l + j\psi + \frac{g}{\Omega_g^2}\frac{d^2}{dt^2} + jD\frac{d^2}{dt^2} + t_D\frac{d}{dt} + (\gamma - j\delta)\,|E(t)|^2\right] = 0 \qquad (2.68)$$

The terms in this equation can readily be identified as follows: l is the linear loss, g is the linear unsaturated gain, ψ represents the linear phase shift acquired per round trip, D is the total group velocity dispersion accumulated in dispersive intracavity media, γ describes the saturable absorber cross-section, δ is a self-phase modulation constant and t_D represents the timing shift per round trip that is caused by small deviations of the carrier frequency from an axial resonator frequency.

The analytic solution to this equation were first recognized by Martinez et. al. [70, 69] to be of the form

$$E(t) = E_0 sech(\frac{t}{\tau})\ exp\ [j\beta ln sech(\frac{t}{\tau})] \qquad (2.69)$$

The pulse is thus described completely by an amplitude, E_0, a pulsewidth, τ, and a chirp parameter β.

Haus has demonstrated that substituting Equation 2.69 back into the Master equation we can solve for four parameters namely, the pulsewidth, τ, the chirp, β, the gain, g, and the phase shift, ψ. The important features of the solutions are summarized in Figure 2-7 where the chirp, β, the normalized pulsewidth τ_n, the pulse bandwidth and a pulse stability parameter are plotted versus normalized dispersion for a fixed value of saturable absorber action while varying the strength of the SPM.

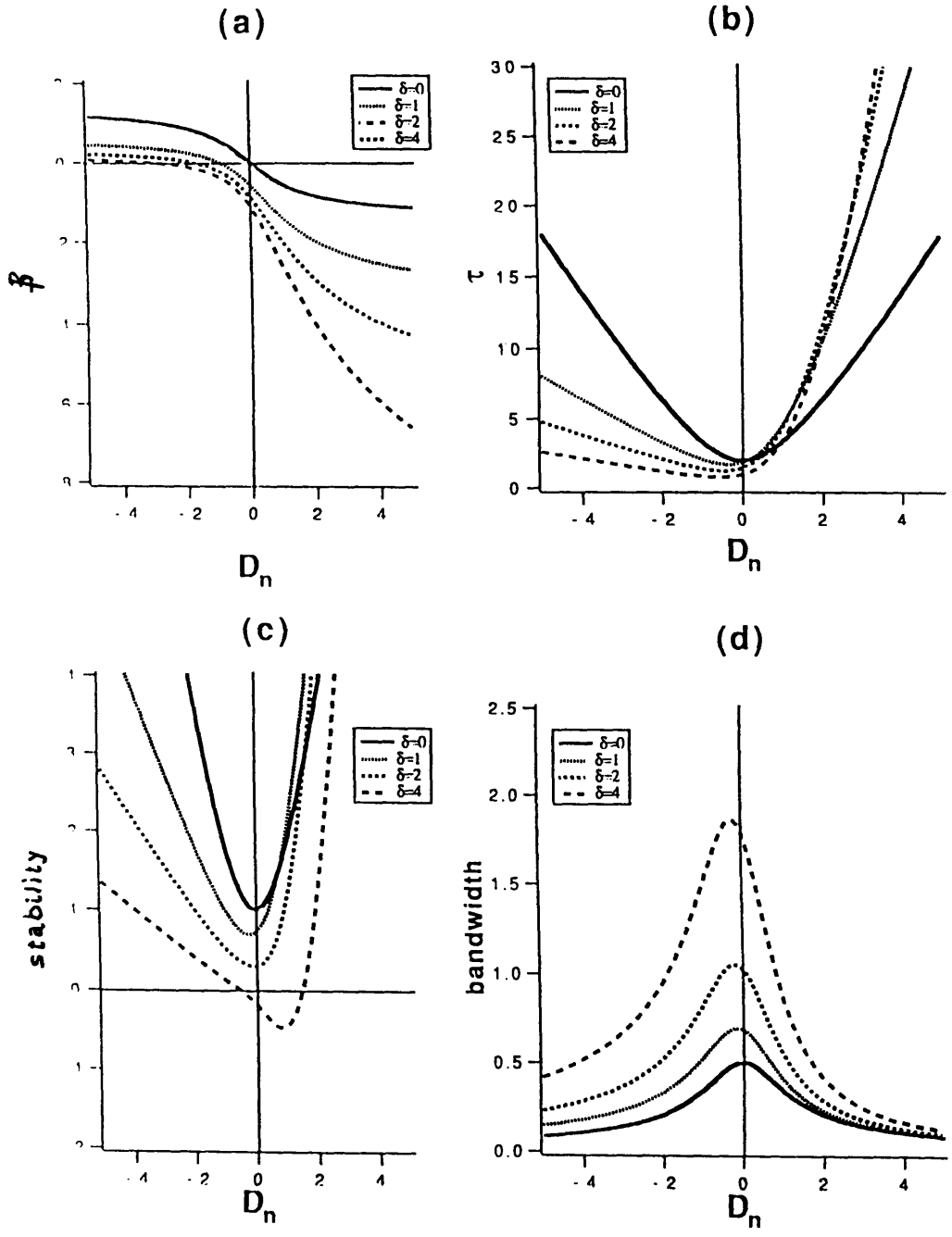

Figure 2-7: Predictions of the master equation: (A) Pulse chirp, (B) Normalized pulsewidth, (C) Pulse stability, and (D) Pulse bandwidth plotted against normalized dispersion for constant saturable absorber action and varying SPM

The normalized parameters are defined as

$$\tau_n = \frac{W\Omega_g^2}{2g}\tau \tag{2.70}$$

$$D_n = \frac{\Omega_g^2}{g}D \tag{2.71}$$

The bandwidth is defined as

$$\Omega = (1+\beta)^2(1/\tau_n) \tag{2.72}$$

The stability parameter is defined as the difference between the gain, g, during mode-locked operation and the cw gain, g_{cw} in continuous wave operation. For the pulse to be stable the stability parameter must be negative, ie. the gain before and after the pulse must be *less* than the loss (which equals the saturated value of the continuous wave gain, g_{cw}).

$$g - g_{cw} < 0 \tag{2.73}$$

Two distinct regimes of operation with qualitatively different pulse shaping mechanisms can be identified. From Figure 2-7a) and b), it is seen that in the positive dispersion regime, the chirp parameter β is large and the resultant pulse widths are long. Gain filtering actually acts as a pulse shortening process in the positive dispersion regime due to the chirped nature of the pulses. It balances the pulse broadening brought about by SPM and positive GVD. The magnitude of saturable absorber action has a strong influence on the pulse width.

Negative dispersion is required to attain short pulses with small amounts of chirp. The reason for this is clear from the earlier discussion about the soliton-like interaction between SPM and negative GVD. Saturable absorber action is critical in stabilizing the pulse formation process by providing discrimination against the breakthrough of CW radiation.

The stability criterion Equation 2.73 observed by both Martinez and Haus makes

the statement that the saturated gain seen by the wings of the pulse must be less than the loss seen by the wings of the pulse in order to avoid the breakthrough CW radiation before and after the pulse. SPM strongly effects the stability of the laser; indeed a pure soliton laser, in the absence of saturable absorber action is never stable because the finite bandwidth of the soliton will then make it experience less gain than CW radiation. Likewise, too much SPM can drive a laser unstable even in the presence of saturable absorber action (see Figure 2-7 c)). This is because with too much SPM, in the presence of the spectral filter of the gain, the pulse gradually begins to lose energy. Consequently the saturated value of the gain rises and the stability criterion of Equation 2.73 becomes violated.

Figure 2-7d) shows that the available bandwidth increases with increasing SPM (as expected due to the generation of new frequencies). With increasing SPM the asymmetry between the positive and negative dispersion regimes also becomes clearer.

The Master equation and its predictions can be used to describe a wide range of fast saturable absorber modelocked systems. While it is often hard to extract quantitative predictions from this formalism due to the difficulty in accurately quantifying phenomena like SPM and saturable absorber action, familiarity with the mechanisms involved and the general trends predicted in Figures 2-7 is essential in the design and operation of femtosecond lasers.

2.5 Modelocking of Ti:Al_2O_3 and Nd:YLF media

Having understood the general mechanisms responsible for modelocking in femtosecond lasers it is appropriate to turn specifically to the modelocking of the two media used in this thesis namely Ti:Al_2O_3 and Nd:YLF.

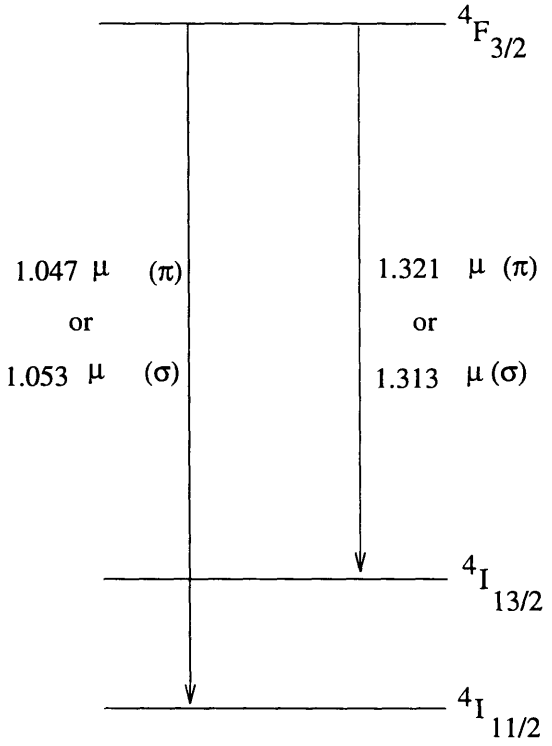

Figure 2-8: Energy level diagram for Nd:YLF

2.5.1 Nd:YLF

Several Nd:doped materials are used as solid-state laser gain media. Nd:YAG is particularly popular because of its excellent physical and thermal properties. The Nd doped Yttrium Lithium Flouride or Nd:YLF medium has also found widespread use. Particularly for the generation of short pulses in the 1.0 μ wavelength range, Nd:YLF is an important source since its gain bandwidth of 1.35 nm [62] is approximately three times as wide as the 0.45 nm bandwidth of Nd:YAG. The $\sigma\tau_f$ product, (where σ is the emission cross-section and τ_f is the flouresence lifetime) of the 1.053 μ Nd:YLF line is also 3 times greater than the analogous quantity for the 1.052 μ line in Nd:YAG. This makes the threshold power for lasing in Nd:YLF proportionately lower than in Nd:YAG.

A simplified energy diagram for the Nd:YLF medium is shown in Figure 2-8. Lasing is usually preferred on the 1.047 or 1.053 μ lines. π polarized light is emitted preferentially at 1.047 μ and σ polarized light at 1.053 μ. If no polarization optics are used π polarized light at 1.047 μ is obtained due to the 1.5 times higher gain crossection of the 1.047 μ, π transition compared to the 1.053 μ, σ transition. The Nd:YLF material has good thermal conductivity, its upper state lifetime is about 520 μs and the natural birefringence of the crystal can be advantageous in certain applications. Finally, the diode-pumpable nature of the Nd:YLF medium makes it an attractive alternative for a compact solid-state system.

Active modelocking of the Nd:YLF medium has been reported by several researchers to produce pulses in the 7 to 10 ps range. Passive modelocking techniques first emerged after the invention of Additive pulse modelocking (APM) [34]. APM relies on the coherent interference of a pulse in the main cavity and the phase-shifted feedback from a nonlinear external or coupled cavity. Since the phase shift is nonlinear, the wings of the pulses interfere destructively when the peaks interfere constructively. The result is saturable absorber action or pulse shortening. APM was first demonstrated in color center lasers and subsequently in a Ti:Al_2O_3 system [119, 30]. Diode-pumped, APM Nd:YLF systems were then implemented and produced pulse durations of about 2 ps [29, 62]. Another scheme relying on the use of a semiconductor saturable absorber in a coupled cavity (Resonant passive modelocking) produced 4 ps pulses [52] from Nd:YLF. Recently the technique of Kerr lens modelocking (KLM) has been succesfully extended to a diode pumped Nd:YLF system to produce pulses of 6 ps duration [68]. Finally, in this thesis the microdot mirror modelocking technique has been applied to an arc-lamp-pumped Nd:YLF system to produce 2.3 ps pulses [87] as will be described in the Chapter 4.

2.5.2 Ti:Al_2O_3

The Ti:Al_2O_3 medium has been the workhorse for the revolution in femtosecond solid-state lasers witnessed over the past five years. Possessing a bandwidth of over 300 nm, extending from 700 nm to past 1 μ, it is extremely attractive both for its tunability and its ability to support femtosecond pulses. Many material properties including low excited state absorption, high thermal conductivity, chemical inertness and mechanical rigidity have allowed rapid progress in the production of high quality Ti:Al_2O_3 laser rods of various diameters and doping densities.

The Ti:Al_2O_3 crystal is formed by the replacement of a small fraction of aluminium ions in the Al_2O_3 crystal lattice with ions of Ti^{3+}. Typical doping densities are in the range of 0.1 % to 0.25 % Ti^{3+} by weight. The effects of the crystal lattice on the electron energy levels of the Ti^{3+} ion are strong and result in many of the unique spectroscopic properties of Ti:Al_2O_3.

Figure 2-9 plots the energy levels in the Ti:Al_2O_3 system versus displacement of the Ti^{3+} ion. The energy levels in this diagram appear as continuous bands rather than discrete levels as was the case in the Nd:YLF medium. This is the key to the tunability of the Ti:Al_2O_3 medium. The reason for the spread of energy levels is that the Titanium ion can move within these "vibronic" bands by coupling vibrational energy to the host crystal lattice. The probability of finding a Ti^{3+} ion in the ground or upper laser states is shown as a normal probability distribution around points A and C. Optical pumping at 500 nm excites Ti^{3+} ions from the lower 2_{T_2} state (point A) to the two-fold degenerate upper 2_E states (point B). The excited Ti^{3+} ion can then release vibrational energy and move to the bottom (point C) of the upper vibronic band from where the lasing transition to point D in the lower band occurs. Finally the ion relaxes back vibronically to point A. The strong phonon interaction between the host and the Ti^{3+} ion, as well as the large separation between the electron energies involved results in the wide absorption and emission spectra of the medium. Another notable feature is that laser emission terminates at high vibrational levels

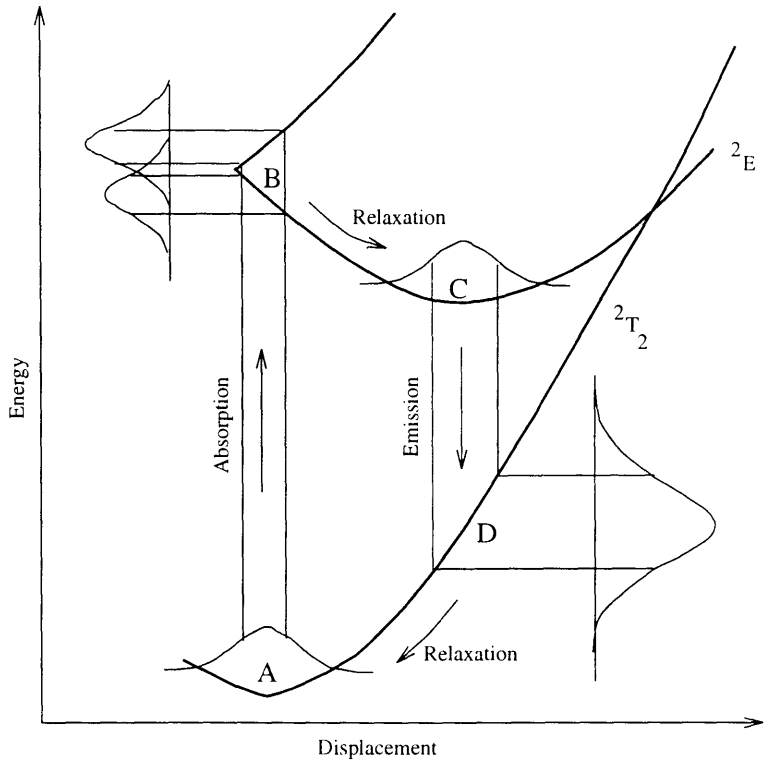

Figure 2-9: Energy level diagram for Ti:Al_2O_3.

of the ground state. These levels are unpopulated since the phonon relaxation to the lower vibronic states is relatively rapid. Consequently, the requisite population inversion between points C and D can be attained easily.

For all of the above mentioned reasons, in the late 1980s, Ti:Al_2O_3 became the material of choice for studying femtosecond pulse generation in solid-state lasers. The excellent material and spectroscopic properties of the Ti:Al_2O_3 medium [2, 76] lead to its demonstration as a highly promising, tunable, broadband laser system in the early 1980s [59, 102]. Following this, the revolutionary developements of the soliton laser [75] and the theory of Additive Pulse modelocking [43] emerged in the latter half of the decade. APM was demonstrated successfully in several systems and it was natural to try it in the new and promising Ti:Al_2O_3 system. In 1989 Goodberlet et. al. reported on the self-starting passive mode-locking of a Ti:Al_2O_3 laser using a nonlinear external cavity [30]. Other modelocking techniques were soon demonstrated in the Ti:Al_2O_3 syste, including Resonant passive modelocking [49], modelocking with a slow-saturable absorber dye-jet [95, 94] and modelocking using a colored glass filter [96].

Against this backdrop, in 1990 came the surprising discovery of Spence et. al. that sub-100 fs pulses could be generated in a Ti:Al_2O_3 medium using only intracavity nonlinearities [104]. They found that they could induce modelocking by misaligning the cavity in order support the existence of two spatial modes. However Spence did not offer a conclusive scientific explanation or proof of the mechanism at work and controversy about this issue was widespread. The role of self-focussing due to the Kerr nonlinearity in the gain medium was suggested early on [84, 51] but not proven conclusively. It is interesting to note that the use of self-focusing for laser modelocking had been suggested by researchers in the Soviet Union as early as 1975 [60].

Conclusive experimental proof for the role of self-focussing came in the spring of 1990 when researchers at Coherent Inc. modeled and designed a highly reliable and reproducible, sub-100 fs laser by modeling the self-focusing nonlinearity present in

the Ti:Al_2O_3 laser rod [107] . Further they showed that using appropriately positioned intracavity apertures (termed "hard" apertures) they could enhance the saturable absorber action achievable from self-focusing in the gain rod. They termed this technique of modelocking Kerr Lens Modelocking (KLM). Concurrent with their activities, efforts to conclusively explain the mechanism at work in Sibbett's experiment were also underway here at MIT. These culminated in the development of the techniques of modelocking using Kerr-polarization-rotation, and Microdot Mirror Modelocking [27, 26].

Following these revolutionary developments, the field of femtosecond pulse generation in KLM Ti:Al_2O_3 has continued to advance at an astonishing rate. Several different directions were taken by researchers. The amplification of oscillator pulses was one active area of research and important milestones in this area will be reviewed in Chapter 6. The development and modelocking of new material systems in order to extend the versatility of available sources has also actively pursued [61, 19, 99]. Harmonic generation and parametric oscillator techniques have also seen impressive advances.

Perhaps the most dramatic progress has been achieved in the reduction of pulse-durations achievable directly from the Ti:Al_2O_3 oscillator. The identification of the pulse width limiting effects of third order dispersion [39] lead to several demonstrations of decreasing pulse duration attained by the minimization of intracavity third-order dispersion. Many techniques were used in order to achieve minimum intracavity dispersion. Prisms and Gires-Tournois interferometers for independent control of second and third order dispersion [46]. New prism sequence arrangements for enabling the convenient use of very low-dispersive prisms were also developed [85]. However, the simple reduction of crystal length and judicious choice of prism materials [38, 3] has proved to be the most effective way of reducing pulse duration. 8.6 fs pulses have been attained using this approach [120]. Very recently the use of specially fabricated, low third-order dispersion, GVD-compensating mirrors [109] has also been

demonstrated as a novel and alternate way to achieve a very short pulse laser [109].

The shortest pulse duration achievable directly from Ti:Al_2O_3 oscillators stands today at an impressive 8.6 fs [120]. These pulses contain only 3 optical cycles and constitute the shortest pulses ever-generated directly from a laser. Efforts to reduce pulse duration even further by elimination of fourth order dispersive terms is ongoing. Meanwhile, as mentioned earlier, success in Ti:Al_2O_3 has inspired the development of other solid-state sources notably Cr:LiCrAlF_6 and Cr:LiSrCaAlF_6 which are broad band *and diode pumpable.* Successful KLM has already been demonstrated in these media [61, 19, 73]. New sources at different wavelengths, as well as novel optimizations of existing modelocking techniques will undoubtedly enable continued progress in this rapidly evolving field.

Chapter 3

Resonator mode analysis

3.1 Introduction

Techniques for the prediction of the spatial mode profile in a linear passive resonator are an important tool in laser design. The intracavity electromagnetic field in a laser can be described as a superposition of counterpropagating Gaussian beams which together set up a standing wave within the resonator. This standing wave solution satisfies both Maxwell's equations and the boundary conditions imposed by the mirrors at the resonator ends. Since the propagation of Gaussian beams in optical systems is conveniently described using the complex Gaussian beam q-parameter and ABCD ray matrices, these tools provide a general technique for calculating the intracavity Gaussian mode profiles in laser resonators.

As explained in chapter 2, Kerr lens modelocking (KLM) relies critically on self-focussing-induced resonator mode amplitude changes. These mode variations are translated into changes in gain using appropriately positioned intracavity apertures. In order to effectively design a KLM laser it is therefore essential to be able to predict the effects of self-focussing and the resultant "nonlinear" intracavity mode. Comparison of the nonlinear mode profile to the linear mode profile for different resonator configurations helps one to decide on the most appropriate setup for a

KLM laser.

Theoretical modelling of the effect of self-focussing on resonator spatial mode profiles is a complicated problem that has been treated both analytically and numerically by several authors. Salin et. al. were the first to quantify the effects of self-focussing on the modelocking of Ti:Al_2O_3 lasers [93]. Under the assumption of a quadratically varying complex propagation constant, (that accounts both for parabolic index variation due to self-focussing and parabolic gain variation due to the Gaussian profile of the pump beam) they derive an ABCD matrix for a nonlinear rod of given length. Using an initial guess for the complex cavity q-parameter the beam is propagated through the entire cavity including the nonlinear gain medium segmented into several layers. Iterative propagation back and forth through the cavity is continued until the solution converges.

Haus has obtained analytic solutions to specific KLM resonator configurations [35]. Using the nonlinear scaling of the q parameter to be described later in this thesis, and in the linearized limit of low powers, he derives the change in radius of curvature and beam waist caused by one transit through specific resonator configurations that include a Kerr medium. Constraining the solution through appropriate boundary conditions, the "KLM action" or differential change in mode size can be derived at specific planes in the cavity.

Brabec et. al. proposed another analytic solution to the problem in 1993 [12]. Their work deals with the most commonly used KLM resonator configuration consisting of a folded four mirror cavity with the crystal placed at an intracavity focus. The confocal parameter and the position of the beam waist are treated as power dependent variables. Using the equations for standard Gaussian beam propagation from the intra-crystal beam waist to each of the crystal surfaces, ABCD matrices for propagation from the crystal surfaces to the laser end mirrors and boundary conditions at those end mirrors, general expressions for the power-dependent confocal parameter and intracavity focus position are derived in the linearized limit of low

power. This technique is powerful but has the drawback of being relatively complex, and non-intuitive.

Finally Magni et. al. have recently provided a more intuitive understanding to the KLM resonator problem [65, 66]. In this case, the paraxial wave equation in a nonlinear medium is solved in the aberrationless limit using a parabolic approximation for the Gaussian beam profile. The solution provides general expressions for the evolution of the beam waist and radius of curvature during nonlinear propagation. Casting these solutions into the analagous ABCD matrices the authors observe that self-focussing can be viewed as the combined effect of a lens with an intensity dependent focal length *and* propagation through a negative distance (self-shortening).

The approach to the problem of self-focussing taken in this thesis is the use of a numerical solution based on the non-linear scaling of the q-parameter introduced by Belanger et. al. in 1982 [8] and studied further by Huang et. al. in 1992 [40]. Huang's description of self-focussing is particularly appealing because once the effects of self-focussing have been accounted for by a simple transformation of the q parameter, linear and nonlinear propagation can be treated identically. This procedure which forms the subject of this chapter is a valuable aid to the intuitive understanding of simple resonators and to the qualitative prediction of the effects of self-focussing on cavity modes. Further, and importantly, it lends itself easily to numerical implementation and can be used to calculate the nonlinear solution to arbitrary resonator configurations, unlike some of the analytical solutions described above.

The organization of this chapter is as follows. Section 3.2 defines Gaussian beams, the q parameter and its transformation using ABCD ray matrices. Section 3.3 describes how the effects of self-focussing can be accounted for by a nonlinear scaling of the q parameter. Section 3.4 describes the iterative program that was written to implement this technique. The code itself is included in Appendix B. Section 3.5 applies this tool to study the example of a simple lens cavity closely related to the compact femtosecond laser cavity implemented later in Chapter 5 of this thesis.

3.2 The q parameter and ABCD matrices

The Gaussian beam used to describe modes in laser resonators is a solution to the paraxial wave equation. The paraxial wave equation is unchanged under the transformation z $\longrightarrow$ z + jb. Consequently a solution to the paraxial equation can be obtained by an imaginary translation of the impulse response to the equation, and this solution defines a Gaussian beam namely,

$$u_{00}(x,y,z) = j\sqrt{\frac{kb}{\pi}}\frac{1}{z+jb}exp\left[-jk\frac{x^2+y^2}{2(z+jb)}\right] \tag{3.1}$$

$$= \frac{\sqrt{2}}{\sqrt{\pi}w}exp(j\phi)exp\left(-\frac{x^2+y^2}{w^2}\right)exp\left[\frac{-jk}{2R}(x^2+y^2)\right] \tag{3.2}$$

where

$$w^2(z) = \frac{2b}{k}(1+\frac{z^2}{b^2}) \tag{3.3}$$

$$\frac{1}{R(z)} = \frac{z}{z^2+b^2} \tag{3.4}$$

$$tan\phi = \frac{z}{b} \tag{3.5}$$

Equation 3.2 defines a wave travelling in the +z direction which has a Gaussian amplitude profile, (the width of which is determined by w(z)) and curved phase fronts with radii of curvature R(z). The minimum beam transverse radius is given by

$$w_0 = \sqrt{\frac{2b}{k}}. \tag{3.6}$$

The parameter b is called the confocal beam parameter and defines the distance over which the beam cross-sectional area expands to twice its value at the minimum beam waist position. We have that

$$b = \frac{\pi w_0^2}{\lambda} \tag{3.7}$$

It is convenient to describe the evolution of the waist and phase fronts of a Gaussian beam in terms of the minimum beam waist, w_0 as

$$w^2(z) = w_0^2(1+(\frac{\lambda z}{\pi w_0^2})^2) \tag{3.8}$$

$$\frac{1}{R(z)} = \frac{z}{z^2+(\frac{\pi w_0^2}{\lambda})^2} \tag{3.9}$$

$$tan\ \phi = \frac{z}{\frac{\pi w_0^2}{\lambda}} \tag{3.10}$$

The propagation of a Gaussian beam can also be described in terms of the so-called Gaussian beam q parameter. The q parameter is defined as

$$q = z + jb \tag{3.11}$$

Consequently the radius of curvature and the beam waist are related to the real and imaginary parts of q in the following way

$$\frac{1}{R} = Re\left[\frac{1}{q}\right] \tag{3.12}$$

$$\frac{\lambda}{\pi w^2} = Im\left[\frac{1}{q}\right] \tag{3.13}$$

The q parameter completely describes a Gaussian beam. Therefore in order to study the propagation of a Gaussian beam through any optical system it is sufficient to study the propagation of the q parameter through the system. The propagation of the q parameter through various optical elements can be easily described and it can be shown that in general the q parameter undergoes a *bilinear transformation* when propagating through a linear optical system [36]. That is,

$$q' = \frac{Aq_0 + B}{Cq_0 + D} \tag{3.14}$$

where q′ is the q parameter at the output of the system and q_0 is the q parameter at

Free space, Length l	$\begin{pmatrix} 1 & l \\ 0 & 1 \end{pmatrix}$
Material, Length l, Index n	$\begin{pmatrix} 1 & l/n \\ 0 & 1 \end{pmatrix}$
Thin lens, Focal length f	$\begin{pmatrix} 1 & 0 \\ -1/f & 1 \end{pmatrix}$
Mirror, ROC R, Angle of incidence θ Tangential plane	$\begin{pmatrix} 1 & 0 \\ -2/(R\ cos\theta) & 1 \end{pmatrix}$
Mirror, ROC R, Angle of incidence θ Sagittal plane	$\begin{pmatrix} 1 & 0 \\ -2\ cos\theta/R & 1 \end{pmatrix}$
Dielectric interface from n_1 to n_2	$\begin{pmatrix} 1 & 0 \\ 0 & n_1/n_2 \end{pmatrix}$

Table 3.1: ABCD matrices for common elements

the input. The system can then be described by a 2 × 2 matrix M, that is

$$M = \begin{bmatrix} A & B \\ C & D \end{bmatrix}. \tag{3.15}$$

ABCD matrices can be written for each element of an optical system. ABCD matrices for common elements are summarized in Table 3.1. In order to describe a complex optical system one need only multiply the corresponding individual ABCD matrices together to obtain the ABCD matrix that describes the total system. Once the output q parameter, q′, has been obtained through the application of the system ABCD matrix on the input q parameter, q_0, Equations 3.12 and 3.13 can be used to extract the beam waist and radius of curvature that completely describe the Gaussian beam at the output plane.

As stated earlier, the spatial mode in a laser resonator is given by the superposition of Gaussian modes that satisfy the boundary conditions imposed by the resonator end elements. In order to solve for the standing wave that exists in a given resonator a

simple recipe based on the q parameter and ABCD matrices can be used. If q_0 is the q parameter at one end of the resonator, and the matrix M, where

$$M = \begin{bmatrix} A & B \\ C & D \end{bmatrix} \tag{3.16}$$

describes the total round trip ABCD matrix (obtained by cascading the individual matrices for the unfolded cavity together), Equation 3.14 then describes the round trip beam propagation in the resonator. To be a steady state solution, the resonator mode must be self-consistent i.e. it must reproduce itself on the round trip. We can therefore write that

$$q' = \frac{Aq_0 + B}{Cq_0 + D} \tag{3.17}$$

$$= q_0 \tag{3.18}$$

This is a simple quadratic equation that has the solution

$$q_0 = \frac{A - D}{2C} \pm \sqrt{(\frac{A + D}{2C})^2 - \frac{1}{C^2}} \tag{3.19}$$

where the fact that

$$AD - BC = 1 \tag{3.20}$$

(which is true for all ABCD matrices relating q parameters in free space) has been used. The cavity is stable only for system configurations which produce a finite beam waist and referring to Equation 3.13 this condition translates into

$$Im(q_0) \neq 0, \tag{3.21}$$

that is referring to Equation 3.19,

$$\left(\frac{A+D}{2}\right) \leq 1 \tag{3.22}$$

3.3 Self-Focussing induced nonlinear scaling of the q parameter

Huang et. al. have formulated a model for self-focussing in a thick nonlinear medium by using non-linear scaling of the q-parameter [40]. We follow their development here. This model neglects aberrations assuming that the Gaussian nature of the beam is not modified by self-focussing. Previous work on self-focussing in a laser cavity has made similar assumptions [1, 53, 101].

As discussed in Chapter 2, self-focussing is the result of the Kerr nonlinearity which introduces an intensity dependent term in the refractive index of the medium, ie.

$$n = n_0 + n_2 I \tag{3.23}$$

For a Gaussian beam we can write that

$$I(r) = I_0 e^{-2r^2/w^2} \tag{3.24}$$

We can approximate this radially varying Gaussian intensity profile with a parabola if we restrict the analysis to excursions around the optical axis that are small compared to the beam waist w, that is if

$$2r^2/w^2 \ll 1 \;\; ie. \;\; r \ll w/\sqrt{2} \tag{3.25}$$

we can write that

$$n \;\; = \;\; n_0 + n_2 I_0 e^{-2r^2/w^2} \tag{3.26}$$

$$\sim \quad n_0 + n_2 I_0(1 - 2r^2/w^2) \tag{3.27}$$

$$= \quad (n_0 + n_2 I_0)(1 - \frac{n_2 I_0}{n_0 + n_2 I_0}\frac{2r^2}{w^2}) \tag{3.28}$$

$$\sim \quad n_0(1 - \frac{2n_2 I_0}{n_0 w^2} r^2) \tag{3.29}$$

Comparing this expression to the defining equation for an inverted parabola, i.e.

$$n = n_0\left(1 - \frac{r^2}{2h_{sf}^2}\right) \tag{3.30}$$

we can readily identify the parameter h_{sf} that determines the curvature of the index profile as

$$h_{sf} = \frac{w}{2}\sqrt{\frac{n_0}{I_0 n_2}} \tag{3.31}$$

Defining P as the power in the entire beam that is

$$P = \int_0^\infty \int_0^{2\pi} I_0 e^{-2r^2/w^2}\, r dr d\phi \tag{3.32}$$

we have that

$$P = \frac{1}{2}\pi I_0 w^2 \tag{3.33}$$

and consequently

$$h_{sf} = \frac{w^2}{2}\sqrt{\frac{n_0 \pi a}{2n_2 P}} \tag{3.34}$$

where a is a correction factor which accounts for higher order terms in the expansion of $e^{\frac{-2r^2}{w^2}}$ and has been predicted to have values in the range of about 3.7 to 6.4 [101]. A familiar system which displays a similar parabolically varying radial index profile is the Graded-Index or GRIN lens. The ABCD matrix for this element has been derived by Haus [36]. Using this analogy we can immediately write down the ABCD matrix for propagation through a thin slice, dz, of the nonlinear medium (assuming that h_{sf}

is constant over the length dz) as,

$$\begin{pmatrix} A & B \\ C & D \end{pmatrix} = \begin{pmatrix} 1 - \frac{dz^2}{2h_{sf}^2} & \frac{dz}{n_0} \\ -\frac{n_0}{h_{sf}^2} dz & 1 - \frac{dz^2}{2h_{sf}^2} \end{pmatrix} \tag{3.35}$$

Using this matrix we can derive an an equation for the differential change dq of the parameter q over an infinitesimal length dz. The details of this derivation are provided in Appendix A. The result is

$$\frac{dq}{dz} = \frac{1}{n_0} + \frac{q^2 n_0}{h_{sf}^2} \tag{3.36}$$

Since it is the real and imaginary parts of the parameter p = 1/q that are related to the radius and waist respectively as previously described in Equations 3.13 and 3.12, we translate the above equation into two differential equations describing the variation of p_r and p_i, of the real and imaginary parts of p as the beam propagates through the nonlinear medium. We get that

$$\frac{dp_r}{dz} = -\frac{p_r^2}{n_0} + \frac{(\sigma p_i)^2}{n_0} \tag{3.37}$$

$$\sigma \frac{dp_i}{dz} = -\sigma p_i \frac{2p_r}{n_0} \tag{3.38}$$

where the scaling factor σ is defined as,

$$\sigma \equiv \sqrt{1 - \frac{P}{P_{crit}}} \tag{3.39}$$

$$P_{crit} \equiv \frac{a\lambda^2}{8\pi n_0 n_2} \tag{3.40}$$

Many numerical and analytical techniques for the solution of these equations have been demonstrated. However, Huang et. al. made the important observation that under the substitution $\sigma p_i \longrightarrow p_i'$ these are exactly the equations that would describe linear propagation through a distance dz in a material of index n_0. This is very convenient because now self-focussing in a nonlinear medium can be accounted

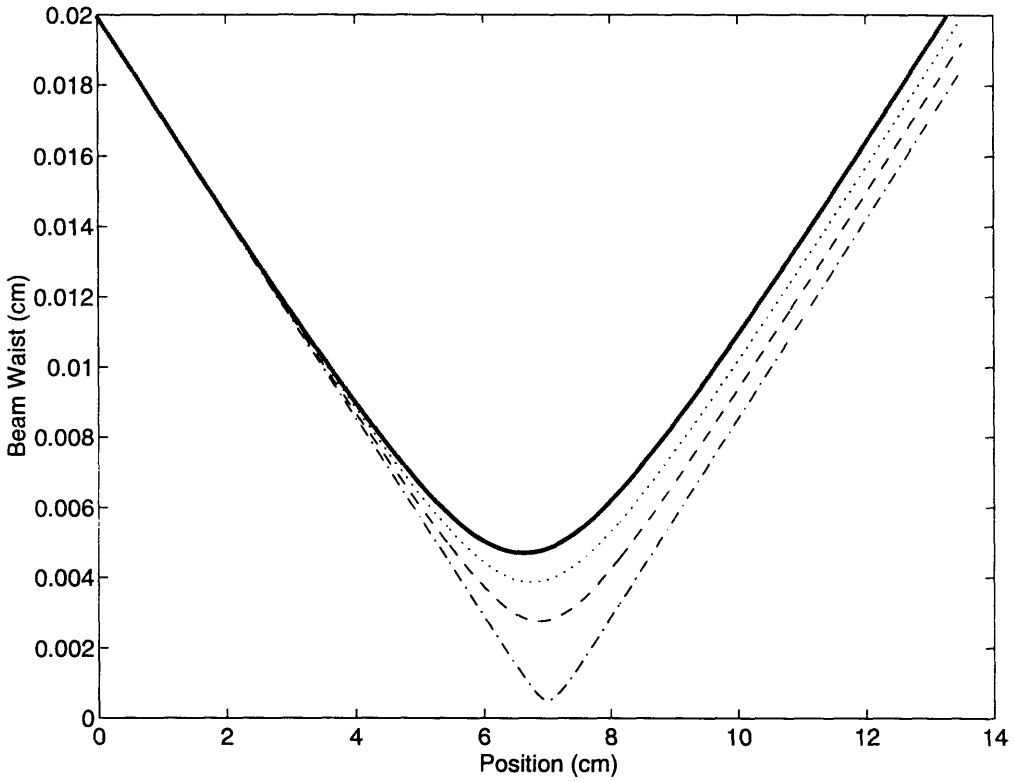

Figure 3-1: Shift in focus position resulting from the effect of self-focussing on a propagating beam. Increasing beam powers: Solid - .1 $\times$ P_{crit}, Dotted - .4 $\times$ P_{crit}, Dashed - .7 $\times$ P_{crit}, Dashdot - .99 $\times$ P_{crit}. The input beam has R = -4 cm, w = .022cm. The length of the material is 13.5 cm, the linear index $n_0 = 1.76$, and the nonlinear index $n_2 = 3\times 10^{-16}$ cm^2/W.

for simply by appropriate scaling of the q parameter upon entering and exiting the material. This treatment is also physically appealing because the effect of scaling can be clearly seen in Equation 3.37 as counteracting the diffraction of the propagating Gaussian beam.

Note that the scaling term σ is dependent on the ratio of the power P to the critical power P_{crit}. As expected σ approaches 1 for low powers. At the critical power, σ approaches 0 and the second term in Equation 3.37 vanishes signifying the cancellation of diffractive effects due to the counteracting influence of self-focussing.

Figure 3-1 provides a more physical picture of these effects of self-focussing in beam propagation. Using the above described q parameter scaling, a Gaussian beam is propagated at different powers through 13.5 cm long slab of sapphire material ($n_0 = 1.76$, $n_2 \sim 3 \times 10^{-16}$ cm^2/W, $\lambda = 800$ nm, $P_{crit} \sim 2.6$ MW). The radius of curvature and beam waist of the input beam (R = -4 cm, w = .022 cm) are chosen so that at low powers the beam comes to a focus approximately in the middle of the block of sapphire. The length of the sapphire block is approximately equal to $2n_0b$, where the confocal parameter, b, of the beam is $\sim$ 3.92 cm corresponding to a minimum beam waist of about 100 μm.

The mode profile of the propagating beam is plotted for increaseing powers upto as much as 0.99 times the critical power, $P_{critical}$. The shift of the position of minimum beam waist (or focus) is very clear. As the power is increased, self-focussing increasingly counteracts the diffractive spreading of the beam. Since the input beam radius of curvature and waist size are held constant, the effect of self-focussing manifests itself as a shift in the position at which the beam comes to focus. Clearly, at higher powers the beam travels further in the material before attaining its minimum size. Notice that for this case in which the beam focus is approximately in the middle of the block, the far field divergence is relatively constant at all powers.

For powers above P_{crit}, σ becomes imaginary and this analysis breaks down. The regime where $P \geq P_{cr}$ corresponds to the case when self-focussing effects are stronger than diffraction resulting in a positive feedback mechanism that causes the collapse of the beam to a singularity. However in most solid-state resonators peak powers are only a fraction of the critical power and so the model described above is quite appropriate and useful.

To summarize the above discussion , if we define scaling parameters Ψ and Ψ^{-1} at the entrance and exit of the nonlinear medium, the entire effect of propagation with

self-focusing is described by the transformation

$$q' = \Psi^{-1} M \Psi q \tag{3.41}$$

where we define

$$\Psi(q) = \frac{1}{Re(1/q) + j\sigma Im(1/q)} \tag{3.42}$$

and

$$\Psi^{-1}(q) = \frac{1}{Re(1/q) + j\sigma^{-1} Im(1/q)} \tag{3.43}$$

and M is the ABCD matrix that describes linear propagation through the medium.

3.4 Numerical implementation of nonlinear scaling of q-parameter

As part of this thesis, the above described method was implemented in a numerical procedure which can be used to evaluate both linear and nonlinear cavity spatial mode profiles for arbitrary resonators. The code (included in Appendix 2) was written in a stack based language ASYST which is convenient for matrix and array manipulation. The program is based entirely on the q-parameter representation of Gaussian beams and the transformation of the q parameter using ABCD matrices as described above. ABCD matrices are defined for a variety of optical elements including all those cited in Table 3.1. Procedures for the manipulation of the q parameter - propagation, extraction of the radius of curvature and beam waist - are also developed. Resonator configurations are defined by the user as cascades of the predefined individual optical elements.

For a specified resonator configuration, the program is capable of evaluating the stability of the resonator and calculating the self-consistent q parameter for stable configurations. Starting at one end of the cavity then, the beam is "propagated"

through the entire resonator using ABCD matrices. The beam waist is calculated concurrently and stored as a function of position. Thick elements are sliced into thinner slices and the q parameter and corresponding beam waist are calculated and plotted after each thin slice. Note that at the boundary between air and a nonlinear element the program calculates the beam waist in air outside the element, then calculates the beam waist after the first slice of material (using the scaling of the q parameter) and linearly interpolates between the two points. Clearly in the limit of an infintesimal slice (ie. across a boundary) the resultant mode profile would exhibit a discontinuous waist size which is physically impossible. However, it must be kept in mind that the entire analysis of Huang et. al. is performed under the assumption of *thick* nonlinear media and one cannot therefore study what happens across a dielectric boundary using this technique.

3.5 The simple lens cavity

To illustrate the utility of this program it is used to study the nonlinear properties of the simple yet enlightening resonator configuration shown in Figure 3-2. This cavity is closely related to that implemented as a compact KLM laser later in this thesis. The cavity is composed of two highly reflecting flat end mirrors and an intracavity lens of focal length f. The lengths of the two arms are L_1 and L_2. To understand this resonator the first step is to map out its linear stability region as a function of the arm lengths L_1 and L_2. The round trip ABCD matrix for the resonator is not difficult to compute and its components are

$$A = 1 - L_1/f - \frac{L_1 + 2L_2(1 - L_1/f)}{f} \tag{3.44}$$

$$B = L_1 + 2L_2(1 - L_1/f) + L_1\left(1 - L_1/f - \frac{L_1 + 2L_2(1 - L_1/f)}{f}\right) \tag{3.45}$$

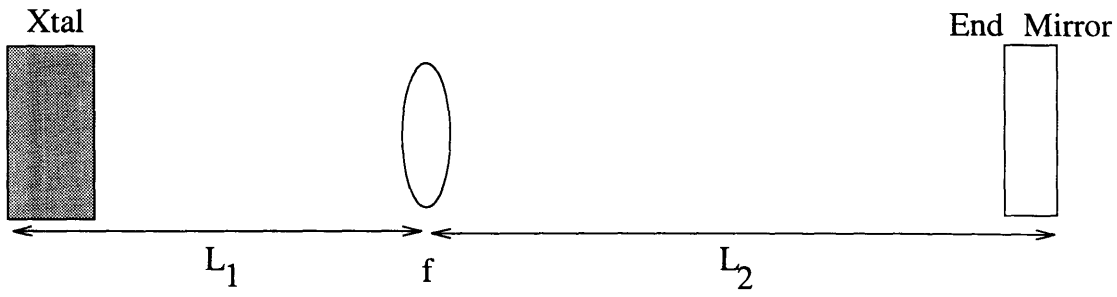

Figure 3-2: Simple lens cavity

$$C = -1/f - \frac{1-2L_2/f}{f} \tag{3.46}$$

$$D = 1 - 2L_2/f + L_1\left(-1/f - \frac{1-2L_2}{f}\right) \tag{3.47}$$

The stability condition of Equation 3.22 for this resonator is

$$\left(\frac{f^2 - 2fL_1 - 2fL_2 + 2L_1L_2}{f}\right)^2 \leq 1. \tag{3.48}$$

This equation can be written as a function of the quantities L_1/f and L_2/f ie.

$$[(1-\frac{L_1}{f})(1-\frac{L_2}{f})]^2 \leq 1 \tag{3.49}$$

Solving this inequality results in the identification of the stable resonator configurations which lie in the shaded regions of the stability diagram of Figure 3-3. At any one point in this two-dimensional parameter space, the program can be used to plot the linear and nonlinear spatial profiles of the intracavity resonator mode. As will be discussed shortly, different points on the stability map exhibit qualitatively different linear and nonlinear mode profiles.

Before proceeding to study specific profiles, it is instructive to plot the linear

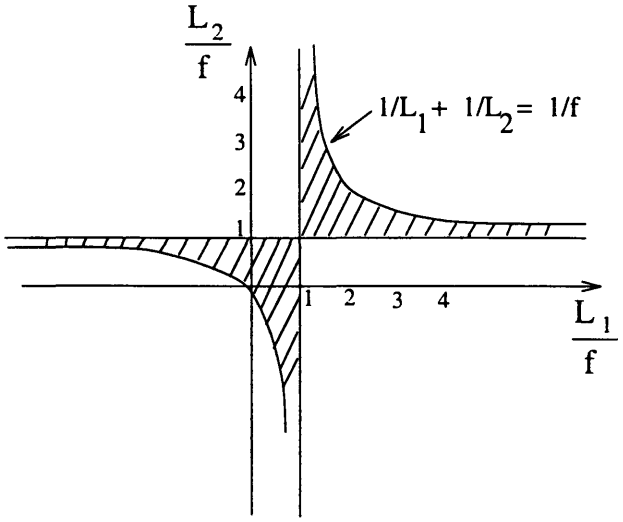

Figure 3-3: Stability diagram for simple lens cavity. The shaded region denotes the parameter space which corresponds to a stable resonator configuration.

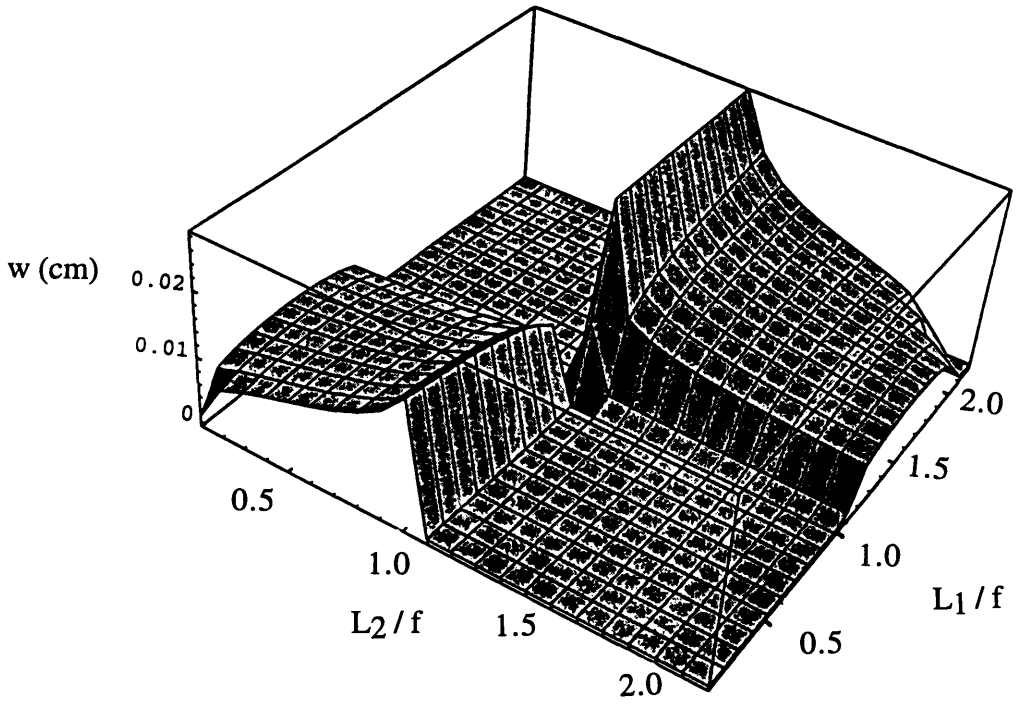

Figure 3-4: Mode size at end mirror M_1 of simple lens cavity plotted as a third dimension over the cavity stability diagram.

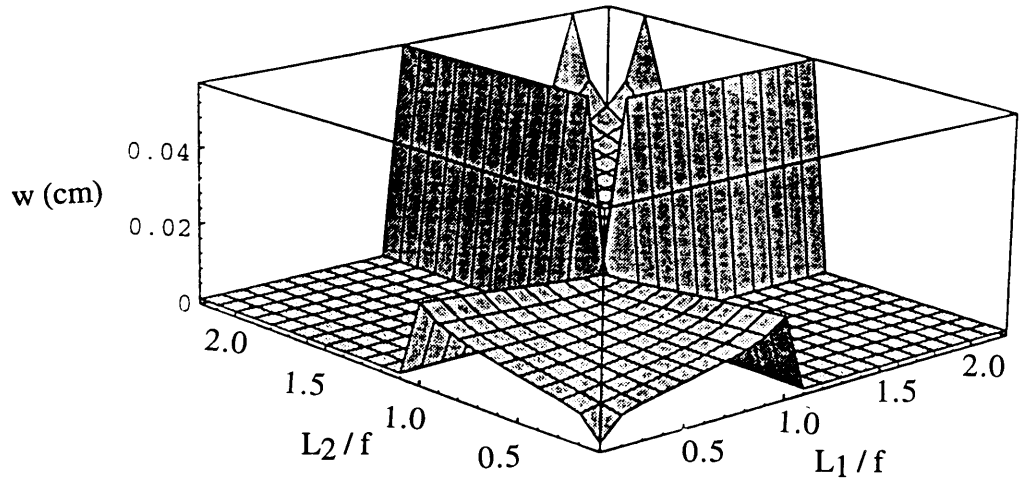

Figure 3-5: Mode size at intracavity lens position of simple lens cavity plotted as a third dimension over the cavity stability diagram

modesize at different points in the resonator as a third dimension over the stability diagram of Figure 3-3. Figure 3-4 plots the mode size at the end mirror M_1 of the resonator corresponding to the arm of length L_1. The general nature of the surface plot agrees with physical intuition. For resonator configurations where $L_1 \sim f$, the Gaussian mode is focussed tightly at M_1 and collimated at the other end of the cavity. Consequently the surface plot of beam size at the mirror M1 dips to zero along the line $L_1 = f$. By an analagous argument it is clear that when L_2 approaches f the modesize at M_1 rises rapidly due to the collimation of the beam in arm 1 and its focussing at mirror M_2. For L_1 and L_2 much less than f, the resonator mode at both ends of the cavity is collimated. Along the hyperbola in the stability diagram of Figure 3-3 where the condition

$$\frac{1}{L_1} + \frac{1}{L_2} = \frac{1}{f} \tag{3.50}$$

is met, the imaging condition of ray optics prevails and the mode size at M_1 shrinks

again.

The 3D mode picture at mirror M_2 can be surmised from Figure 3-4 by simply interchanging the axes corresponding to L_1 and L_2. Figure 3-5 shows the 3D plot for mode size at the intracavity lens. This plot is symmetric with respect to L_1 and L_2 as one would expect physically. The qualitative trends can easily be traced in a manner similar to that just done for Figure 3-4

Having a basic understanding of the linear behavior of the cavity we can now calculate representative mode profiles in order to understand the influence of self-focussing. Figures 3.5 through 3.12 are a series of linear and nonlinear mode profile plots, each obtained at a different point in the stability map of the cavity. All of these simulations utilize the same cavity configuration with a lens of focal length 5 cm and a Ti:Al_2O_3 crystal of length 0.3 cm. The nonlinear mode is calculated at a power equal to one half of the critical power. For Ti:Al_2O_3 the critical power is on the order of 2.6 MW and one half of that is a reasonable estimate for the peak power in a typical femtosecond Ti:Al_2O_3 oscillator.

Table 3.2 compares these operating points by tabulating several important parameters. Figure 3-14 provides a quick reference for the approximate positions (in the stability map of the cavity) of the points tabulated in Table 3.2. The parameters tabulated for each point include the linear and nonlinear beam waists (w_l and w_{nl}) at the crystal, the resultant saturable absorber action, γ (ie. the differential change in mode area per unit power, at the crystal high reflector) and the self phase modulation per unit power ie. δ. Note that δ is calculated as

$$\delta = \frac{2\pi}{\lambda} n_2 \frac{1}{A_{eff}} \, b \tan^{-1}(\frac{l}{b}) \tag{3.51}$$

where b is the confocal parameter of the beam, l is the crystal length and

$$A_{eff} = \pi w_{nl}^2. \tag{3.52}$$

Γ is calculated as

$$\Gamma = \frac{1}{.5 * P_{crit}} \frac{A_{nl} - A_l}{A_l}. \tag{3.53}$$

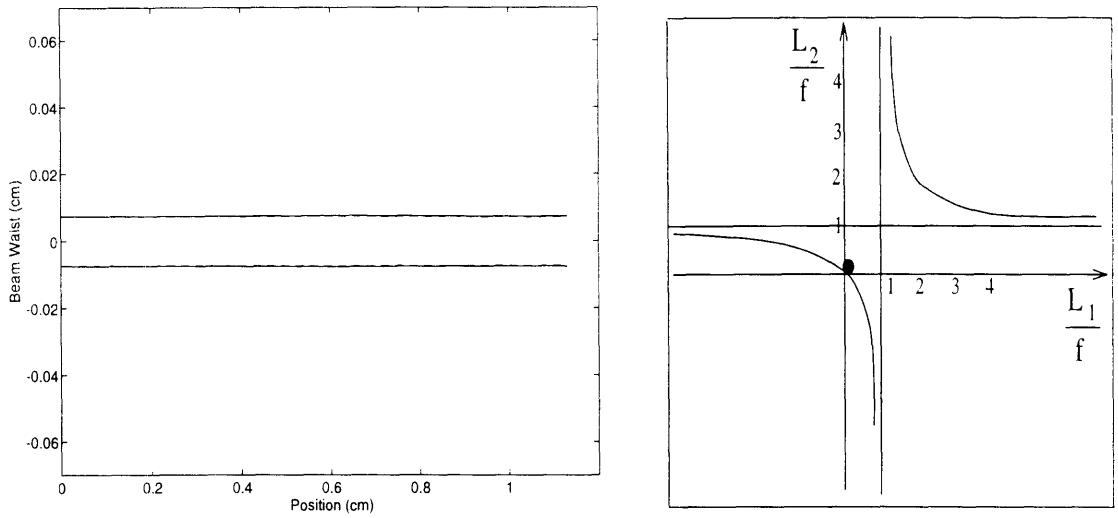

Figure 3-6: $L_1 = L_2 = 0.1$, Left: Mode profiles. Solid line - low intensity, Dotted line - High Intensity. Right: Stability position

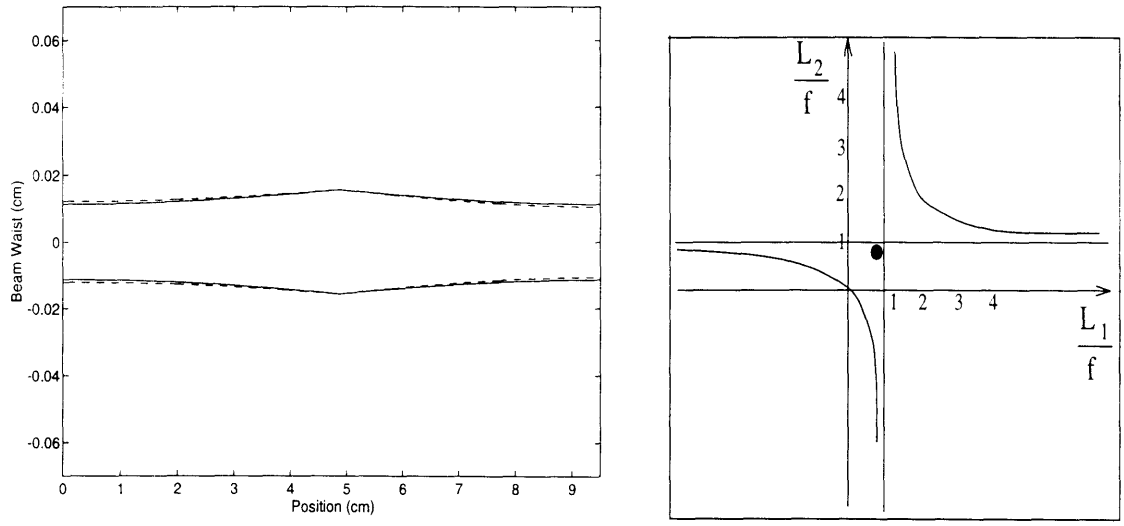

Figure 3-7: $L_1/f = L_2/f = 0.95$, Left: Mode profiles. Solid line - low intensity, Dotted line - High intensity. Right: Stability position

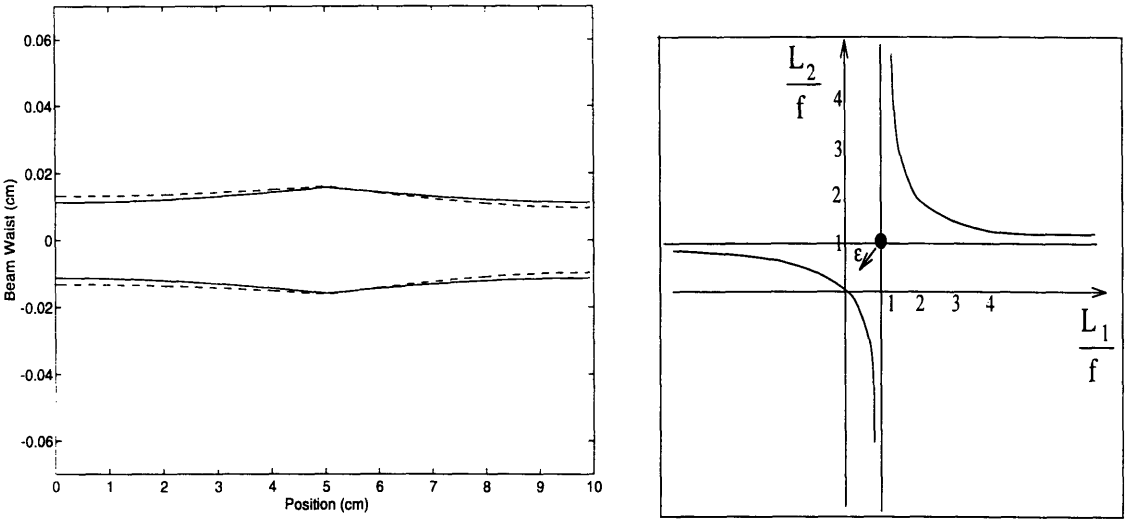

Figure 3-8: $L_1/f = L_2/f = 0.98$, Left: Mode profiles. Solid line - low intensity, Dotted line - high intnsity. Right: Stability position, ϵ is a small distance.

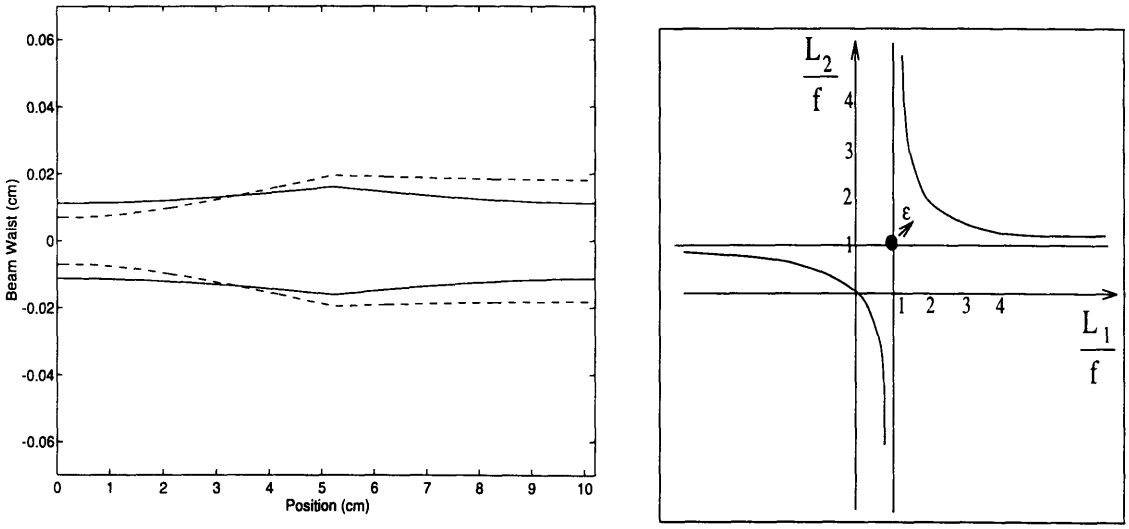

Figure 3-9: $L_1/f = L_2/f = 1.02$, Left: Mode profiles. Solid line - low intensity, Dotted line - high intensity. Right: Stability position, ϵ is a small distance.

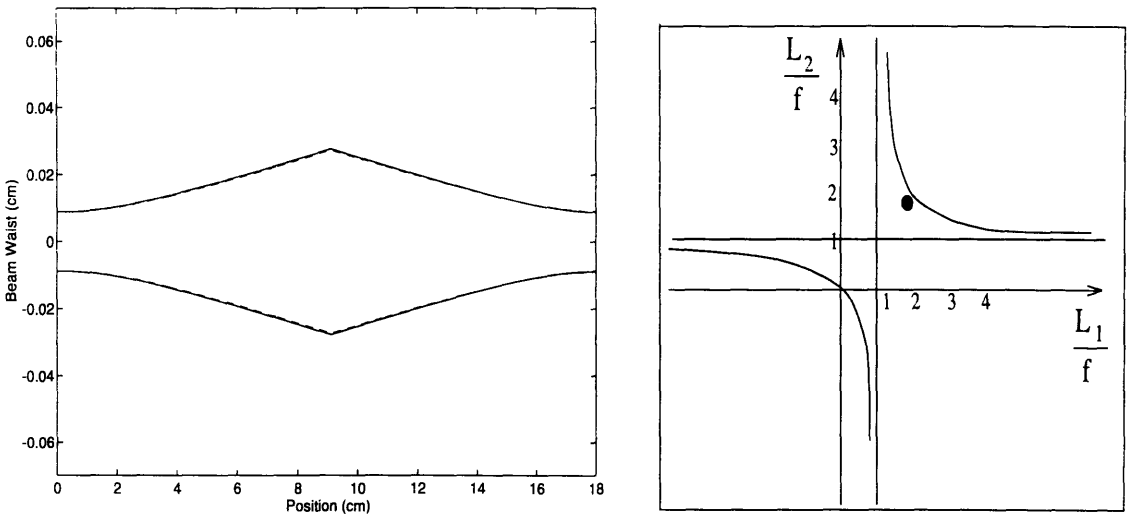

Figure 3-10: $L_1/f = L_2/f = 1.8$, Left: Mode profiles. Solid line - low intensity, Dotted line - high intensity. Right: Stability position

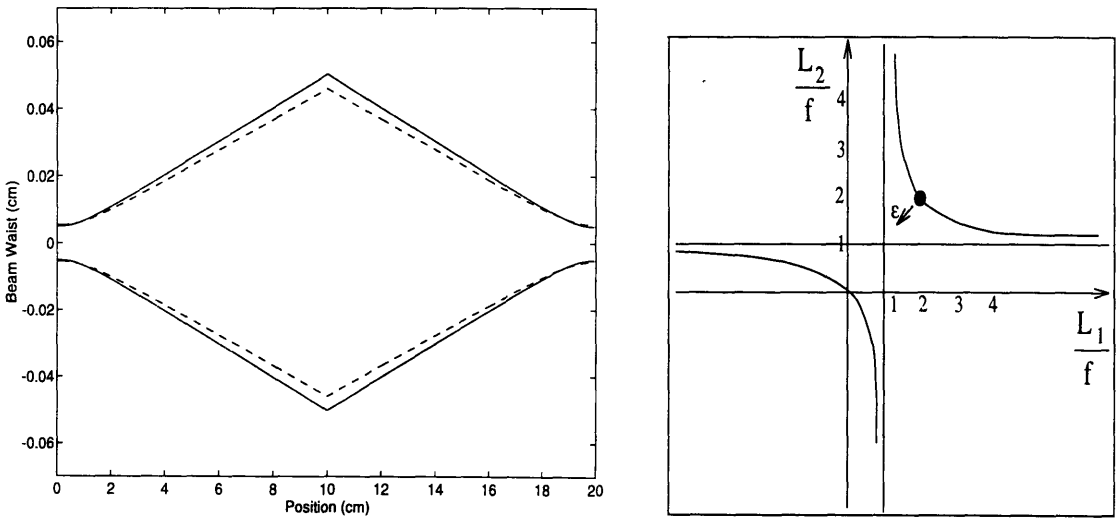

Figure 3-11: $L_1/f = L_2/f = 1.98$, Left: Mode profiles. Solid line - low intensity, Dotted line - high intensity. Right: Stability position, ϵ is a small distance.

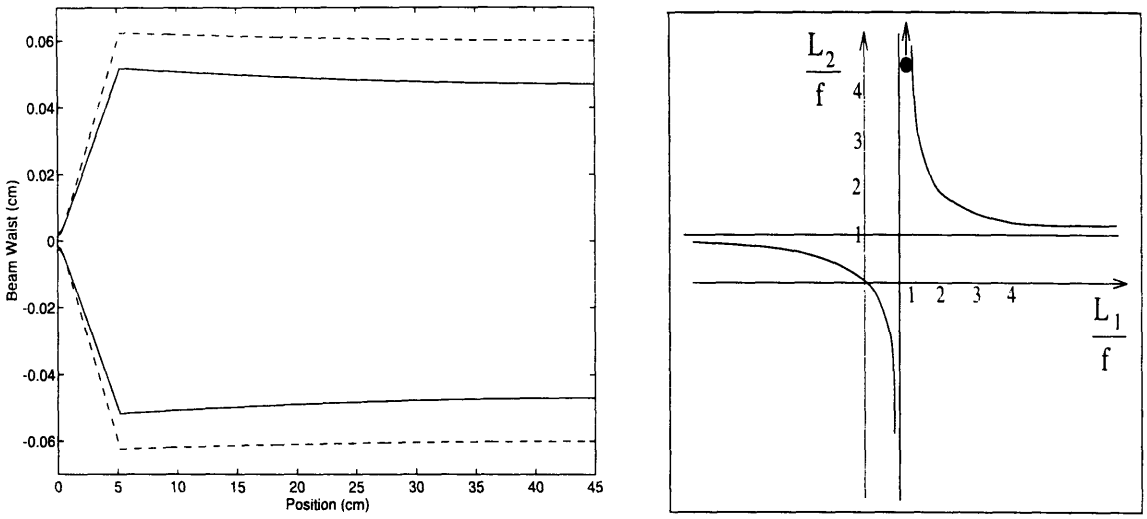

Figure 3-12: $L_1/f = 1.02$, $L_2/f = 8$, Left: Mode profiles. Solid line - low intensity, Dotted line - high intensity. Right: Stability position

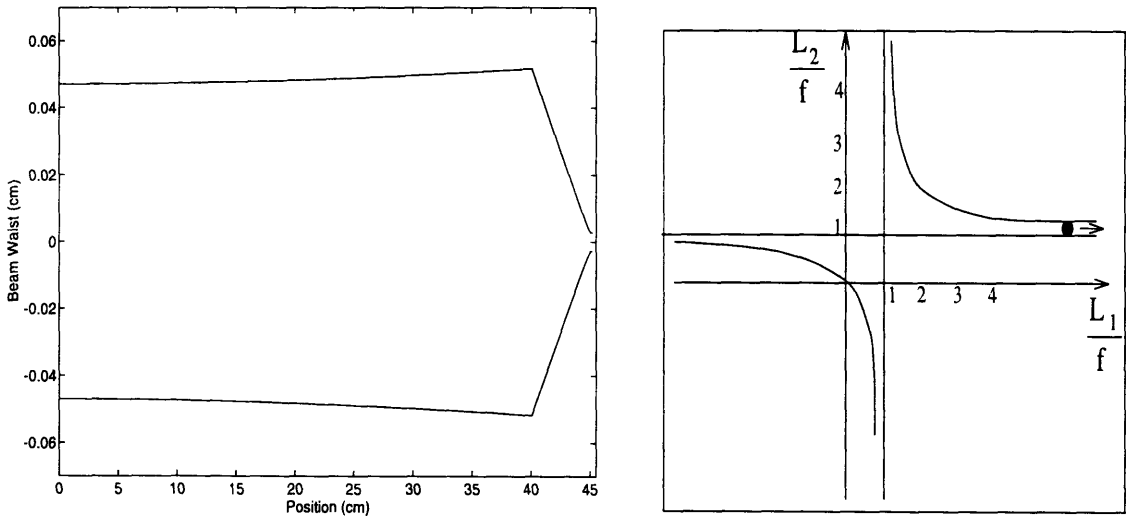

Figure 3-13: $L_1/f = 8$, $L_2/f = 1.02$, Left: Mode profiles. Solid line - low intensity, Dotted line - high intensity. Right: Stability position

This type of comparison can shed light on several KLM laser design issues. The size of the mode in the crystal is a key parameter in obtaining sufficient power extraction from the gain and in choosing an appropriate pump focal spot. Typical Ti:Al_2O_3 lasers require focussed spot sizes in the gain of about 30 to 50 μm. Consequently with current crystal technology operating point 8, with its spot size in the crystal of approximately 0.5 mm would be unsuitable even from a continuous wave laser standpoint.

The suitability of a given operating point for KLM operation can also be estimated. For example, if pump beam aperturing is intended then the requirement of a negative differential mode size at the crystal for KLM limits operation to points 1, 4 or 7. The choice of pump spot size also becomes clear, since the pump beam must provide an effective aperture to distinguish between linear and nonlinear modesizes in the crystal. Ideally it should be exactly the size of the nonlinear mode in the crystal. Similarly if hard aperturing with a slit is intended, an appropriate position and size for the slit can be ascertained at each operating point.

Stability of modelocked operation and favorability for self-starting behavior can be determined by comparing saturable absorber action at different positions. From this point of view, operating points 4 and 7 offer the best possibilities. For short pulse generation in the positive dispersion regime one would seek to enhance the γ/δ ratio of saturable absorber action to self-phase modulation as predicted by Haus [35] by working close to stability boundaries at points 3, 4, 6 or 7. Figure 3-15 plots this ratio of γ/δ as a function of the parameter $L_1/f = L_2/f$, along the line corresponding to equal resonator arm lengths. The trend of maximization of this ratio close to the stability boundaries is seen clearly in this plot.

It is also interesting to investigate operation of the cavity around the confocal instability point at which

$$\frac{L_1}{f} = \frac{L_2}{f} = 1. \tag{3.54}$$

Operation around this point results in enhancement of nonlinear mode changes be-

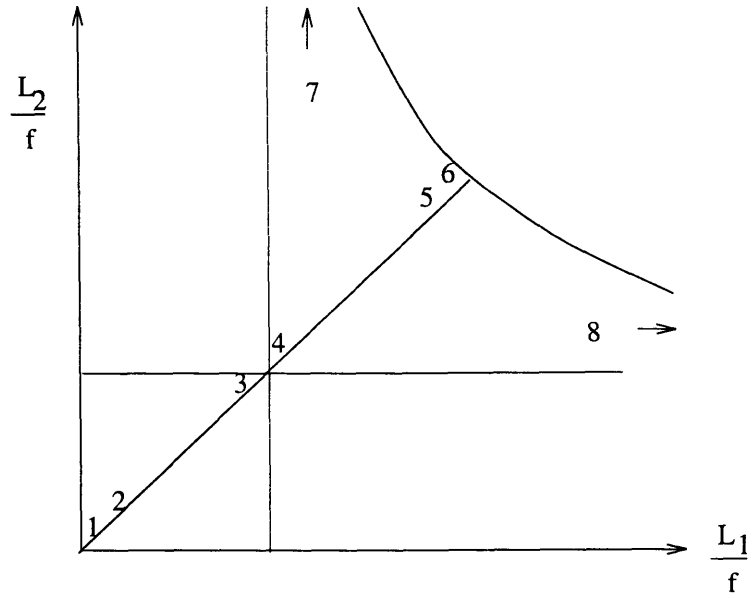

Figure 3-14: Approximate position in the cavity stability map of the points 1 through 8 that are tabulated in Table 3.2

Pt.	L_1/f	L_2/f	w_l (cm)	w_{nl} (cm)	b (cm)	$\Delta w/w$ %	γ (1/W)	δ (1/W)	γ/δ
1	0.1	0.1	7.45e-3	7.32e-3	2.09	-2.7	-2.1e-8	4.2e-8	-0.49
2	0.95	0.95	1.13e-2	1.21e-2	5.75	14.7	1.1e-7	1.5e-8	7.34
3	0.98	0.98	1.13e-2	1.32e-2	6.84	36.5	2.8e-7	1.3e-8e-8	21.73
4	1.02	1.02	1.13e-2	7.01e-3	1.92	-61.6	-4.7e-7	4.6e-8	-10.41
5	1.8	1.8	8.74e-3	8.77e-3	3.04	2.31	1.8e-8	2.9e-8	0.61
6	1.98	1.98	5.03e-3	5.46e-3	1.19	21	1.6e-7	7.3e-8	2.21
7	1.02	8	2.51e-3	1.8e-3	0.13	-48.6	-3.73e-7	3.4e-7	-1.1
8	8	1.02	4.73-2	4.7e-2	1.27	0.0	0.0	1.02e-9	0.0

Table 3.2: Comparison of linear and nonlinear parameters at different operating points in the simple lens cavity. w_l, w_{nl} are the linear and nonlinear mode waists in cm at the crystal high reflector. b is the confocal parameter of the nonlinear mode in cm. $\Delta w/w$ gives the percent change in mode area. γ is the differential change in mode area per unit power and δ is the SPM per unit power. The ratio γ/δ is dimensionless. All calculations use a 5 cm focal length lens, a 0.3 cm Ti:Al_2O_3 crystal and a power of $.5P_{cr}$ for the nonlinear mode.

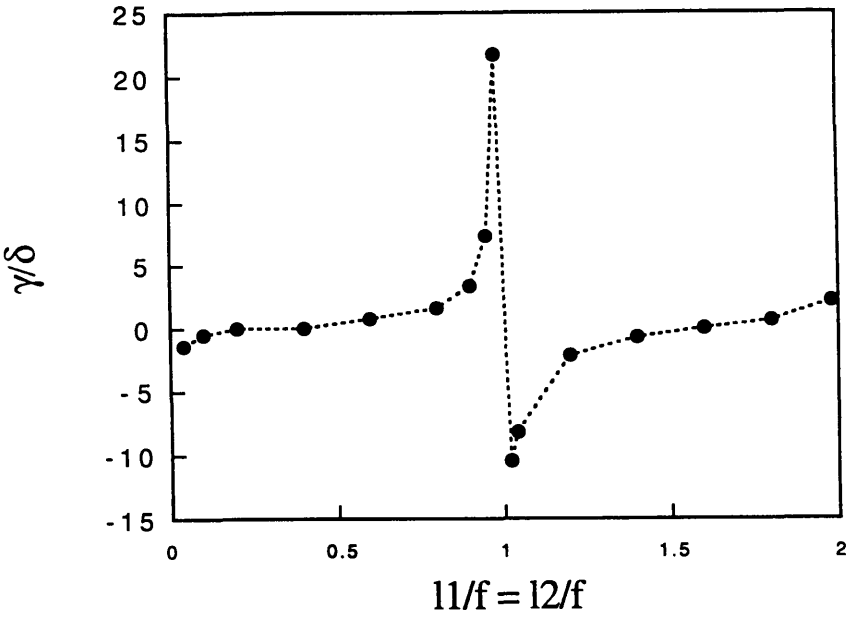

Figure 3-15: The ratio of saturable absorber action (γ) to self-phase-modulation (δ) is plotted as a function of the equal arm lengths normalized to the focal length. Note the enhancement of this factor that is possible at the expense of geometric stability of the cavity.

cause of the proximity to two of the three cavity instability boundaries. However one must be cautious in choosing an operating point here, because small changes in position can alter the effects of self-focussing *both* in *sign* and in magnitude. Figure 3-16 shows a few representative operating points that have been chosen close to the confocal instability point. Points A and A′ which lie along the line where $L_1 = L_2$ were also included in Table 3.2 as Points 3 and 4 respectively. Figures 3-17 through 3-22 display the linear and nonlinear modes corresponding to these six points of operation indicated in Figure 3-16. Table 3.3 compares key parameters at the various points.

Several important observations can be made from this comparison. First it is important to notice the qualitative differences in the nonlinear behavior at these points. In particular the nonlinearity *changes* sign in going across the confocal instability point, since for points A, B and C where L_1 and L_2 are less than f, the nonlinear mode in the crystal is *larger* than the linear mode and for points A′, B′ and C′ where L_1 and L_2 are greater than f, the nonlinear mode is *smaller* than the linear mode.

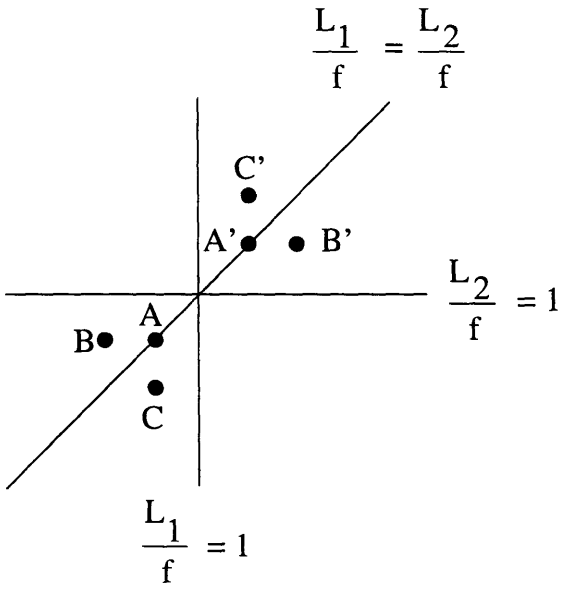

Figure 3-16: Operating points close to the confocal instability point where $\frac{L_1}{f} = \frac{L_2}{f} = 1$

Pt.	L_1/f	L_2/f	w_l (cm)	w_{nl} (cm)	b (cm)	$\Delta w/w$ %	γ (1/W)	δ (1/W)	γ/δ
A	0.98	0.98	1.13e-2	1.32e-2	6.84	36.5	2.8e-7	1.3e-8	21.7
B	0.96	0.98	1.34e-2	1.46e-2	8.37	18.5	1.4e-7	1.1e-8	13.5
C	0.98	0.96	9.49e-3	1.11e-2	4.80	35.8	2.7e-7	1.8e-8	15.0
A′	1.02	1.02	1.13e-2	7.0e-3	1.92	-61.6	-4.7e-7	4.6e-8	-10.84
B′	1.02	1.04	1.34e-2	1.17e-2	5.36	-24.3	-1.8e-7	1.6e-8	- 24.3
C′	1.04	1.02	5.03e-3	5.46e-3	1.37	-60.7	-4.7e-7	6.4e-8	-7.33

Table 3.3: Comparison of linear and nonlinear parameters at different operating points close to the confocal instability point in the simple lens cavity(see Figure 3-16. w_l, w_{nl} are the linear and nonlinear mode waists in cm at the crystal high reflector. b is the confocal parameter of the nonlinear mode in cm. $\Delta w/w$ gives the percent change in mode area. γ is the differential change in modearea per unit power and δ is the SPM per unit power. The ratio γ/δ is dimensionless. All calculations use a 5 cm focal length lens, a 0.3 cm Ti:Al_2O_3 crystal and a power of $.5P_{cr}$ for the nonlinear mode.

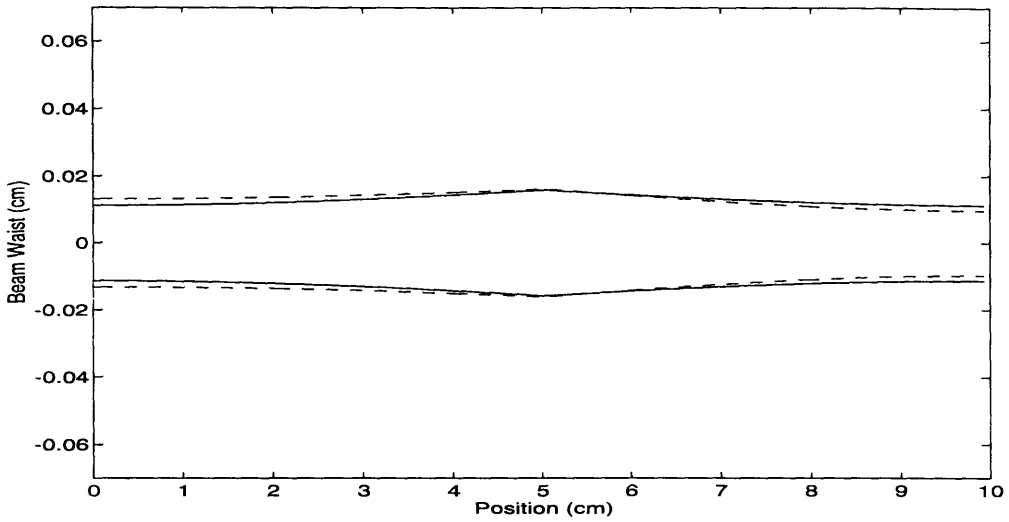

Figure 3-17: $L_1/f = .98$, $L_2/f = .98$. Low intensity (solid) and high intensity (dashed) mode profiles corresponding to point A in Figure 3-16

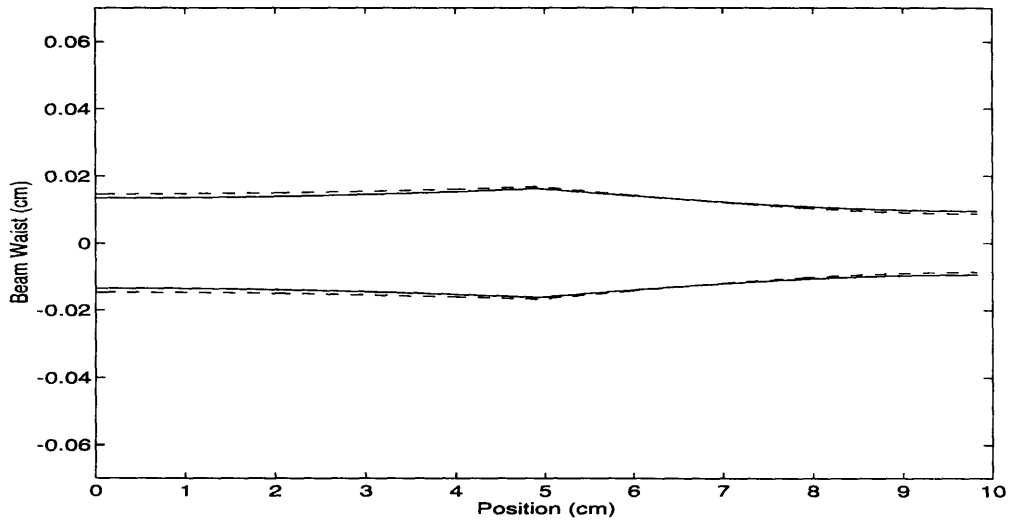

Figure 3-18: $L_1/f = .96$, $L_2/f = .98$. Low intensity (solid) and high intensity (dashed) mode profiles corresponding to point B in Figure 3-16

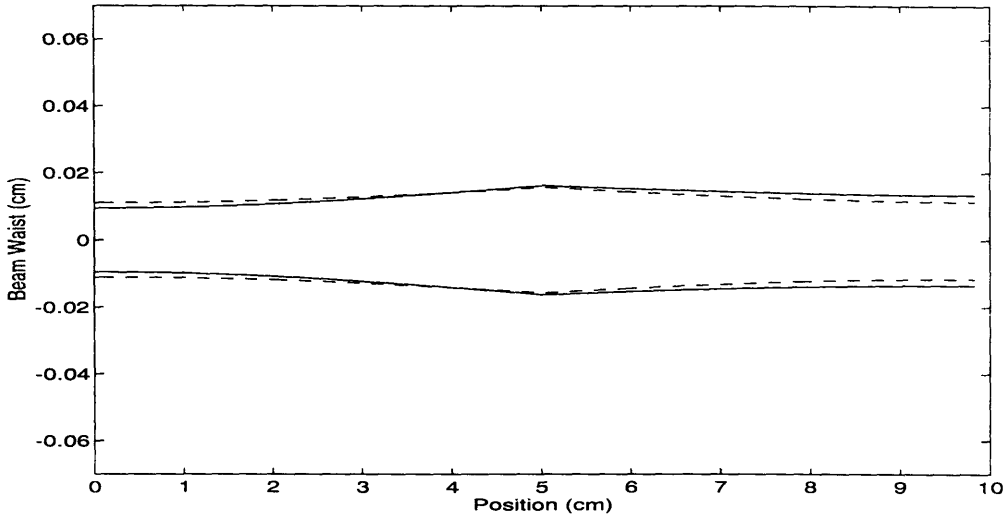

Figure 3-19: $L_1/f = .98$, $L_2/f = .96$. Linear (solid) and Nonlinear (dashed) mode profiles corresponding to point C in Figure 3-16

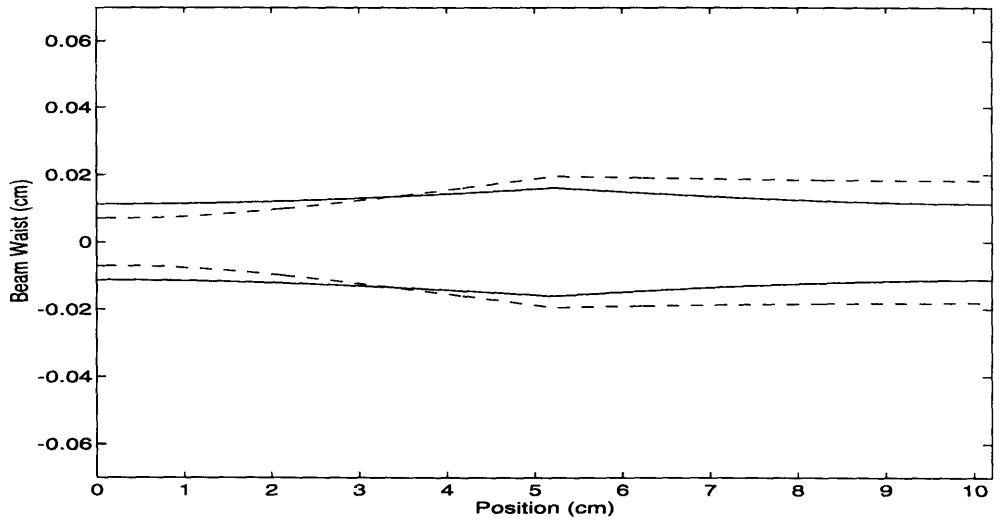

Figure 3-20: $L_1/f = 1.02$, $L_2/f = 1.02$. Low intensity (solid) and high intensity (dashed) mode profiles corresponding to point A′ in Figure 3-16

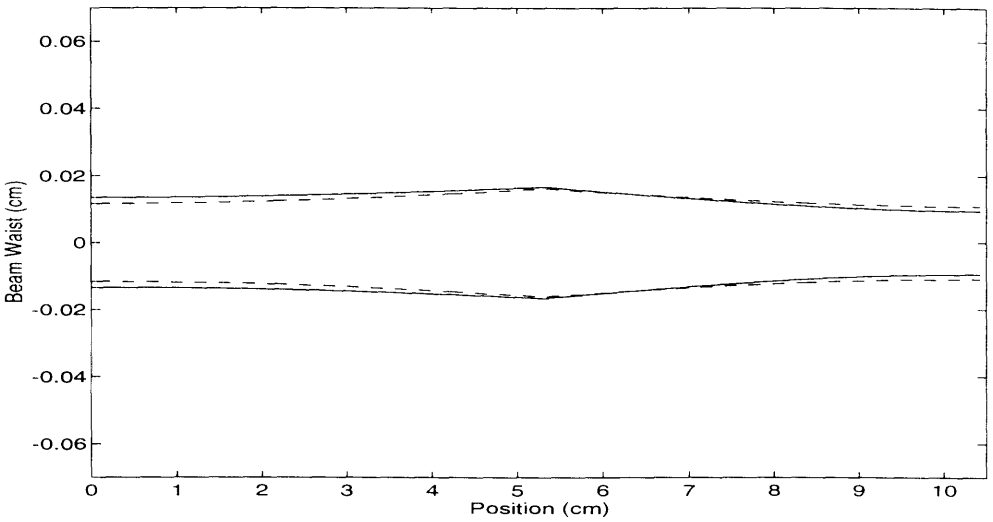

Figure 3-21: $L_1/f = 1.04$, $L_2/f = 1.02$. Low intensity (solid) and high intensity (dashed) mode profiles corresponding to point B′ in Figure 3-16

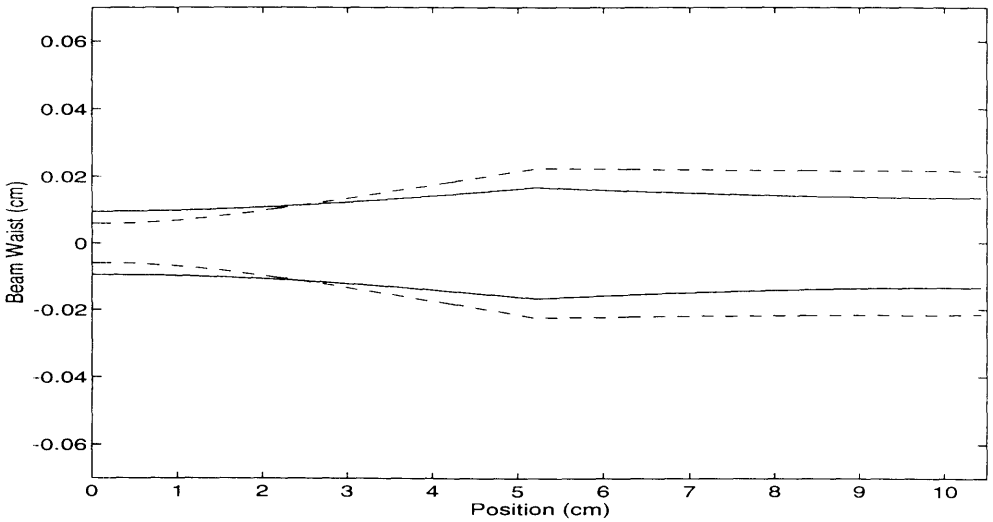

Figure 3-22: $L_1/f = 1.02$, $L_2/f = 1.04$. Low intensity (solid) and high intensity (dashed) mode profiles corresponding to point C′ in Figure 3-16

It also appears that proximity to the instability boundary where $L_1 = f$ (with L_1 being the length of the arm containing the nonlinear gain medium), favors large negative changes in modesize due to self-focussing. In a very simple picture (which appears to be valid at the operating points that were investigated) one can think qualitatively of self-focussing as just causing a shortening of the arm containing the nonlinear medium. Using this as a guideline, one can move along the linear stability map of the cavity (Figure 3-4) to predict the sign and nature of the changes in resonator mode that will occur due to nonlinear self-focussing. It must be noted that this model is oversimplified and a systematic study of its valididty has not been done.

However this model appears to be a useful qualitative guide to the effects of self-focussing. Along the line of symmetry where $L_1 = L_2$ the mode profile in the resonator appears symmetric around the lens, as one would expect physically. If one is at point A, self-focussing results in a shortening of the arm L_1, de-symmetrizing the mode profile and causing the nonlinear mode to be more focussed in the longer L_2 arm which is the arm whose length is now closest to one focal length. The same reasoning holds for point B except that one does not begin with a symmetric linear mode. The nonlinearity just makes the mode profile more asymmetric causing a greater degree of focussing in the arm whose length is closer to a focal length ie. L_2. At point C, one begins with an asymmetric mode, more focussed in the arm corresponding to L_1 since L_1 is now the arm whose length is closest to one focal length. Self-focussing "reduces" the length of L_1 and therefore makes the mode profile more symmetric. At all three points (A, B, C) the increase in modesize at the crystal due to self-focussing precludes the use of the pump beam as an aperture.

The changes occuring at points A′, B′ and C′ can be traced by analogous reasoning. Operation at points A′ or C′, appears to produce the largest magnitude of saturable action. At point A′ the linear mode profile is symmetric around the intracavity lens and the assymmetric nonlinear mode is characterized by a tighter focus in the crystal, due to the self-focussing-induced approach towards the $L_1 = f$ border. Similarly at

point C′, the asymmetric linear mode (more focussed in the arm corresponding to L_1) becomes even more asymmetric as a result of self-focussing. It appears that proximity to the $L_1 = f$ border (where L_1 is the arm containing the nonlinear medium) is important in maximizing the saturable absorber action occuring in the crystal. This issue is discussed further in Chapter 5 where operation of the compact KLM laser at point 7 of Table 3.2 is discussed. Once again it is found both theoretically and experimentally that proximity to the $L_1 = f$ border is a dominant force in producing strong saturable absorber action in the gain crystal.

Analyses and comparisons such as those just presented were valuable in this thesis for deciding on the appropriate geometry, operating point and laser parameters for use in the compact KLM resonator to be described in Chapter 5. It must be stressed that the numerical tool that has been provided should only be used as a preliminary guideline for simple resonator configurations. Complex effects such as astigmatism, thermal lensing, non uniform gain, and higher order modes are not included in this model. These are all very real and important influences on the operation of a KLM laser. Consequently the program provided is meant to be used as a starting point for simple KLM resonator design. Once a given resonator has been implemented its performance must be individually evaluated and appropriately optimized.

Chapter 4

Microdot mirror modelocking

4.1 Introduction

Passive modelocking with the use of intracavity, solid-state nonlinearities alone, became a topic of active research following the re-emergence of solid-state laser gain media in the late 1980s. Interest lay primarily in further enhancing the convenience of a solid-state gain medium by finding a reliable modelocking technique that required only bulk solid-state nonlinearities. Early methods to passively modelock solid-state lasers had included the use of organic dyes as saturable absorbers as well as some preliminary attempts at the use of all-optical intracavity modulaters [14, 91, 79]. These techniques were limited by their inconvenience and weak nonlinear response respectively. A major breakthrough in this field had been the invention of the soliton laser [75]. The further realization that soliton-like action in the external cavity was not necessary for pulse shortening [11], lead to the theory of Additive Pulse Modelocking (APM) [43, 34] on which the next generation of coupled-cavity passively modelocked solid-state lasers [30, 29, 64] was based. APM relies on the self-phase-modulation (SPM) nonlinearity occuring in an external cavity, the SPM being generated in a nonlinear fiber placed therein. Undoubtedly a powerful and versatile concept, APM in solid-state lasers suffered from the drawback of complexity due to the need for

interferometric control in order to stabilize the length of the external cavity to a degree of high accuracy. Further, the presence of fiber detracted from the convenience of the system due to familiar experimental inconveniences of a fiber medium namely its fragile nature and low coupling efficiency. Resonant passive modelocking using a semiconductor anti-resonant Fabry-Perot saturable absorber (AR-FPSA) in a coupled cavity scheme had emerged as a promising and relatively convenient technique [49].

Following these developments, the use of *intracavity bulk* nonlinearities which would eliminate altogether the need for coupled cavity schemes was viewed as highly desirable. Modelocking with intracavity nonlinear fiber mirrors and Kerr-rotation effects in fibers had been demonstrated [13, 41, 37] but once again, the inconvenience of fiber was a fundamental limitation. Against this backdrop came the revolutionary discovery of "self-modelocking" in the Ti:Al_2O_3 medium by Spence et. al in 1991 [104]. Their discovery demonstrated that ultrashort pulses could be generated by using the nonlinearities such as the Kerr effect arising in the gain medium itself [83, 51]! Prior to this demonstration self-focusing had been considered a deleterious effect in high power modelocked lasers and efforts to minimize its effects or to reduce it were usually taken. Spence's startling discovery suggested that intracavity mode profile changes due to self-focusing may in fact be *exploited* to create saturable absorber action in a surprisingly simple manner.

Soon after this first demonstration, Negus et. al. [107] and others [83, 28] studied self-modelocking by modeling the effect of self-focusing on the Gaussian mode in the entire cavity. With the results of their model Negus et. al. chose the optimal intracavity position to place an aperture, that being the position where maximal amplitude difference between low power (linear) and high power (nonlinear) resonator modes occurred. With this approach they significantly optimized and controlled the process producing sub 100 fs pulses with almost a Watt of power. They termed this technique Kerr Lens Modelocking (KLM) and their research formed the basis for a robust sub-100 femtosecond laser product namely the Coherent MIRA 900 laser.

Concurrent with these developments and as part of this thesis, efforts to develop alternative intracavity modelocking techniques were also underway. The use of Kerr-induced polarization rotation for passive modelocking was demonstrated [14, 27] in our laboratory as was the technique of microdot mirror modelocking [26, 87] which forms the subject of this chapter. Microdot mirror modelocking was first demonstrated in a laser-pumped, medium power Ti:Al_2O_3 system and subsequently extended to a lamp-pumped, high power Nd:YLF system. This chapter describes these experiments and discusses the potential of the microdot mirror modelocking technique. Section 4.2 describes the concepts of microdot mirror modelocking and its theoretical analysis as developed by Huang et. al. [40]. The fabrication of the microdot mirror structures is also detailed. Section 4.3 describes the application of microdot mirror modelocking to modelock a Ti:Al_2O_3 laser. Section 4.4 describes the extension of the technique to a lamp-pumped Nd:YLF medium. Section 4.5 concludes with a discussion of the advantages, limitations and future potential for the microdot mirror modelocking technique.

4.2 The microdot mirror modelocker

The microdot mirror modelocker is pictured schematically in Figure 4-1. The idea of the microdot mirror device is credited to David Huang, following his investigation of the description of self-focusing as a nonlinear-scaling of the q-parameter. It consists of an anti-reflection coated lens, that serves to focus the intracavity laser beam into a glass substrate. The substrate material and thickness determine the nonlinearity introduced and the choice of these parameters will be discussed shortly. The front surface of the mirror is antireflection coated in order to minimize intracavity losses. A broad-band, high damage-threshold coating is used. In addition the substrate is also wedged at 1 degree to eliminate spurious reflections which can interfere with the modelocking process [33].

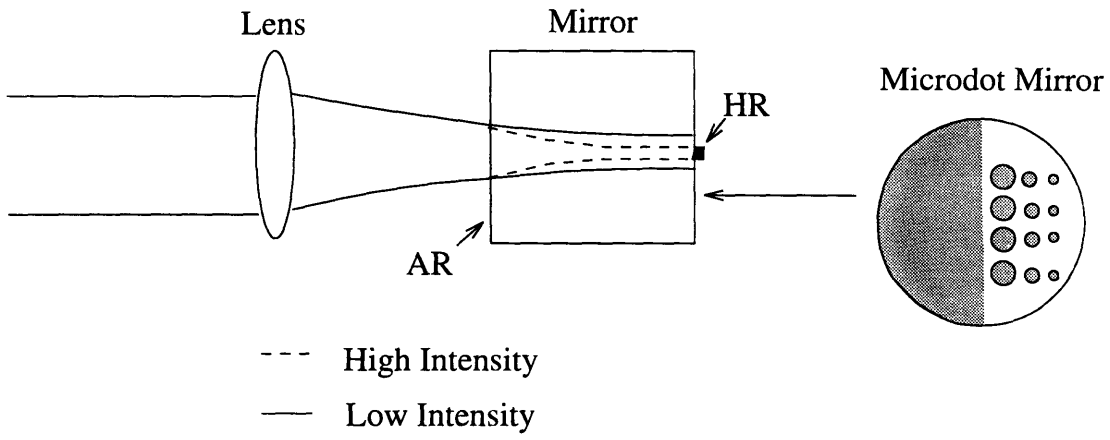

Figure 4-1: Schematic of the microdot mirror modelocker. The beam is focused by the input lens L into an antireflection-coated glass substrate that has high-reflectivity microdots on the rear surface. Nonlinear self-focusing in the glass results in a smaller focal spot at the patterned rear surface. The mirror pattern facilitates alignment and adjustment of the linear and nonlinear mirror reflectivity

The rear surface of the modelocker is patterned with a high-reflector pattern. Approximately one half of the mirror is uniformly high reflector coated and the other half is patterned into a series of microdots of decreasing size from column to column. Each row of microdots is identical in pattern to the others.

microdot mirrors were patterned using standard photolithography and wet-etching techniques. The substrates were ordered with intially uniform anti-reflective and high-reflective coatings on the two faces. The substrates were then solvent cleaned in a standard fashion using acetone followed by methanol followed by nitrogen. KTI 820-20 photo-resist was then painted on the anti-refelective surface, followed by baking for 25 minutes at 90 degrees. To avoid damage to the exposed high reflective coating the temperature was ramped gradually - taking about 1 hr to reach the requisite temperature. KTI 820-20 photo-resist was then spun on the high-reflective coating spinning at 2000 RPM for about 30 secs. The resist was baked again at 90 degrees for 25 minutes. The resist was then exposed through a positive chrome mask to ultraviolet light of 365 nm at an intensity of 8 mw/cm^2 for a period of seven seconds.

The exposed pattern was developed using KTI 934 1:1 solution for 60 seconds and baked at 110 degrees for 10 minutes. Finally a hydroflouric acid etch in the ratio 40 mls of 10:1 HF to 160 mls of deionized water was used. The etching process was monitored using a depth profile meter (DEKTAK) as well as microscopic observation. From the flaking of the dielectric layers it was clear when the glass substrate had been reached. An initial profile (before any processing) was also run in order to estimate the height of the high reflective coating layer. This initial height varied depending on the characteristics (primarily the wavelength) of the coating, and ranged from 2.5 to 5.5 microns for different mirrors. When the etch was complete the photoresist was removed by soaking in acetone and then rinsing thoroughly in methanol. Finally a nitrogen gun was used to dry the sample.

The above technique was adequate for the fabrication of microdots in the 400 micron to 50 micron diameter range. Though the procedure was simple and efficient, many improvements can be made. While it was used due to the highly resistant nature of standard dielectric coatings, HF is a dangerous and strong etchant and it would be desirable to avoid its use. Further, process reproducibility and controllability, as well as the smoothness of the pattern are not very good with wet etching processes in general. Reactive ion etching would certainly result in a cleaner definition of dots. It would also allow smaller dots to be fabricated; however, some experimentation would be required to identify appropriate gaseous etchants for the process. The most optimal process would perhaps be to have the high reflective coating *deposited* in a pattern onto the mirror. This avenue was not pursued in this work since a deposition facility was not available for this work.

The theory of the microdot mirror modelocker was developed by Huang et. al. in conjunction with the description of self-focussing using nonlinear scaling of the q parameter which has been described in detail in the previous chapter. Using this formalism, the linear and nonlinear characteristics on a single pass through the microdot mirror were calculated in order to understand its behaviour. In these calculations a

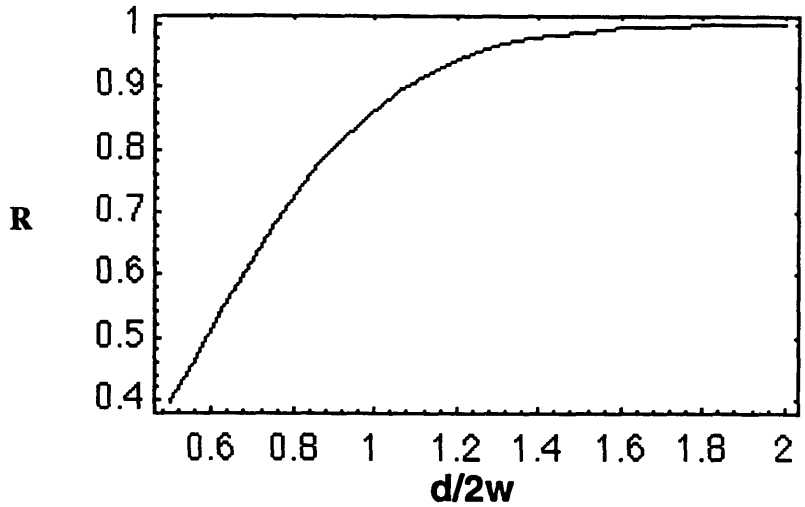

Figure 4-2: Linear reflectivity at low powers, R(0), of the microdot mirror plotted versus dot-diameter (d), normalized to the beam diameter (2w). The linear waist size is assumed to be 50 μm.

typical linear spot size of 50 μm is assumed at the high reflector face of the microdot mirror. The q parameter of the linear beam at the mirror entrance is then nonlinearly scaled, the beam is propagated through the mirror and scaled again at the high reflector in order to yield the nonlinear waist size. Aperturing functions are used to calculate the transmission (or reflection) of either the linear or nonlinear Gaussian beams through the high-reflecting dots.

Figure 4-2 and 4-3 plot the linear and nonlinear characteristics of the mirror as a function of dot diameter, d, normalized to the beam diameter, 2w. These curves are calculated for a linear spot size of 50 μm, a peak power of 100 kW and a microdot mirror thickness of 1.25 cm, assuming a linear beam waist of 50 μm. These values correspond approximately to the characteristics of the experimental demonstration to be described in the next section. The graphs are readily interpretable physically. The linear reflectivity, denoted by R(0), tends to 1 when the normalized dot diameter is large. It falls off exponentially for decreasing dot diameters, reflecting the aperturing of a Gaussian beam by a circular aperture. That is, for a dot of diameter d, the

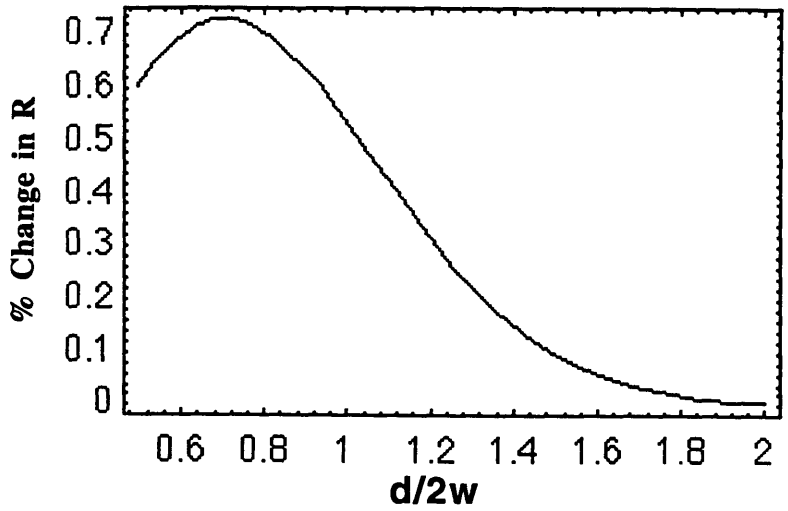

Figure 4-3: Microdot mirror nonlinear reflectivity (ie. change in reflectivity) at a power of 100 kW. The horizontal axis plots the dot-diameter, d, normalized to the beam diameter, 2w. The linear waist size is assumed to be 50 μm, the peak power is 100 kW, and the microdot mirror is 1.25 cm thick.

overlap with a Gaussian beam is given by,

$$R(0) = \frac{2}{\pi w^2}\int_0^{2\pi}\int_0^{d/2} e^{\frac{-2r^2}{w^2}} r dr d\phi \tag{4.1}$$

$$= 1 - e^{\frac{-d^2}{2w^2}} \tag{4.2}$$

The nonlinear reflectivity curve also has a characteristic shape. For very small or very large values of the normalized dot diameter the nonlinear reflectivity is zero. This is because in these limits, *both* linear and nonlinear spots at the microdot are either completly reflected or completely transmitted. For the parameters used, the maximum nonlinearity occurs when the normalized dot diameter is about 0.62. The maximum nonlinearity achievable in practice, is restricted by the linear reflectivity. Typically in a Ti:Al_2O_3 laser, for example, the linear reflectivity of the end mirror must be at least 85% in order for it to lase with sufficient intracavity power.

As expected, the nonlinearity is a function of the thickness of the microdot mirror and it saturates past a certain thickness. To demonstrate this, the nonlinearity for a

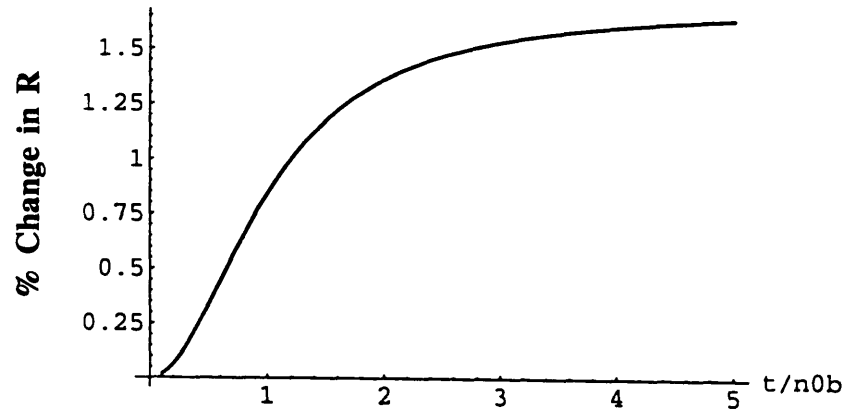

Figure 4-4: Microdot mirror nonlinear reflectivity (ie. change in reflectivity) at 100 kW plotted versus microdot mirror thickness, t, normalized to the n_0b, where n_0 is the linear refractive index and b the confocal parameter. The dot diameter is fixed at 85 μm and the linear waist size at 50 μm. Note the saturation of the nonlinearity for thicknesses in excess of $2n_0$b.

fixed dot diameter of 85 μm is plotted in Figure 4-4 versus the ratio of the microdot mirror thickness to the quantity $n_0 b$ where n_0 is the refractive index of the mirror substrate and b the confocal parameter. The saturation behavior for $l \gg 2n_0 b$ is clear.

4.3 Microdot mirror modelocked Ti:Al_2O_3 laser

The microdot mirror was first used to modelock a Ti:sapphire laser in the configuration shown in Figure 4-5. This work was done in 1991 in collaboration with Drs. Giuseppe Gabetta and Joe Jacobson. The gain medium was a 2.0 cm long Brewster-cut Ti:Al_2O_3 rod with an absorption coefficient of ~ 1 cm^{-1} at the pump wavelengths. The 2.1 m long laser cavity used a four-mirror folded design with the focusing mirrors having a 10 cm radius of curvature. The laser was pumped by all lines of a cw argon laser focussed into the microdot mirror by a 10.0 cm focal-length lens. Wavelength tuning and bandwidth control were provided by a single plate birefringent filter. In-

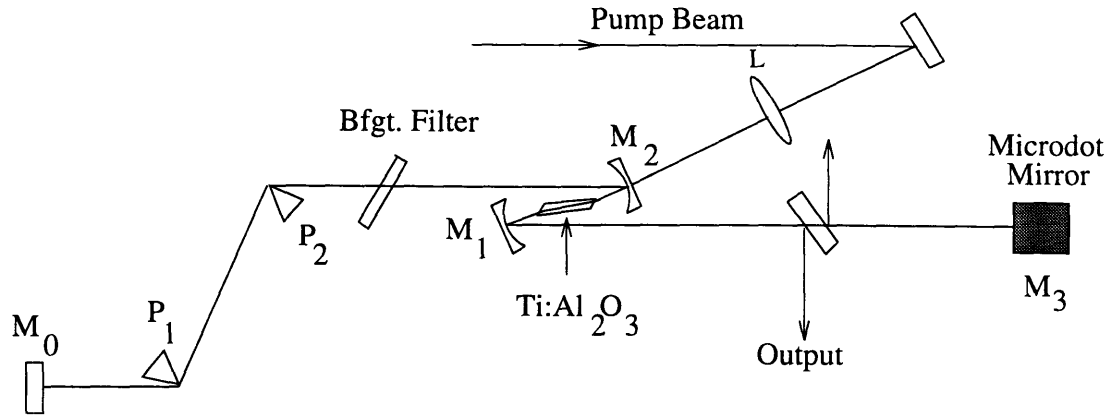

Figure 4-5: Schematic diagram of the microdot mirror modelocked Ti:Al_2O_3 laser. Mirrors M2 and M3 are curved while mirror M1 and the microdot mirror function as end mirrors. The output is taken from beam splitter BS. A single-plate birefringent filter is used for wavelength tuning. P1 and P2 are intracavity prisms for GVD compensation.

tracavity group-velocity dispersion compensation was achieved using a pair of SF10 Brewster-angled prisms separated by a distance of 80 cm. The maximum negative dispersion achievable with this pair of prisms was -12000 fs^2. The beam splitter functioned as an output coupler providing a total coupling of 5 % in two beams. The laser operated with a cw slope efficiency of 12 % and a pump threshold of 4.0 W. About 800 mW of output power was obtained at 10 W of pump power.

The microdot mirror was mounted on an xyz translator so that the mirror could be aligned to lase on any dot by transverse translation. The cavity was first aligned and optimized for CW operation on the uniform high-reflecting half of the mirror. The laser was then operated on progressively smaller dots until modelocking was achieved.

For the cavity configuration and operating parameters described above, mode locking was achieved using dots in the range of 77 to 85 μm. The laser was pumped at 10 W of power and the output power of 410 mW corresponded to an intracavity power of about 8 W. The intracavity prisms were adjusted to minimize the output pulse duration. The measured pulse duration was 190 fs (assuming a $sech^2$ pulse shape),

corresponding to 1.25 times the bandwidth limit. The modelocking was not self-starting but it could be initiated by inducing a sufficiently short intensity fluctuation in the laser, for instance by tapping an end mirror. Once modelocking is initiated the laser operated stably for an indefinite period of time.

4.4 Microdot mirror modelocked Nd:YLF laser

Modelocking techniques for lamp-pumped laser geometries are of interest in order to obtain higher power ultrashort pulses. Lamp pumped, actively modelocked Nd:YAG and Nd:YLF lasers are common commercial products. Acousto-optically modelocked Nd:YLF systems produce pulses only in the 50 ps regime which is quite far from the bandwidth limit of the gain medium ($\sim$ 1 ps) . However, passive modelocking techniques do not seem to have found widespread use in lamp pumped systems. Additive pulse modelocking (APM) has been applied to a lamp-pumped Nd:YLF system to generate 3.7 ps pulses with up to 7 W of average power [62]. Prior to this thesis KLM had only been used in laser-pumped, solid state systems. Due to the uniform pumping of the gain in lamp pumped systems, the possibility of exploiting mode changes in the gain for KLM, using the pump beam soft aperture, is excluded. Consequently KLM requires the addition of both a nonlinear medium at an intracavity focus as well as an appropriately positioned intracavity aperture. Regardless of the location of the nonlinearity, positioning of the intracavity aperture in KLM lasers is highly dependent on laser cavity design, alignment and pump-geometry and it requires careful modeling of the cavity. Due to all these complexities, active modelocking has continued to be the predominant approach for short pulse generation in lamp-pumped lasers.

Since it is quite independent of laser pump geometry, microdot mirror modelocking is a strong candidate for the passive modelocking of lamp-pumped solid-state lasers. It also has the advantage of modularity in the sense that the positioning of the

aperture is automatic and the entire device can be placed at the end of a wide variety of resonators to yield the desired saturable absorber effect. Finally, the broadband, non-resonant nature and sturdy nature of the device makes it quite flexible. For these reasons it was decided in this thesis to extend the technique of microdot mirror modelocking to an arc-lamp pumped Nd:YLF laser with the potential for high-power operation. This work was performed with initial assistance from Dr. Joe Izatt and in close collaboration with Dr. Artur Gouveia-Neto from the Department of Physics, Universidade Federal de Alagoas, Maceio, Brazil.

Initial experiments on the system indicated that stable short pulse generation did not result from the incorporation of a microdot mirror modelocking alone. Theoretical predictions [34] indicated that a dispersion compensation mechanism may be required for the production of stable, chirp-free pulses. Dispersion compensation would serve to cancel the substantial positive dispersion arising from the laser rod, as well as to provide operation in the soliton regime. Different methods of dispersion compensation for the system were evaluated. The relativly large magnitude of positive dispersion to be compensated, as well as practical reasons pertaining to a convenient cavity layout lead to the choice of a Gires-Tournois interferometer (GTI) as the preferred compensation mechanism. In the following discussion the operation and design of the GTI are first discussed, before presentation of the experimental results and observations from the system.

4.4.1 Dispersion compensation and the Gires Tournois Interferometer

The positive dispersion in the Nd:YLF rod was estimated using a Sellmeir [4] equation for the refractive index of the Nd:YLF medium. This equation is of the form

$$n^2(\lambda) = 1.38757 + .70757\frac{\lambda^2}{\lambda^2 - .00931} + .18849\frac{\lambda^2}{\lambda^2 - 50.99741} \qquad (4.3)$$

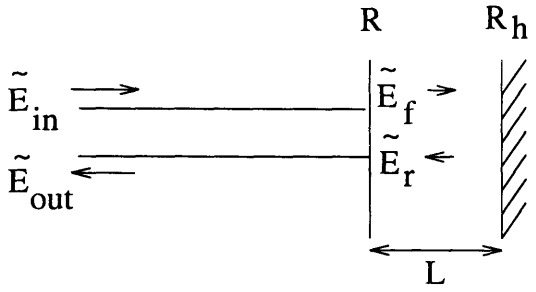

Figure 4-6: Schematic of a Gires Tournois Interferometer. R is the reflectivity of the partially reflective front face, R_H is the reflectivity of the highly reflective rear face and L is the spacing between the two layers.

From Chapter 2 we have that the total dispersion accumulated in passing through an optical system is given by

$$\frac{d^2\phi}{d\omega^2} = \frac{\lambda^3}{2\pi c^2}\frac{d^2P}{d\lambda^2}. \tag{4.4}$$

Since for a rod of length L, the optical path length, P(λ), , is simply

$$P(\lambda) = n(\lambda)L \tag{4.5}$$

we get that

$$\frac{d^2\phi}{d\omega^2} = \frac{\lambda^3}{2\pi c^2}L\frac{d^2n}{d\lambda^2}. \tag{4.6}$$

Using 4.3 and the experimental rod length of L = 10.4cm, it was estimated that the total positive material dispersion arising from propagation in the rod is + 1820 fs^2.

A Gires Tournois interferometer (GTI) consists of two mirrors aligned parallel to each other, with an air space (or other spacer layer) in between them. A schematic of a generic GTI is shown in Figure 4-6. R is the reflectivity of the partially reflective front face, R_H is the reflectivity of the highly reflective rear face and L is the spacing between the two layers. $\tilde{E}_{in}$ is the incoming field, $\tilde{E}_{out}$ the outgoing field, and $\tilde{E}_f$ and $\tilde{E}_r$ the fields in the two directions as indicated within the GTI. The complex reflectivity of the GTI has a frequency dependent phase and consequently when a short

pulse (composed of several frequencies) interacts with a GTI the reflected spectrum exhibits a frequency dependent phase shift. As described in Chapter 2, this introduces the possibility of group velocity and higher order dispersion of the pulse spectrum.

In order to analyze this problem we need to to derive an expression for the frequency dependence of the complex reflectivity, $\Gamma = |\Gamma| e^{\psi(\omega)}$ of a GTI. Γ is defined as

$$\Gamma = \frac{\tilde{E}_{in}}{\tilde{E}_{out}} \tag{4.7}$$

Consider the input plane wave,

$$\tilde{E_{in}} = E_0 e^{j(\omega t - kz)} \tag{4.8}$$

Recalling that the scattering matrix for a partially reflective layer [36] is

$$\begin{bmatrix} -\sqrt{R} & j\sqrt{1-R} \\ j\sqrt{1-R} & -\sqrt{R} \end{bmatrix} \tag{4.9}$$

and assuming that for the highy reflective rear surface $R_H = -e^{j\phi}$, we have the following set of equations:

$$E_f = j\sqrt{1-R}E_{in} + \sqrt{R}e^{j(\phi-\omega t_0)}E_f \tag{4.10}$$

$$E_r = -E_f e^{j(\phi-\omega t_0)} \tag{4.11}$$

$$E_{out} = -\sqrt{R}E_{in} + j\sqrt{1-R}E_r. \tag{4.12}$$

where $t_0 = 2Ln(\omega)/c$ is the round trip time within in the GTI. Eliminating E_r and E_f from the above equations we get that the complex reflectivity is

$$\Gamma = \frac{E_{out}}{E_{in}} \tag{4.13}$$

$$= \frac{-\sqrt{R} + e^{j(\phi-\omega t_0)}}{1 - \sqrt{R}e^{j(\phi-\omega t_0)}} \tag{4.14}$$

Taking the magnitude and phase of the above expression we have that

$$|\Gamma| = 1 \tag{4.15}$$

and the frequency dependent phase $\psi(\omega)$, of $\Gamma(\omega)$ is

$$\psi(\omega) = tan^{-1}\left[\frac{(1-R)sin(\phi-\omega t_0)}{-2\sqrt{R}+(1+R)cos(\phi-\omega t_0)}\right] \tag{4.16}$$

From these expressions it is clear that while the magnitude of the reflectivity remains constant independent of frequency, its phase $\psi(\omega)$ has a complex frequency dependence which is periodic in ω with a period defined by the round trip time within the GTI. $\frac{d^2\psi}{d\omega^2}$ which describes the GVD in the structure is also finite and periodic. The maximum available dispersion from the GTI increases as the square of the mirror spacing, L, and the period of the phase function, i.e. the free-spectral-range (FSR), is inversely proportional to the mirror spacing. The optimal design for the GTI must ensure that sufficient second-order dispersion is attainable and that the FSR is broad compared to the pulse spectrum so that GVD is relatively constant over the pulse bandwidth.

The GTI designed and used in the microdot mirror modelocked lamp-pumped Nd:YLF system was fabricated by collaborators at Coherent Inc., CA. It was a variable air-space structure with a nominal spacing of 350 μm, an uncoated front surface of reflectivity 4 % and a 99.9 % reflective back surface. Using these parameters and Equation 4.16 the GVD of the device is plotted in units of fs^2 as a function of wavelength in Figure 4-7 . The maximum dispersion is approximately + or $-$ 2.5×10^6 fs^2 and the FSR is approximately 1 nm.The mirror spacing, and thus the dispersion, can be varied using a piezoelectric transducer (PZT) to change the separation between the two mirrors. Varying the GTI separation by half a wavelength, i.e. $\lambda/2$, sweeps over an entire period in the dispersion function of the GTI.

Finally, note that if a partial rather than total reflector is used as the GTI rear

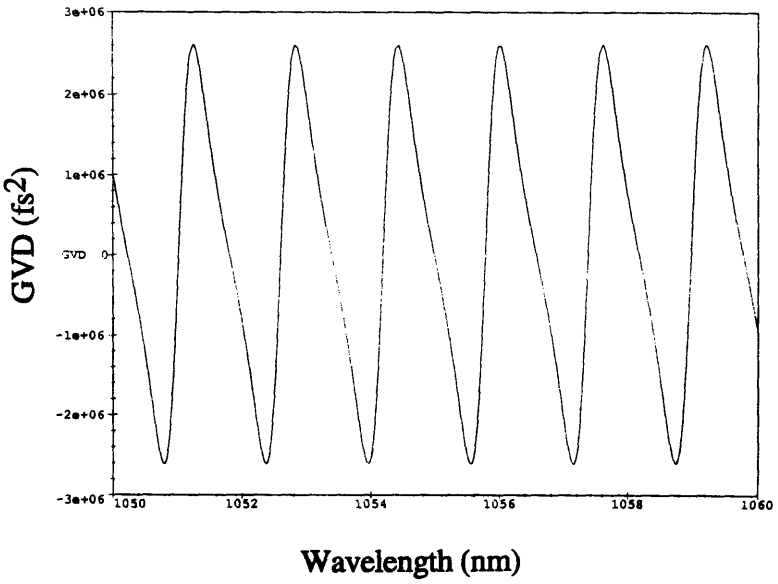

Figure 4-7: GVD in fs^2 plotted as a function of wavelength for a GTI with a nominal gap spacing of 350 microns, a front mirror reflectivity of 4% and a 100 % rear mirror reflectivity

mirror, the characteristics of the complex reflectivity are slightly modified and we have:

$$|\Gamma| = \frac{R + R_H - 2\sqrt{RR_H}cos(\phi - \omega t_0)}{1 + RR_H - 2\sqrt{RR_H}cos(\phi - \omega t_0)} \tag{4.17}$$

and

$$\psi(\omega) = tan^{-1}\left[\frac{\sqrt{R_H}(1-R)sin(\phi - \omega t_0)}{-\sqrt{R_H}\sqrt{R} - \sqrt{R} + \sqrt{R_H}(1+R)cos(\phi - \omega t_0)}\right] \tag{4.18}$$

4.4.2 Experimental results

The configuration for the microdot mirror modelocked lamp-pumped Nd:YLF system is shown in Figure 4-8. The system is based on a Quantronix 4217 lamp-pumped Nd:YLF laser, modified to incorporate the microdot mirror modelocker and the GTI. The gain medium is a 10.4 cm long by 4 mm diameter, arc-lamp pumped Nd:YLF rod. The above-described GTI is placed at one end of the cavity and the microdot mirror modelocker at the other. The cavity length was approximately 176

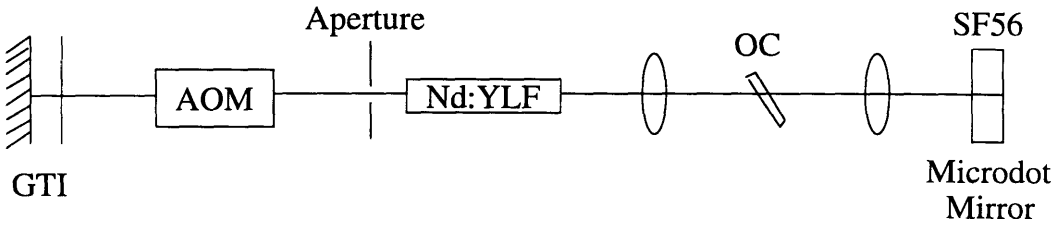

Figure 4-8: Schematic of lamp-pumped Nd:YLF laser cavity with a microdot mirror and a GTI.

cm. An acousto-optic modulator (AOM) was placed near the GTI end of the laser in order to actively modelock the laser and start the passive modelocking process. An aperture was placed between the AOM and the laser rod in order to discriminate against higher order spatial modes. A 45 cm spherical lens was placed close to the gain rod on the microdot mirror side of the cavity. Following predictions from cavity simulations to be described shortly, this lens was tilted off axis by approximately 16 degrees in order to compensate for astigmatism originating in the Nd:YLF rod. A 3.1 cm focal length lens was used to focus the laser mode into the microdot mirror. The output coupler is a 0.375 inch thick substrate that is anti-reflection coated on one side and coated on the other to provide a total output of about 2.3% in two beams.

The microdot mirror was composed of a 0.5 inch thick SF56 glass substrate. SF56 was chosen because its non-linear index ($n_2 = 9.082 \times 10^{-13}$ esu) is approximately 9 times that of BK7 glass. The substrate is anti-reflection (AR) coated on one side and high-reflection (HR) coated on the other side. The microdots in each row range in diameter from 200 microns to 50 microns, with the dots decreasing in area by 3% per column.

The laser was initially aligned for optimal active-modelocked performance lasing on the uniform high reflectivity portion of the microdot mirror. Pulse durations of 100 ps were achieved using active modelocking. The microdot mirror was then

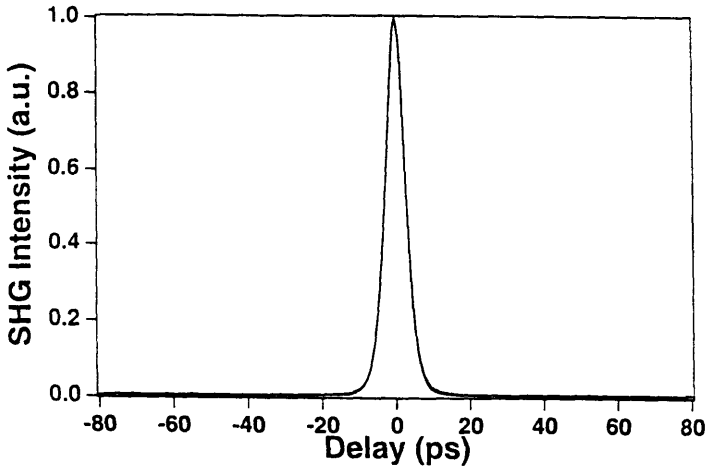

Figure 4-9: Typical autocorrelation from microdot mirror modelocked Nd:YLF system. The pulsewidth is 2.3 ps assuming a sech^2 shape

translated, transverse to the beam, so that lasing occured on successively smaller high reflecting dots. The GTI spacing was ramped over an entire FSR at each dot while the pulse-duration was monitored using background-free autocorrelation. When the saturable-absorber action introduced by the microdot mirror and the dispersion compensation from the GTI were sufficient, a dramatic reduction in pulse duration occurred. Pulse shortening was observed on dots with diameters ranging from 132 microns to 121 microns.

Figure 4-9 shows the autocorrelation of a typical pulse. The pulse duration is 2.25 ps assuming a sech^2 pulse shape. The spectrum of the pulse shown in Figure 4-10 fits reasonably with a sech^2 shape and has a FWHM of 0.53 nm corresponding to 1.20 times transform limit. The laser is not self-starting and microdot mirror modelocked was initiated using an AOM which provides a loss modulation of $\sim$ 5%. Similar approaches have been used to initiate KLM in Ti:Al_2O_3 lasers. Once the microdot mirror modelocking had been started, the RF power to the modelocker could be turned off and the passive modelocking process continued unperturbed for over one hour. The total output power in two output beams was about 800 mW at 82 MHz

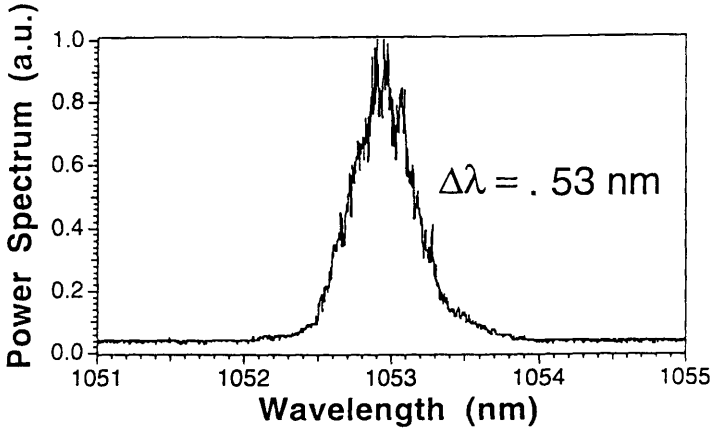

Figure 4-10: Spectrum of pulses from the microdot mirror modelocked Nd:YLF system. The FWHM is .53 nm

using a pump level of 36 A, corresponding to an arc-lamp power of 4.7 kW.

The microdot mirrror modelocked Nd:YLF cavity is quite complex due to strong astigmatic and thermal effects arising from the rod. Consequently the earlier code developed in Chapter 3 for the analysis of simple cavities, is not sufficient to model this cavity. A sophisticated iterative program developed by our collaborators at Coherent Inc, was used to calculate linear and nonlinear resonator modes in this cavity. This approach has been discussed already in Chapter 3 and was first proposed by Salin et. al [93]. It begins by solving the linear resonator mode using standard ABCD matrix techniques and using this as a first input for calculating the effects of self-focusing. Nonlinear self-focusing is accounted for by slicing up the nonlinear medium, in this case the microdot mirror, and using a parabolic approximation for the nonlinear index within each slice. Simulations were run in both XZ and YZ planes to account for the astigmatism of the rod. In addition the thermal lensing in the rod was also modelled.

The calculated linear transverse-mode radius is about 900 μm in the laser rod and about 40 μm at the microdot mirror. Figure 4-11 displays the simulated differential change in laser mode size at the highly reflecting microdot as a function of intracavity

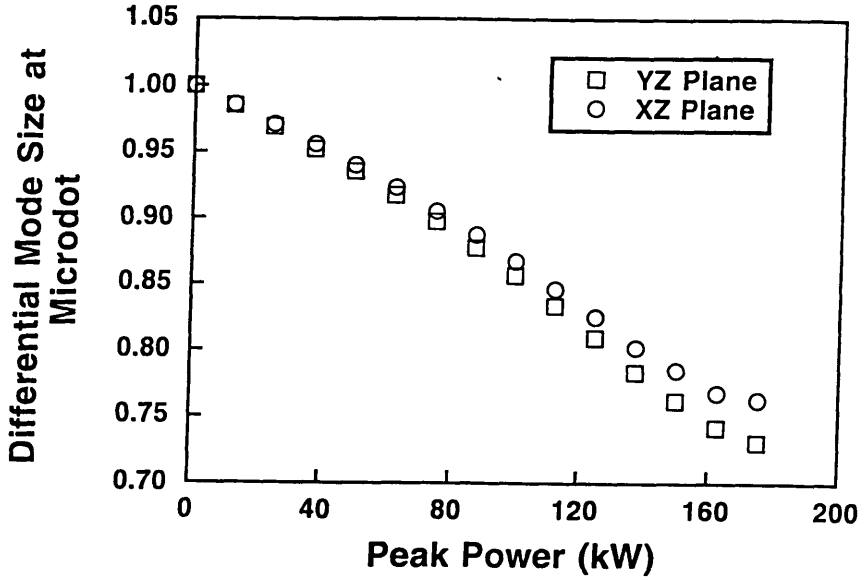

Figure 4-11: Differential change in mode size in microns at the rear surface of the microdot mirrror, plotted as a function of peak power. The estimated intracavity peak power was approximately 90 kW.

peak power. The estimated peak power in the laser was about 90 kW, which corresponds to a high-intensity mode area decrease of about 24 %. At this power, the saturable-absorber action (or change in reflectivity per unit change in peak power) is estimated to be about 0.28 % / kW. Mode-size changes also occured at the additional transverse aperture placed in the cavity for spatial-mode control. However, since the modelocking process was observed to be insensitive to the longitudinal position of this aperture it is not believed to have played an important role in providing KLM saturable absorber action.

In the case of the microdot mirror modelocking of the Nd:YLF system, the simulation of the self-consistent cavity linear and nonlinear modes, provides the opportunity for a comparison with the nonlinearity predicted on a single-pass calculation through the microdot mirror. This technique was discussed earlier in this chapter (see Figure 4-3 and used to design the microdot mirrors used in the above experiments. Using the linear spot size at the microdot mirror as predicted by the self-consistent cavity mode solution, the single pass change in beam size due to self-focusing in the mi-

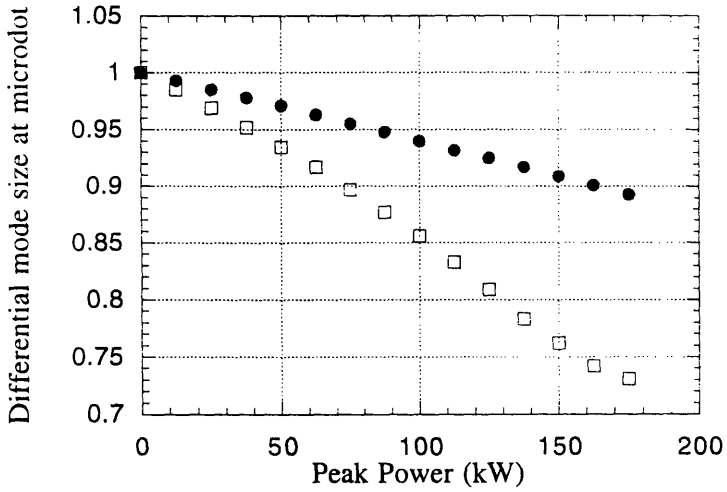

Figure 4-12: Comparison of single-pass and self-consistent approaches for calculating the effects of self-focusing. Differential change in mode size in microns, in the XZ plane, at the rear surface of the microdot mirrror, plotted as a function of peak power. The dots correspond to a single-pass calculation and the squares to the self-consistent cavity calculation.

crodot mirror was calcualated. Figure 4-12 plots the differential change in mode size predicted by this single-pass calculation as well as that predicted by the entire cavity simulation (ie Figure 4-11). The results from the two calculations are clearly very different. It is very important to note this difference and to keep it in mind when designing future experiments based on the microdot mirror modelocker. As far as possible the entire cavity linear and nonlinear modes should be simulated in order to predict nonlinear cavity behavior. Contrary to preliminary expectations the microdot mirror is not completely modular in terms of the nonlinear mode changes that it induces and therefore cannot as such be treated independently. This observation is confirmed further in Chapter 5 where the discrepancy between single-pass and self-consistent approaches is discussed again in the context of the compact KLM laser cavity configuration.

4.5 Conclusion

The above experiments seek to demonstrate that microdot mirror modelocking is an important alternative for the modelocking of solid-state lasers. The technique inherently possesses several advantageous features, in particular its modularity, non-resonant nature, compactness and relative independence from pumping geometry. However the most important feature of this technique is perhaps its versatility. The two dissimilar systems that have been modelocked using this technique bear testimony to this fact. To conclude this chapter a brief look at recent developments and a comparison of microdot mirror modelocking to Kerr Lens Modelocking will serve to clarify the future potential of the microdot mirror modelocking technique and to place the subject in perspective.

The above-described microdot mirror modelocked femtosecond Ti:Al_2O_3 system is a laser pumped system using prism pairs for dispersion compensation. While microdot mirror modelocking was demonstrated almost simultaneously with KLM (using a hard intracavity aperture or the soft pump beam aperture), in subsequent years KLM has clearly become the preferred method for modelocking of Ti:Al_2O_3 and other solid-state media capable of femtosecond pulse generation. In comparison with the microdot mirror modelocking technique, KLM (especially with the soft pump-beam aperture) has some distinct advantages. KLM, especially using the pump-beam aperture, is remarkably simple and uses a minimal number of intracavity components. However, it may be noted that the initial search for the modelocked operating point is more controllable with microdot mirror modelocking than with KLM using a soft aperture. The need to fabricate the microdot mirror, simple though it is, may also have served as a deterrant to the spread of microdot mirror modelocking. The most decisive advantage of KLM over microdot mirror modelocking has been the inherently smaller amount of higher order intracavity dispersion that is present in a KLM design. As has been described earlier, recent advances in the production of sub 50 fs pulses from Ti:Al_2O_3 have relied critically on the minimization of intracavity third and higher

order dispersion. In this context microdot mirror modelocking, is at a significant disadvantage due to the relatively large amount of glass it introduces into the laser in the form of the microdot mirror substrate. While it should be noted that with optimizations of laser design, pulse widths of 50 fs ought to be achievable from a microdot mirror modelocked Ti:Al_2O_3 system, pulses shorter than this will be hard to achieve with this technique. *Cancellation* of third order dispersion (using intracavity GTIs [46]), rather than its minimization could enable microdot mirror modelocking to compete with KLM in pulse width; however the relative complexity of such a system makes it somewhat unattractive.

In contrast to the Ti:Al_2O_3 medium, the Nd:YLF medium is characterized by a much narrower bandwidth and consequently produces much longer pulses. The other important difference lies in the lamp-pumped nature of the Nd:YLF system discussed above. In this case, KLM using nonlinearity in the gain medium is not an option because the intracavity mode is not tightly focussed in the gain medium. Consequently microdot mirror modelocking immediately becomes attractive. Further the long pulsed nature of the system reduces the importance of higher order dispersion introduced by the microdot mirror modelocking. However, as described above, it is essential to compensate for second order dispersion arising from the substantial length of the rod and the GTI has been shown to be a compact and effective way to achieve this. As mentioned earlier, active modelocking in lamp pumped Nd:YLF systems has been unable to achieve sub 50 ps pulse generation. Other passive modelocking techniques primarily the use of an AR-FPSA are feasible; however the level of intracavity power that the AR-FPSA can safely be exposed to remains unclear. We can conclude therefore that with the performance demonstrated in this thesis, microdot mirror modelocking can be considered a serious alternative for generating transform limited pulses from high-power, lamp-pumped systems.

Chapter 5

Compact, high repetition rate femtosecond Kerr lens modelocked lasers

5.1 Introduction

Overall system compactness and practicality are crucial factors which encourage both laboratory and commercial use of femtosecond lasers. While the emergence of the Ti:Al_2O_3 Kerr Lens Modelocked (KLM) laser consitutes a significant step towards a practical femtosecond source, these systems are still too cumbersome to be considered truly compact or practical. For this reason widespread research into the development of diode pumpable sources and the extension of existing modelocking technology to these systems is underway [61, 19, 68]. The elimination of expensive and space-consuming laser pumping will consitute a major step forward in popularizing femtosecond technology.

Concurrent with research into diode-pumping technologies, it is imperative to critically re-examine the design of the femtosecond oscillator itself. This is because it will take both a diode pump source *and a compact, simplified resonator design* to

create a truly practical femtosecond system. It is this fact that has motivated the design and implementation of a compact, high repetition rate femtosecond KLM laser geometry which forms the subject of this chapter.

The compact, femtosecond KLM laser developed in this chapter could find potential applications in instrumentation, imaging and high-speed communication technology. Further, the heretofore unachievable repetition rates we demonstrate will be useful for new kinds of fundamental experiments. An exemplary use is for experiments concerning the squeezing of light, whereby the random phase noise associated with light from a coherent source, for example a laser, is minimized through the use of self-phase modulation in a fiber. High repetition rates help in this process to avoid noise introduced by scattering off acoustic modes in the fiber. The cutoff frequency for this so-called Guided Acoustic Wave Brillouin Scattering (GAWBS) is about 1 GHz. Short-pulse sources at such repetition rates improve the achievable level of squeezing considerably, as recently demonstrated with a GHz Nd:YLF source [9].

The organization of this chapter is as follows. Section 5.2 reviews existing KLM laser geometries and identifies the need for dispersion compensation as a crucial factor in limiting system compactness. Section 5.3 discusses existing methods of compensating group velocity dispersion. Section 5.4 presents concepts required to analyze the use of prismatic elements for dispersion compensation. In Section 5.5 the implemented laser design is explained and analyzed. Section 5.6 presents the experimental results obtained utilizing this laser geometry. Section 5.7 discusses possible improvements to the technique. Section 5.8 suggests and discusses possible alternative dispersive resonator geometries. Section 5.9 concludes the chapter.

5.2 Overview of previous work

The laser geometry used in the first demonstration of self-modelocking in $Ti:Al_2O_3$ achieved in 1991 by Spence et. al. [104] is shown in Figure 5-1. It consisted of a

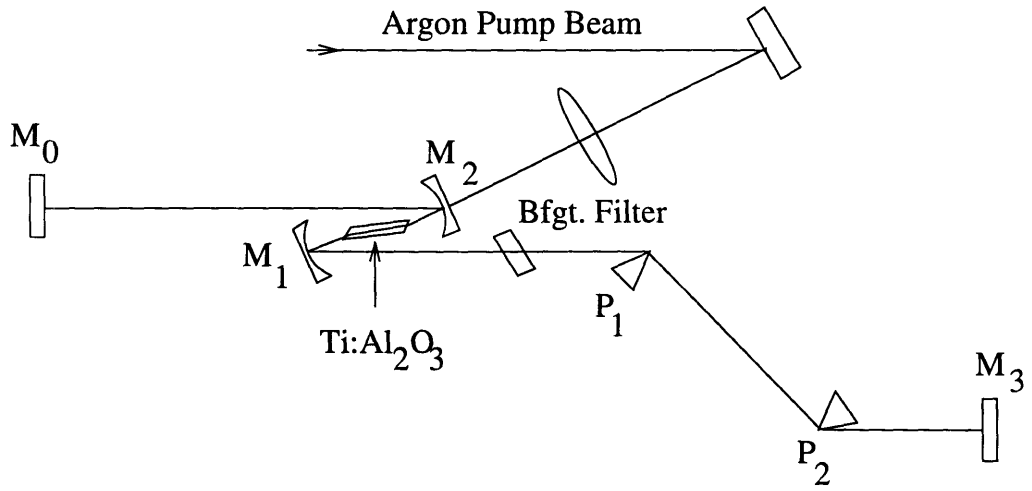

Figure 5-1: Schematic of the cavity configuration used in the self-modelocked laser demonstrated by Spence et. al. in [104]. This laser produced 60 fs pulses at a repetition rate of about 100 MHz.

Brewster angled gain medium, placed at the focus of a pair of curved mirrors. The pump beam is focussed into the laser crystal through one of the curved mirrors which is coated to be transmissive at the pump wavelengths. An SF14 prism pair separated by 35 cm is included in one arm of the laser for dispersion compensation and the laser produced 60 fs pulses at a repetition rate of approximately 100 MHz. The same cavity could also produce 2 ps pulses in the absence of dispersion compensation.

This so-called Z cavity appears to have become the model for the design of subsequent femtosecond KLM laser geometries. A close variant, the folded X cavity geometry shown in Figure 5-2 has also been popular. Even the most advanced, state-of-the-art, demonstrations of short pulse generation in $Ti : Al_2O_3$, producing pulses in the sub 10 fs regime [3, 5, 105], use geometries very similar to the Z cavity of Figure 5-1 or the folded X cavity of Figure 5-2. Ring geometries have also been proposed and demonstrated in a $Ti:Al_2O_3$ laser [113, 81]; however these ideas have not found widespread use.

A four prism sequence has been substituted for the two prism pair shown in

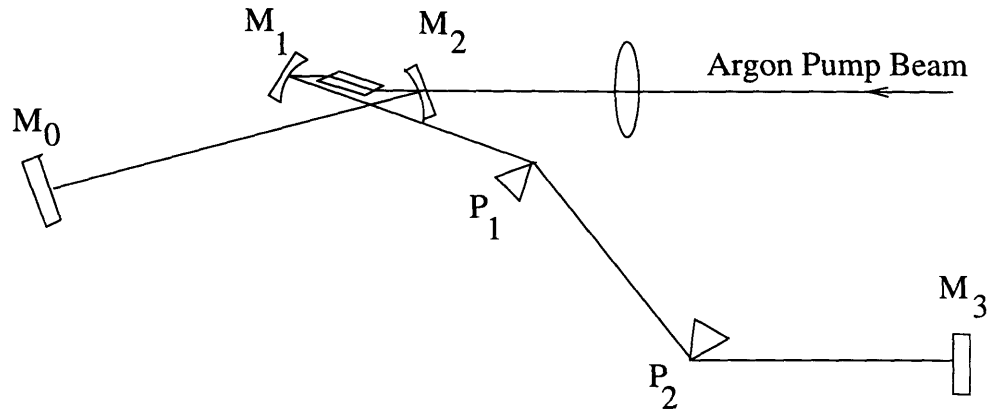

Figure 5-2: Popular X folded cavity layout for a Kerr-lens-modelocked Ti:Sapphire laser.

Figures 5-1 or 5-2 in some demonstrations [88]. This technique has the advantage that the laser beam emerges spatially undispersed at both ends of the laser cavity. Prism arrangements which provided greater dispersion for the same interprism spacing have also been conceived [85]. However, the goal here was not compactness but rather the convenient use of the low dispersive fused silica glass as prism material. Consequently, despite the use of a novel prism arrangement, the basic cavity geometry employed remained a folded X or Z cavity.

Demonstrations of KLM in other materials for example Cr:Forsterite [98], Cr:$LiCAlF_6$ [61], Cr:$LiSrAlF_6$ [19] and Cr^{4+}:YAG [99], have also employed very similar folded X or Z geometries, notwithstanding the different properties of these materials, in particular the fact that some of them can be diode-pumped.

Clearly then these geometries were believed to be optimal, or at least satisfactory, given the principal constraints on femtosecond KLM laser design that were assumed and are listed below.

1. The gain medium must be at an intracavity focus in order to ensure a tightly focussed infrared mode in the crystal for sufficient extraction of energy from

the pump. A two mirror converging fold has been historically popular from dye-lasers [117] and consequently became the natural choice.

2. An intracavity prism sequence separated typically by 30 to 50 cm must be included for dispersion compensation. To date, KLM in broad bandwidth lasers has achieved chirp-free and stable pulse generation exclusively in the negative dispersion regime [34] where the soliton-like effects arising from the interplay between self-phase-modulation and negative group-velocity-dispersion constitute the dominant pulse-shaping mechanism. The prism pair is a simple, low-loss and cost effective way of introducing negative dispersion. Its operation has also been understood in the context of femtosecond pulse generation from dye-lasers [17, 23]. These factors have lead to its widespread use in femtosecond KLM lasers

However, the prism pair clearly limits the laser geometry from several points of view. Simplicity of the cavity geometry, compactness, repetition rate and ease of alignment are all compromised as a result of the prisms. Not surprisingly, a closer examination of the literature reveals that longer pulsed systems such as Nd:YAG [63] and Nd:YLF [68] which did not include dispersion compensation mechanisms have been successfully Kerr Lens modelocked with significantly different laser geometries.

Among solid-state, short-pulsed lasers modelocked by techniques other than KLM one also finds evidence for a greater variety of geometries, including those that allow compact and high-repetition rate laser design. However once again the demonstrations are restricted to narrow-band media and the consequent lack of a dispersion compensation mechanism. Nd:YAG and Nd:YLF lasers have been modelocked at a repetition rates of 1 GHz and 500 MHz respectively, to produce sub 10 ps pulses using a high frequency acousto-optic-modelocking (AOM) techniques [118, 50]. FM modelocking has been employed to achieve 13 ps pulses at 5.4 GHz, in laser-pumped Nd:YLF system [97]. An Nd:YLF laser produced 10 ps pulses at 456 MHz when modelocked using an external coupled-cavity. It may be noted here that while the

repetition rate of these actively modelocked systems is eventually limited by the speed of the AOM involved, passive modelocking schemes, relying on the very fast Kerr nonlinearity, do not face a similar barrier.

In summary the evidence from past work pointed to the fact that a successful compact geometry for KLM would hinge on a compact and preferably simple way to introduce negative dispersion into a laser geometry.

5.3 Dispersion compensation

Several methods for the generation of negative group velocity dispersion have been suggested. Grating-pairs were suggested early on and have the advantage of being able to provide a relatively large amount of negative dispersion, but are not ideal for intracavity use due to their lossy nature [115]. Prism pairs were then introduced [23] and now constitute the most common dispersion compensation mechanism in femtosecond KLM lasers. The use of prism pairs for dispersion compensation is a legacy from the generation of dye lasers [22]. In addition to low insertion loss, they have the useful feature that the dispersion is easily tunable through the zero value. They have also been used in conjunction with gratings to externally compress dye laser pulses to generate the shortest light pulse which measured six femtoseconds [21].

Concurrent with these developments, the use of prisms for negative dispersion was analyzed theoretically [31, 21, 23], and simplified expressions to estimate the amount of negative dispersion from a given prism pair were developed. These details will be reviewed in the next section. Subsequently in recent years, when higher order dispersion from prisms has become an important parameter in minimizing the pulse durations attainable directly from solid-state lasers, more complicated ray-tracing analysis techniques for dispersion calculation have been developed [6].

Gires-Tournois Interfermeters (GTI) have also been used for dispersion compensation. The phase of light reflected a GTI varies periodically with frequency and for

appropriate parameters, the device can provide negative group velocity dispersion over a limited bandwidth. A GTI based laser [47] has been demonstrated to produce transform-limited pulses from 100 ps to 40 fs pulses at repetition rates of 82 MHz. GTIs have also been used to compensate for higher-order dispersion in Ti:Al_2O_3 lasers in order to produce very short pulses [46]. However, GTIs are expensive and delicate devices, which are not entirely suitable for use in very short pulse lasers. The amount of dispersion in a GTI varies as the square of the inter-mirror spacing; however the bandwidth varies as the inverse of this quantity. Consequently to design and build a GTI which provides sufficient dispersion compensation over a very wide bandwidth is not a trivial task.

Recently, special mirrors capable of providing negative dispersion have been designed and are the basis of an ultrashort pulse laser producing sub 10 fs pulses [109, 112]. The technology of chirped multilayer dielectric film deposition by which this is achieved is both interesting and elegant. Significantly, unlike most regular interferometric structures including GTIs, these mirrors exhibit a nearly constant GVD over as broad a bandwidth as 120 nm. However, the drawback is that to date only a small amount of dispersion can be achieved for each reflection off the mirrors. This necessitates a cavity design including several mirror bounces, thus increasing the complexity and size of the laser despite the elimination of the prism pair. Further, the negative dispersion introduced can be varied only in discrete quanta. While this is not a serious limitation, it limits the overall practicality and flexibility of the laser.

Other interesting methods for GVD compensation have been suggested. Notably an analysis of adjustable negative GVD from Graded Index (GRIN) lenses has been provided [114]. This is an interesting and compact way of providing GVD which is in fact integrable with waveguide or optical fiber technology [114]. However, GRIN lenses with appropriate parameters are hard to acquire which is the reason why experimental demonstrations are yet to come two years after publication of the theoretical analysis.

5.4 Dispersion compensation using prismatic elements

It is clear from the above overview that at the time of this work, a suitably compact, cheap and flexible dispersion compensation technique was not evident among pre-existing techniques. For the construction of a compact and high-repetition rate femtosecond source we therefore designed a novel dispersion-compensation technique that uses prismatic cavity end elements. Our technique of dispersion compensation builds on concepts contained in the earlier cited analysis [31, 23] of dispersion compensation arising from intracavity prisms. This section first provides relevant details of this background.

The introduction of negative dispersion into a ring laser cavity by a single prism was observed by Dietel et. al. in 1983 [17, 20], but not well understood at the time. In 1984, Gordon and Fork published a paper explaining how the single prism, double mirror ring resonator pictured in Figure 5-3 could provide negative dispersion [31]. This resonator is closely related to our high-repetition rate KLM scheme to be described shortly. Recall from Chapter 2 that group velocity dispersion in an optical system, arises from a frequency or wavelength dependent propagation constant and can in general be expressed as

$$\frac{d^2\phi}{d\omega^2} = \frac{\lambda^3}{2\pi c^2}\frac{d^2P(\lambda)}{d\lambda^2} \tag{5.1}$$

where $P(\lambda)$ is simply the wavelength-dependent path length through the system. In order to calculate the dispersion of the resonator in Figure 5-3 we need to derive an expression for $P(\lambda)$ at the central wavelength through this system.

Figure 5-4 shows lines representing two wavelengths propagating through the prism; AC through the apex and BD at the central wavelength. Implicit in this picture is the important assumption that the monochromatic spatial mode representing each wavelength capable of oscillating in the laser is defined with respect to a

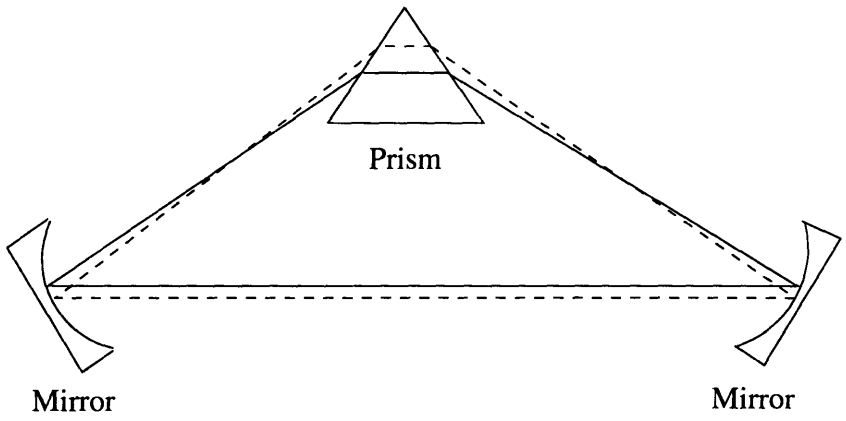

Figure 5-3: Cavity layout for single-prism ring resonator capable of exhibiting net negative intracavity dispersion. The two lines represent propagation axes corresponding to two different wavelengths.

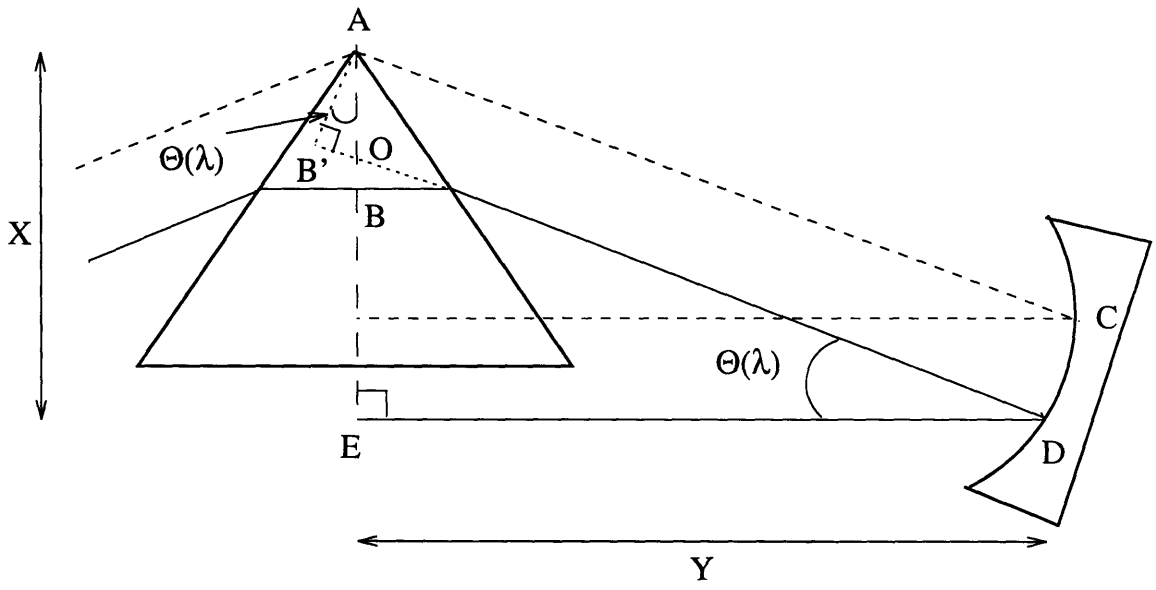

Figure 5-4: Analytic diagram for single-prism ring resonator.

distinct axis. This axis will be referred to hereafter as a *propagation axis.* The entire spatial mode corresponding to each wavelength and consequently to each propagation axis must be determined through the standard resonator mode analysis techniques overviewed in Chapter 3. However, the dispersive properties of the resonator can be estimated by simply studying the path of the wavelength dependent propagation axes through the resonator. Restriction of the analysis to propagation axes, permits the application of the laws of ray optics in order to determine the self-consistent intracavity paths of these axes. This is indeed the approach that has been used by Gordon and Fork in their analysis of this resonator [31]. However, they do not explicitly clarify these concepts which are in fact crucial to a proper understanding of how and why dispersion can be accomodated into resonators in unexpected and interesting ways, as in the resonator of Figure 5-3 and in the high-repetition rate KLM laser geometry of the next section.

Elegant theoretical formalisms for analyzing dispersive cavities have been developed by Martinez [71, 72] and improved on by Kostenbauder [58]. Martinez has observed that in the analysis of a cavity including one or more dispersive elements, the ABCD matrix formalism cannot adequately account for the frequency dependence of parameters such as gain, time delay, beam center and propagation angle. He has also noted that the Gordon and Fork ray tracing strategy just summarized, can be used to obtain the solution for particular cavity configurations, but does not provide a thorough understanding of the laser behavior as a function of different parameters. For this purpose it is essential to develop new theoretical tools; namely the E and F terms in an expanded ABCDEF matrix formalism. The E terms in these matrices account for relative displacement of wavelength dependent propagation axes and the F terms describe relative angles of propagation. Kostenbauder has carried these ideas further through the use of an elegant 4 X 4 matrix formalism that has the physically appealing feature of keeping optical system and light-beam dependent matrices entirely separate.

Returning to the resonator of Gordon and Fork and to Figure 5-3, we can now clearly identify two propagation axes representing two wavelengths, these axes having been propagated self-consistently through the cavity entirely subject to the laws of ray optics. The entire path length of the central wavelength (solid line) through the resonator is given by 2BDE in Figure 5-4. Since AB and CD are both possible wavefronts and AC and BD must be equal in optical path length. To calculate the length BD it is therefore sufficient to calculate the length $B'D$ which is equal by construction to the length AC. After some trigonometry one can prove that the

$$BD = B'D = AEsin(\theta) + EDcos(\theta) \tag{5.2}$$

and so

$$P = 2BDE = 2AEsin(\theta) + 2ED(1 + cos(\theta)) \tag{5.3}$$

Since the angle θ is a function of the prism index, n, which is in turn a function of λ, by application of the chain rule for derivatives we can write that

$$\frac{dP}{d\lambda} = \frac{dP}{d\theta}\frac{d\theta}{dn}\frac{dn}{d\lambda} \tag{5.4}$$

and similarly,

$$\frac{d^2P}{d\lambda^2} = [\frac{d^2n}{d\lambda^2}\frac{d\theta}{dn} + \frac{d^2\theta}{dn^2}(\frac{dn}{d\lambda})^2]\frac{dP}{d\theta} + (\frac{d\theta}{dn})^2(\frac{dn}{d\lambda})^2\frac{d^2P}{d\theta^2} \tag{5.5}$$

Since expressions for $n(\lambda)$ are usually available, to calculate dispersion it is sufficient to obtain expressions for $P(\theta)$ (Equation 5.3), $\theta(n)$ and their derivatives . Using Snell's law it is easily shown that

$$\theta(n) \;=\; sin^{-1}(nsin\alpha) - \alpha \tag{5.6}$$

$$\frac{d\theta}{dn} = [(sin\alpha)^{-2} - n^2]^{-1/2} \tag{5.7}$$

$$\frac{d^2\theta}{dn^2} = n(\frac{d\theta}{dn})^3 \tag{5.8}$$

where 2α is equal to the apex angle of the prism. These expressions can be further simplified at the central wavelength, λ_0 corresponding to the Brewster angle on the prism. The derivatives of $P(\theta)$ require further geometric analysis, the details of which are straightforward but not particularly pertinent here. The important issue to understand in the analysis outlined above is the general method by which the dispersion calculation is performed. The reader is therefore referred to the paper by Gordon and Fork [31] for further geometrical details on the derivation of $dP/d\theta$ and $d^2P/d\theta^2$ which lead to the final expression of round-trip dispersion in this resonator given by,

$$\frac{d^2\phi}{d\omega^2} = \frac{\lambda^3}{2\pi c^2}[\frac{d^2n}{d\lambda^2} + n(\frac{dn}{d\lambda^2})^2]2AB' + (\frac{dn}{d\lambda})^2 2(f - BD) \tag{5.9}$$

where f = R/2 is the identical focal length of the two resonator mirrors and the derivatives are evaluated at the central wavelength, λ_0. This equation can be easily understood in physical terms. The positive dispersion term is proportional to AB' which is a measure of the insertion of the prism into the beam. The negative dispersion introduced is proportional to the term (f - BD). This quantity is the optical path length from the prism bisector to the intersection point between propagation axes (on either side of the prism). The cavity configuration dictates that the intersection points for the self-consistent paths of different propagation axes always fall a focal length away from the mirrors. Propagation from the intersection point on one side of the prism over to that on the other side (reflecting off the mirrors in the process) does not introduce dispersion since by Fermat's principle all rays must travel equal optical path lengths while traversing this distance. Consequently, for mirrors of given focal length, the further away from the prism they are placed, the larger will be the

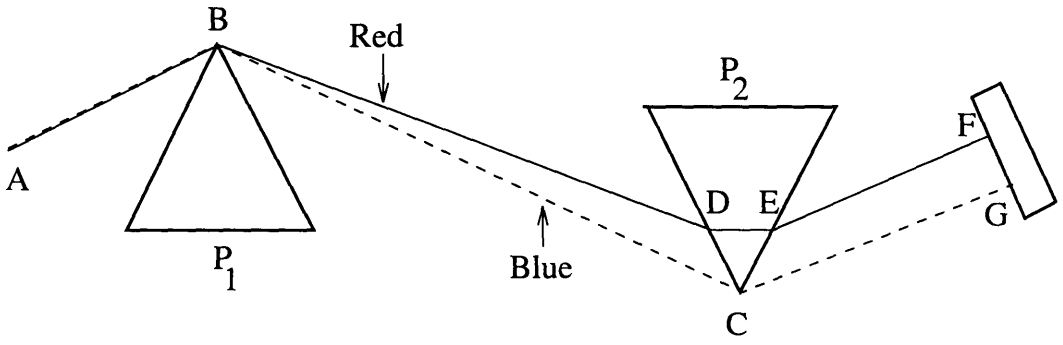

Figure 5-5: Negative dispersion from a pair of prisms

negative dispersion introduced.

A similar analysis has been used to analyze the case of a prism pair shown in Figure 5-5 [23]. It is enlightening to note that in *both* cases the origin of negative dispersion is the fact that light at longer wavelengths (red) travels through more intracavity material than light at shorter wavelengths (blue). However, the method by which this is ensured differs somewhat in each case. In the case of the prism pair the first prism can be thought as serving to angularly disperse the light. Referring to Figure 5-5, the fact that red light gets deviated less by P1, combined with the orientation of P2 ensures the propagation of red light through more material in P2. It is important to emphasize that the existence of GVD depends on the second derivative of path length with respect to wavelength, consequently a linear variation of path length with wavelength as produced in the air between the two prisms, does not produce GVD.

While the prism-pair can be considered as a modular element which can be introduced at one end of any resonator geometry to introduce negative dispersion, in the case of the single-prism ring resonator, the existence of dispersion and its magnitude are both closely tied to the cavity geometry. The path followed by propagation axes

is indeed now a function of *both* the dispersive properties of the prism *and* the specific details of cavity geometry. When the interaction of these two forces produces a spatial separation of self-consistent round trip paths of propagation axes, such that light at longer wavelengths traverses more intracavity material than light at shorter wavelengths, negative dispersion is introduced. The magnitude of this effect is entirely a function of the particular geometry under discussion. In the case discussed above, with AB = 1 mm and f= 60 cm, and using a quartz prism, a length of BD $\sim$ 1.1 m is required to adequately compensate for the positive dispersion from a typical 5 mm sapphire crystal. Thus lasers fashioned after this geometry are potentially quite large (repetition rate $\sim$ $150MHz$). Another significant problem is that of transforming the theoretical *resonator* of Figure 5-3 into a real *laser* which requires the incorporation of a gain medium into which the lasing mode must be focused, and an appropriate pumping mechanism. It is not evident how this can be simply and efficiently achieved without significant changes in the proposed resonator design of Gordon and Fork.

5.5 Compact dispersion-compensating laser: design and analysis

To achieve the goal of building a compact and dispersion compensated KLM laser, a related but different geometry pictured schematically in Figure 5-6 was designed in this thesis. This geometry is able to provide adequate negative dispersion, and can also be very conveniently implemented in the laboratory. It consists of a bare minimum of components, namely a flat-Brewster cut gain medium, a curved mirror and a prismatic output coupler. The prismatic output coupler is one half of a Brewster prism which is coated on one side with an appropriate reflective coating. It serves simultaneously to provide angular dispersion of the laser beam and to couple light out of the laser.

To Kerr lens modelock any laser one must incorporate both fast saturable absorber

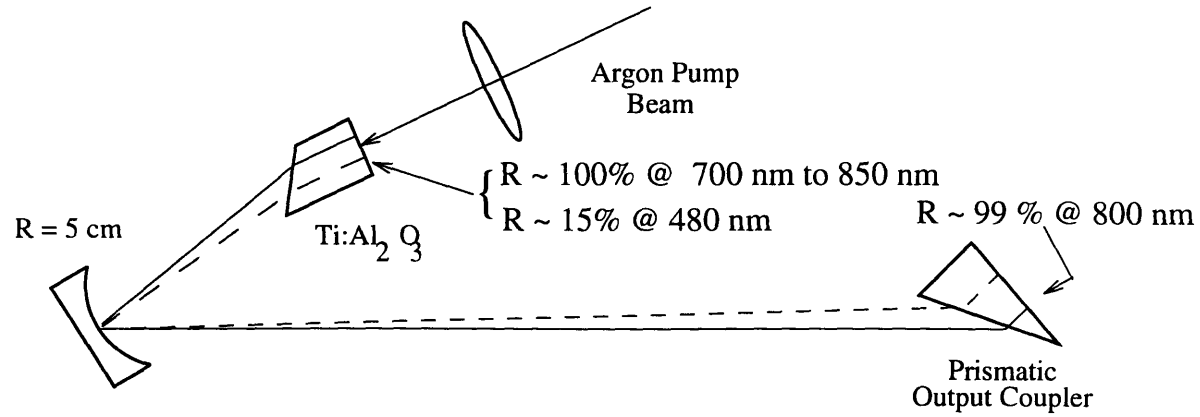

Figure 5-6: Simple, compact and dispersion compensating cavity layout. Solid and dashed lines represent the self-consistent round-trip intracavity paths corresponding to two distinct wavelengths. The cavity geometry enforces the spatial separation of these paths causing light at longer wavelengths to traverse more intracavity material. This is the origin of negative dispersion.

action and net negative intracavity dispersion into the laser design. Of course, the laser geometry must be capable of supporting broad band oscillation in the first place. As will be apparent from the ensuing analysis, the laser of Figure 5-6 is able to satisfy all of these conditions.

5.5.1 Saturable absorber action

The analysis of dispersion in the cavity proceeds, as before, by consideration of self-consistent intracavity paths of propagation axes. However, the entire spatial mode profile corresponding to each wavelength must be determined using the standard resonator mode analysis techniques described in Chapter 3. Such analysis identifies the intracavity location of beam waists and their relative sizes as well as the cavity operating points where fast saturable absorber action can be obtained.

The unfolded resonator of Figure 5-6 corresponds indeed to the simple lens cavity analyzed in Chapter 3, if one neglects the astigmatic effects introduced by the

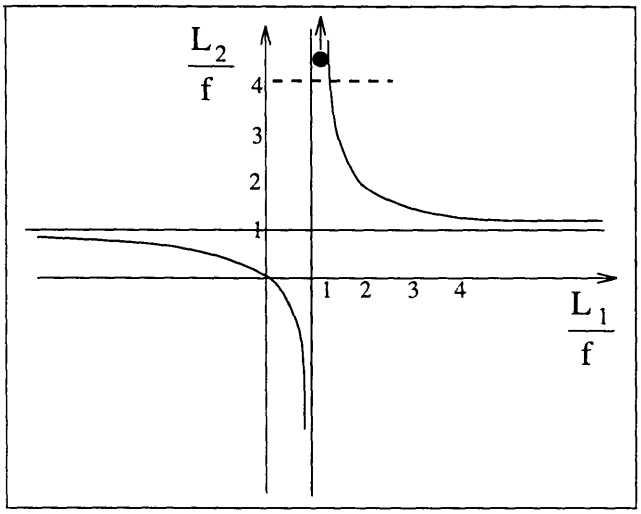

Figure 5-7: Approximate position in the cavity stability map of the operating point of the compact KLM laser. The dashed line corresponds to the type of cross-section along which the linear and nonlinear modesizes are plotted in the next three figures.

Brewster surfaces in the cavity. Using the code developed earlier to calculate linear and nonlinear cavity spatial modes we found that for our cavity configuration and operating point the spatial modes for all wavelengths are tightly focused in the gain medium and relatively collimated in the longer cavity arm. Due to self focussing in the gain medium, for certain cavity settings, i.e. at certain points in the linear geometric cavity stability map, higher intracavity intensities present a smaller mode size in the gain medium and therefore overlap better with the focussed pump beam therein. This provides the requisite intensity-dependent loss mechanism or fast-saturable absorber action necessary for KLM.

In particular, the operating point chosen for KLM operation of the compact source is shown in Figure 5-7 and corresponds to point 7 of the points analyzed in Table 3.2 of Chapter 3. As discussed earlier, this point is suitable for several reasons namely its small mode size in the gain medium($\sim$ 25 μm), its negative change in modesize in the crystal at high powers ($\sim$ -48 % at 0.5 $\times$ P_{crit}) , and its relatively large γ/δ ratio

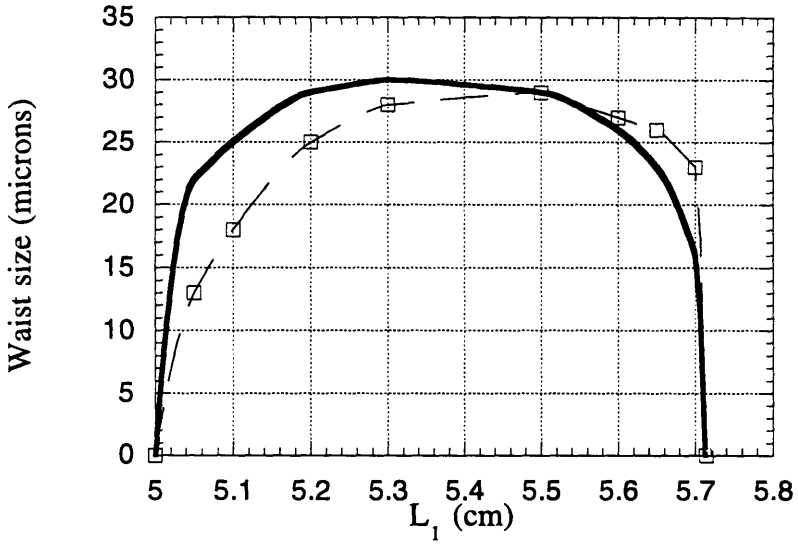

Figure 5-8: Linear (solid) and nonlinear (dashed) mode-sizes in μm for compact KLM laser, plotted as a function of one arm length, L_1, while the second arm length L_2 is held constant at 8f. Nonlinear modes are calculated at .5 * P_{crit}, the crystal length assumed is 0.3 cm and f = 5 cm.

($\sim$ -1.1 at 0.5 $\times$ P_{crit}).

As discussed in Chapter 3, it is important to note that small deviations in the point of operation on the linear-stability map, can result in *qualititatively* different effects of self-focusing. For example, on a closer examination one finds that not all points close to operating point 7 of Chapter 3 (shown in Figure 5-7) exhibit a negative change in modesize in the crystal, for higher intensities. We can quantify this by plotting the linear and nonlinear modesizes at the crystal high reflector (for a power of .5 $\times$ P_{crit}) as a function of one arm length, L_1, while maintaining a fixed second arm length, L_2, approximately equal to 8f. The focal length f used is 5 cm. The type of cross-section along which the mode is plotted is shown as a dashed line in Figure 5-7. Figure 5-8 plots the linear and nonlinear modesizes along this cross-section, as calculated by the iterative procedure for calculation of self-consistent non-linear cavity modes. The two stability boundaries in this diagram occur at L_1 = f = 5 cm and at $1/L_1 + 1/L_2 = 1/f$ ie. where $L_1 \sim 5.7$ cm. Since the nonlinear modesize in the crystal is smaller than the linear modesize only at points close to *one* of these boundaries, KLM action

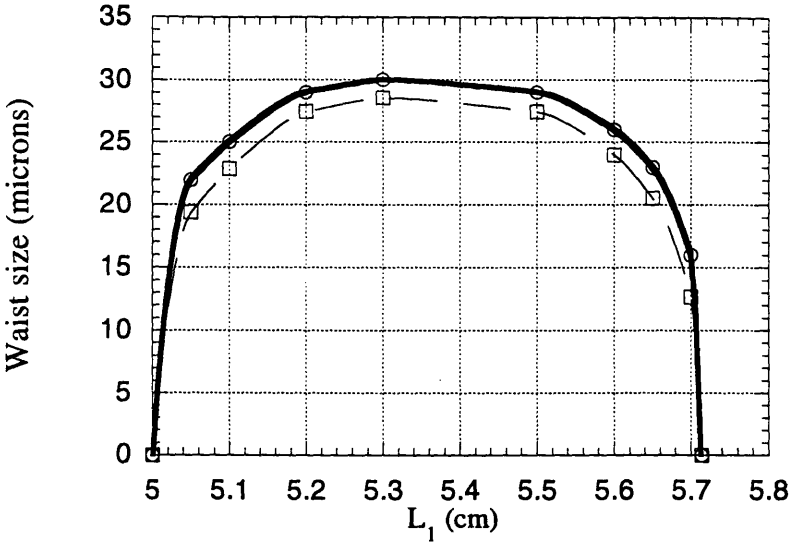

Figure 5-9: Single-pass calculation of linear (solid) and nonlinear (dashed) mode-sizes in μm for compact KLM laser, plotted as a function of one arm length, L_1, while the second arm length L_2 is held constant at 8f. Nonlinear modes are calculated at .5 * P_{crit}, the crystal length assumed is 0.3 cm and f = 5 cm.

using the pump beam aperture is possible only at points closer to this boundary. This fact was borne out experimentally, when modelocked operation could be achieved at points close to the L_1 = f boundary but not at the other one.

The above described assymetry in the nonlinear behavior at the two borders of stability is quite important. It is encouraging that the simple picture of self-focussing (discussed in Chapter 3) as a shortening of the arm containing the nonlinear medium does indeed predict this behavior. It is important to note, however, that the calculation of nonlinear self-focusing in a *single-pass* through the crystal does *not* yield the correct qualitative or quantitative result. Figure 5-9 shows the predicted single-pass change in waist size calculated using the transformation of the q-parameter, using the appropriate linear beam q-parameter (calculated by the self-consistent round-trip calculation) at the entrance of the crystal. Clearly this calculation predicts that the nonlinear waist will be smaller than the linear one throughout the stability region. This prediction is in disagreement with the simulated self-consistent round-trip solu-

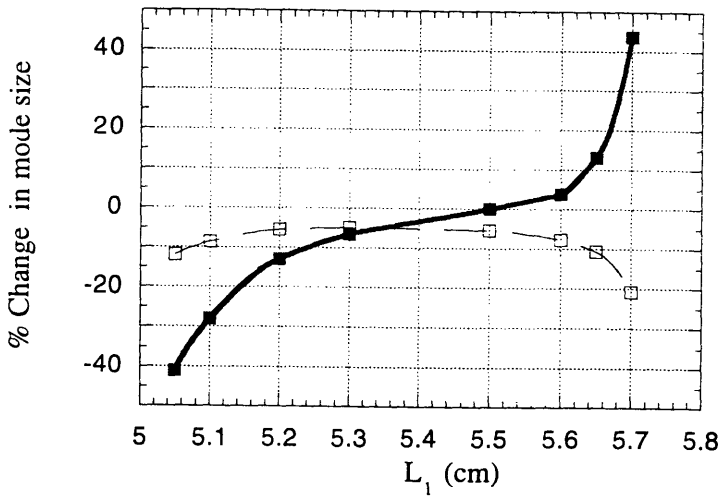

Figure 5-10: Change in mode size at crystal high reflector plotted as a function of one arm length, L_1 as calculated using a single-pass calculation (dashed line) and on a self-consistent round trip calculation (solid line). The second arm length L_2 is held constant at 8f. Nonlinear modes are calculated at .5 * P_{crit}, the crystal length assumed is 0.3 cm and f = 5 cm.

tion of Figure 5-8 as well as with the experimental findings to be described shortly. Figure 5-10 makes the discrepancy clear by comparing the predicted change in mode size at the crystal high reflector using the single-pass technique (Figure 5-9) and the self-consistent round-trip cavity simulation (Figure 5-8). Clearly the results are quite different not only in magnitude but also in *sign.* One must conclude that an estimate of the effects of self-focussing in a laser cavity cannot be accurately predicted using only a single pass calcualation through the nonlinear medium. The same observation was also made in the Chapter 4 in the context of Microdot mirror modelocking of the Nd:YLF laser.

5.5.2 Dispersion calculation

Turning to the dispersion calculation, the cavity exhibits net negative dispersion because the resonator setup and geometry ensure that propagation axes of different wavelengths follow *spatially displaced* self-consistent intracavity paths. The wave-

length dependence of angular deviation at the two Brewster interfaces is responsible for causing this relative displacement of propagation axes, as a consequence of which light at longer wavelengths traverses more material at both ends of the cavity, thus generating negative GVD.

To estimate the GVD introduced, using an analysis analogous to that of Gordon and Fork, we need to derive an expression for the wavelength dependent path length, $P(\lambda)$, of propagation axes through the cavity. The unfolded equivalent cavity of Figure 5-11 is used in this analysis. Note that the curved mirrror of radius R is replaced by a lens of focal length R/2. A self-consistent path for any wavelength through this laser must be perpendicular to the reflective laser end surfaces *and* be appropriately deviated at each Brewster interface. If the deviation of a given wavelength caused by both interfaces (gain and output coupler) is identical, each propagation axis (independent of wavelength) must travel undeviated through the intracavity lens in order to define a self-consistent intracavity path. This implies that propagation axes for all wavelengths will pass through, and indeed, intersect at the center of the lens. Mathematically, we can state that the assumption wherein the intersection point, O, falls on the lens center, L, is accurate in the limit when

$$\frac{dn/d\lambda}{dn'/d\lambda} = 1 \tag{5.10}$$

where $n(\lambda)$ is the refractive index of the gain medium and $n'(\lambda)$ is the refractive index of the prismatic output coupler. For example when we use Ti:Al_2O_3 as the gain medium and LAKL21 as the prismatic output coupler substrate, this ratio is 0.98 and consequently the above approximation is reasonable.

To proceed further in the calculation of $P(\lambda)$ the laser is divided into two parts on either side of the intracavity intersection point between propagation axes. For simplicity, let us first consider the limit described by Equation 5.10 where the intersection point, O, of propagation axes falls on the center of the lens, L, as shown in the unfolded equivalent cavity diagram of 5-11. Note that this point will henceforth be

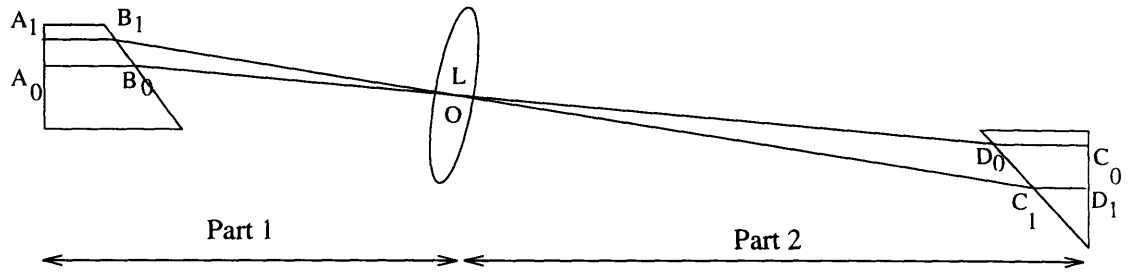

Figure 5-11: Equivalent unfolded cavity schematic for dispersion calculation in laser of Fig 5-6. The curved mirror is replaced by an equivalent lens. Materials with identical $dn/d\lambda$ are assumed for the gain medium and the prismatic output coupler, resulting in intersection of propagation axes at the lens center, C.

referred to exclusively as O. Note also that the assumption of Equation 5.10 is by no means essential to the KLM operation of the laser geometry of Figure 5-6; however it provides a simple starting point for the analysis which will be generalized later. Note finally that Figure 5-11 and the following analysis do not account for astigmatic effects.

$P(\lambda)$ can be decomposed into two parts as shown in Figure 5-11. The optical path lengths associated with these parts are $P_1(\lambda)$ and $P_2(\lambda)$ respectively. We can therefore write that the total optical path length P(λ) is given by,

$$P(\lambda) = P_1(\lambda) + P_2(\lambda) = ABO + CDO \tag{5.11}$$

where the points A, B, C, and D will clearly be wavelength dependent as shown in Figure 5-11 for two wavelengths. This wavelength dependence will not be explicitly indicated in subsequent equations.

As in the analysis of Gordon and Fork described earlier, referring to Figure 5-12, it can be seen from Fermat's principle that the optical path length ABO is equivalent to the distance RQO. In this figure the apex of the prism is denoted by Z. Therefore

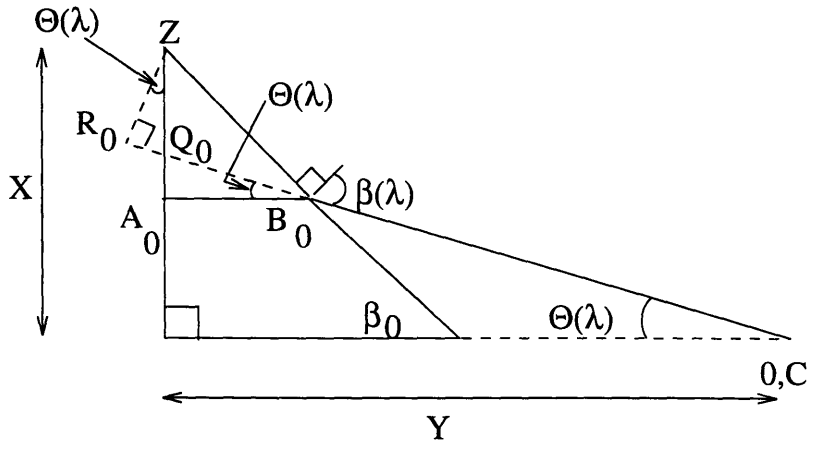

Figure 5-12: Detailed geometry for calculation of path length in one part of unfolded cavity of Figure 5-11.

$P_1(\lambda)$ can be calculated as follows.

$$P_1(\lambda) = RQO = RQ + QO \tag{5.12}$$

Since,

$$RQ = ZQ sin\theta(\lambda) \tag{5.13}$$

$$= (X - Y tan\theta(\lambda)) sin\theta(\lambda) \tag{5.14}$$

and

$$QO = \frac{Y}{cos\theta(\lambda)} \tag{5.15}$$

we have that

$$P_1(\lambda) = (X - Y tan\theta(\lambda)) sin\theta(\lambda) + \frac{Y}{cos\theta(\lambda)} \tag{5.16}$$

$$= X sin\theta(\lambda) + \frac{Y}{cos\theta(\lambda)}(1 - sin^2\theta(\lambda)) \tag{5.17}$$

$$= X sin\theta(\lambda) + Y cos\theta(\lambda) \tag{5.18}$$

We now have $P_1(\lambda)$ as a function of $\theta(\lambda)$. Applying the chain rule we get,

$$\frac{d^2P_1}{d\lambda^2} = \frac{d^2P_1}{d\theta^2}(\frac{d\theta}{d\lambda})^2 + \frac{dP_1}{d\theta}\frac{d^2\theta}{d\lambda^2} \tag{5.19}$$

We will evaluate the dispersion at a central wavelength $\lambda = \lambda_0$ for which the prism is cut where it can be proved that,

$$\frac{d\theta}{d\lambda} = \left.\frac{dn}{d\lambda}\right|_{\lambda_0} \tag{5.20}$$

and

$$\frac{d^2\theta}{d\lambda^2} = \left.\frac{d^2n}{d\lambda^2}\right|_{\lambda_0} + n(\left.\frac{dn}{d\lambda}\right|_{\lambda_0})^2 \tag{5.21}$$

We now require only $dP_1/d\theta$ and $d^2P_1/d\theta^2$ in order to obtain a complete expression for the dispersion. These can be expressed as,

$$\frac{dP_1}{d\theta} = X cos\theta(\lambda) - Y sin\theta(\lambda) \tag{5.22}$$

and

$$\frac{d^2P_1}{d\theta^2} = -X sin\theta(\lambda) - Y cos\theta(\lambda) = -P_1 \tag{5.23}$$

Further, it can be proved that at the central wavelength, λ_0,

$$\frac{dP_1}{d\theta} = ZR_0 \tag{5.24}$$

$$= A_0B_0 \tag{5.25}$$

where R_0, A_0 and B_0 correspond to the central wavelength λ_0. The details of this derivation are provided in Appendix A.

Putting all the above expressions together we arrive at a final expression for the dispersion, D_1, coming from Part 1 of Figure 5-11 which is,

$$D_1 = \frac{d^2\phi}{d\omega^2} = \frac{\lambda_0^3}{2\pi c^2}\frac{d^2P_1}{d\lambda^2}\bigg|_{\lambda_0} \tag{5.26}$$

$$= \frac{\lambda_0^3}{2\pi c^2}\left[\left(\frac{d^2n}{d\lambda^2}\bigg|_{\lambda_0} + n\left(\frac{dn}{d\lambda}\right)^2\bigg|_{\lambda_0}\right)A_0B_0 - \left(\frac{dn}{d\lambda}\bigg|_{\lambda_0}\right)^2 P_1\right] \tag{5.27}$$

$$= \frac{\lambda_0^3}{2\pi c^2}\left[\frac{d^2n}{d\lambda^2}\bigg|_{\lambda_0} A_0B_0 - \left(\frac{dn}{d\lambda^2}\bigg|_{\lambda_0}\right)^2 B_0O\right] \tag{5.28}$$

Since Part 2 in Figure 5-11 is identical in configuration to Part 1, we can immediately write down an analagous expression for the dispersion D_2, as

$$D_2 = \frac{d^2\phi}{d\omega^2} = \frac{\lambda_0^3}{2\pi c^2}\frac{d^2P_2}{d\lambda^2}\bigg|_{\lambda_0} \tag{5.29}$$

$$= \frac{\lambda_0^3}{2\pi c^2}\left[\frac{d^2n}{d\lambda^2}\bigg|_{\lambda_0} C_0D_0 - \left(\frac{dn}{d\lambda^2}\bigg|_{\lambda_0}\right)^2 D_0O\right] \tag{5.30}$$

The total one-way intracavity dispersion D is just the sum of D_1 and D_2. That is

$$D = D_1 + D_2 \tag{5.31}$$

$$= \frac{\lambda_0^3}{2\pi c^2}\frac{d^2P}{d\lambda^2}\bigg|_{\lambda_0} \tag{5.32}$$

$$= \frac{\lambda_0^3}{2\pi c^2}\left[\frac{d^2n}{d\lambda^2}\bigg|_{\lambda_0}(A_0B_0 + C_0D_0) - \left(\frac{dn}{d\lambda^2}\bigg|_{\lambda_0}\right)^2(B_0O + D_0O)\right] \tag{5.33}$$

It is clear that the positive dispersion is proportional to the term $A_0B_0 + C_0D_0$ which is just the total path length of the beam within intracavity material. The negative dispersion is proportional to the sum $B_0O + D_0O = B_0D_0$, since for a given set of end elements the longer the cavity the larger the spatial separation between a pair of wavelengths when they traverse the material in either end-element and consequently the larger the amount of negative dispersion introduced.

As mentioned earlier, the above expressions are accurate only in the limit of

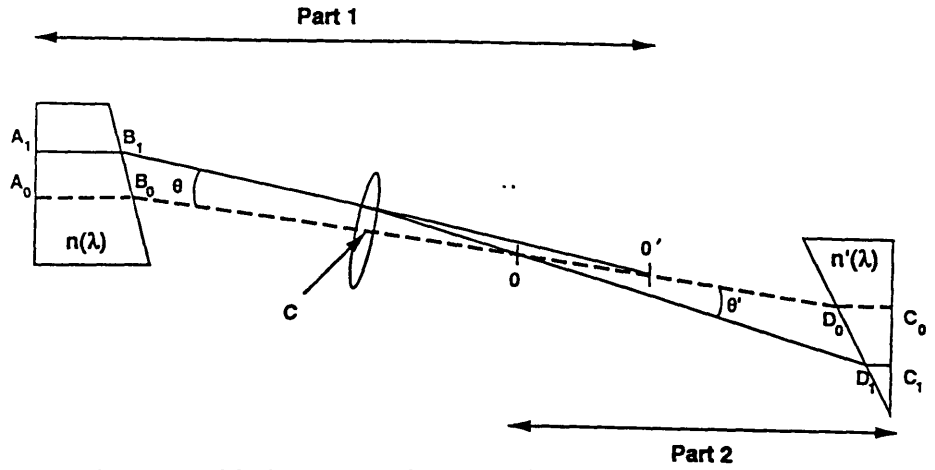

Figure 5-13: Equivalent unfolded cavity schematic for dispersion calculation in laser of Fig 5-6 assuming dissimilar $\frac{dn}{d\lambda}$ for the gain and the prismatic output coupler. Propagation axes for two different wavelengths are shown in solid and dashed lines. O is the intracavity intersection point between propagation axes. O′ is the virtual image of O through the lens.

Equation 5.10, when the gain and the prismatic output coupler have similar $\frac{dn}{d\lambda}$. However, this might often not be the case in which case the above analysis must be generalized. In the general case, the intersection point between propagation axes for different wavelengths, O, is distinct from the lens center, L. The situation is depicted in Figure 5-13. Since in this case the relative angle between two given wavelengths at each end element will be different, the lens serves to deviate the axes in order to "match up" these angles and permit the existence of a self-consistent intracavity path. It can easily be shown from the laws of ray optics that

$$B_0O' = B_0O + f\left[\frac{\theta'}{\theta} - 1\right] \tag{5.34}$$

$$D_0O = D_0L - f\left[1 - \frac{\theta}{\theta'}\right] \tag{5.35}$$

Note that the ratio θ/θ' is equal to the ratio $(dn/d\lambda)/dn'd\lambda)$. Viewed from the gain medium, the propagation axes all seem to emanate from the point O′ and so

we can again calculate the total cavity dispersion as arising from two parts as shown in Figure 5-13. We can write expressions for D_1 and D_2 in these two parts of the laser, in a completely analagous fashion to the earlier analysis. The final result, again evaluated at the central wavlength λ_0 is,

$$D = D_1 + D_2 \tag{5.36}$$

$$= \frac{\lambda_0^3}{2\pi c^2} \left.\frac{d^2P}{d\lambda^2}\right|_{\lambda_0} \tag{5.37}$$

$$= \frac{\lambda^3}{2\pi c^2} \left[\left.\frac{d^2n}{d\lambda^2}\right|_{\lambda_0} A_0B_0 + \left.\frac{d^2n'}{d\lambda^2}\right|_{\lambda_0} C_0D_0 - \left(\left.\frac{dn}{d\lambda}\right|_{\lambda_0}\right)^2 B_0O' - \left(\left.\frac{dn'}{d\lambda}\right|_{\lambda_0}\right)^2 D_0O \right] \tag{5.38}$$

As expected, in the limit that the two end elements have identical $\frac{dn}{d\lambda}$ Figure 5-13 reduces to Figure 5-11 and Equation 5.38 reduces to Equation 5.33 derived earlier. The distance of points O and O' from the lens center, L, is proportional to the ratio of $\frac{dn/d\lambda}{dn'/d\lambda}$ and the greater this ratio, the more critical it is that the generalized analysis be used to estimate the dispersion. The expressions derived in this section will be applied in the next section to estimate dispersion in the configurations implemented in the laboratory.

5.6 Experimental results

The laser geometry implemented was identical to that of Figure 5-6. Two configurations, one using a low dispersion LAKL21 prismatic output coupler (POC) and the other using a high dispersion SF10 POC were studied. 54 fs pulses at a repetition rate of 385 MHz, were achieved with the LAKL21 POC and 111 fs pulses at 1 GHz were produced in the configuration using an SF10 POC.

The Ti:Al_2O_3 gain medium is cut in a flat-Brewster geometry. It measures 3.17 mm on its shortest side and is doped 0.25 % Titanium by weight. The flat face is coated with a broad band high reflective coating at the lasing wavelengths (700 - 850 nm) and is also coated to be highly transmissive at the pump wavelengths.

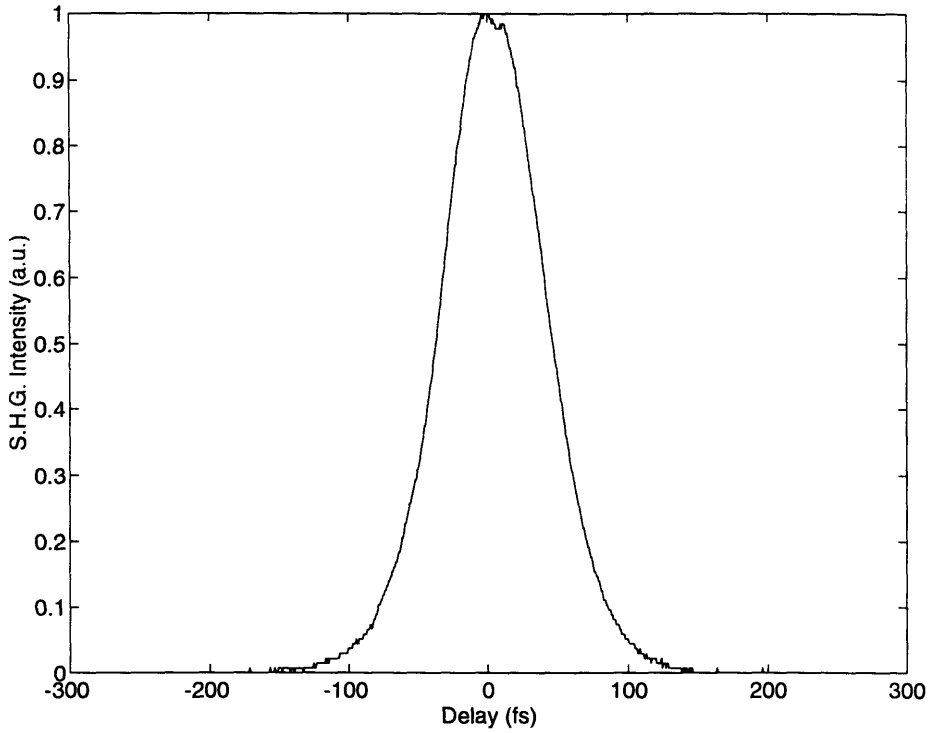

Figure 5-14: Autocorrelation of pulse from laser using LAKL21 POC. The pulse width is 54 fs assuming a $sech^2$ pulse shape.

The laser is pumped with all lines of an Argon laser, focused into the gain medium using a plano-convex lens. A focal length of 10 cm is used at 385 MHz and one of 5 cm is used in the 1 GHz configuration. A curved mirror of focal length 2.5 cm is placed at a distance slightly greater than 2.5 cm from the gain medium. The cavity is completed by a 1 % transmitting POC (either LAKL21 or SF10) , wedged at Brewster angle, with the uncoated face within the cavity. The coating on the prismatic output coupler is also a broad-band coating in the range 700-850 nm. The angle between the two cavity arms is optimized experimentally to minimize intracavity astigmatic effects. For operation at 385 MHz the substrate for the POC is LAKL21 which was chosen to minimize pulsewidth-limiting higher order dispersive terms. For operation at 1 GHz, an SF10 POC is used due to its higher dispersion.

Operating at a repetition rate of 385 MHz, with an LAKL21 output coupler, a stable train of pulses which measured 54 fs directly from the oscillator was produced

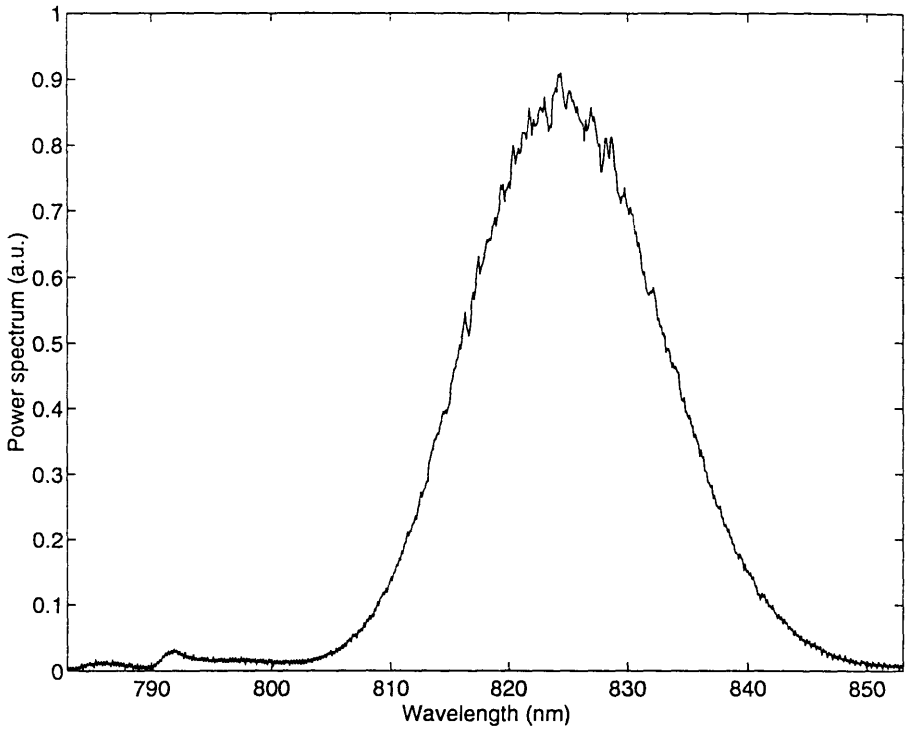

Figure 5-15: Spectrum of pulse from laser using LAKL21 POC. The spectral bandwidth is 17.9 nm. The resultanttime-bandwidth product is 0.45.

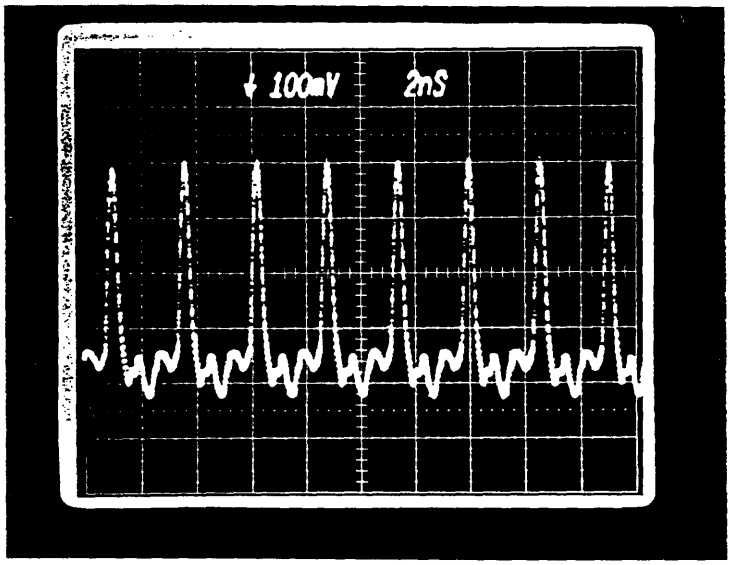

Figure 5-16: Pulse train at 385 MHz from laser using LAKL21 POC.

A_0B_0	3.2 mm
C_0D_0	0.5 mm
B_0O	2.18 cm
D_0O	35.5 cm
$(dn/d\lambda)_{.8\mu m}^{LaKL21}$	-.0261987 μm^{-1}
$(d^2n/d\lambda^2)_{.8\mu m}^{LaKL21}$	.065655 μm^{-2}
$(dn/d\lambda)_{.8\mu m}^{Ti:Al_2O_3}$	-.0267961 μm^{-1}
$(d^2n/d\lambda^2)_{.8\mu m}^{Ti:Al_2O_3}$	.0640994 μm^{-2}

Table 5.1: Values used to estimate dispersion in 385 MHz configuration using Equation 5.33.

. Figure 5-14 shows the background-free, non-interferometric autocorrelation of the pulse. A $100\mu m$ thick KDP doubling crystal was used in the autocorrelator. The pulse duration is 54 fs calculated assuming a $sech^2$ pulse shape. Figure 5-15 shows the corresponding spectrum measured using an optical multichannel analyzer (OMA). The spectrum fits well with a $sech^2$ shape and has a bandwidth of 17.9 nm yielding a time-bandwidth product of 0.45. Figure 5-16 shows the laser output pulse train measured using a fast photodetector connected to a high speed sampling scope. 100 mW of average output power was measured at a pump power of 3.5W.

The cavity length in this case was $\sim$ 38 cm. Using Equation 5.33 with the values provided in Table 5.1 we had estimated that a second arm length of 41 cm would be required to produce -100 fs^2 round-trip cavity dispersion. The optimized experimental value of 35.5 cm was not far from this estimate and we could thus be confident of using our earlier developed analysis in oscillator design. The calculated dispersion for the experimental cavity length is approximately -40 fs^2. Since $dn/d\lambda$ for sapphire and LAKL21 are almost identical, as expected, the difference between the estimates of dispersion from Equations 5.33 and 5.38 was negligible i.e. less than 2%.

To achieve an even higher repetition rate we used SF10 instead of LAKL21 as a substrate for the POC. SF10 has a much higher value for $dn/d\lambda$ than LAKL21 and consequently a much shorter cavity length is attainable while remaining in the net

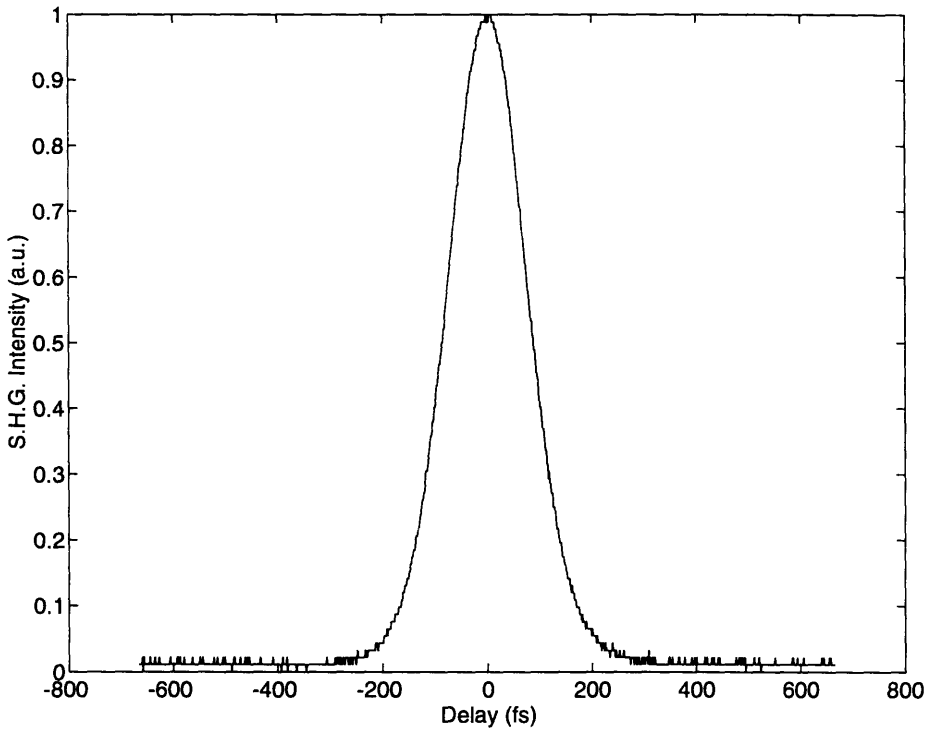

Figure 5-17: Autocorrelation of pulse from laser using SF10 POC. The pulse width is 111 fs assuming a $sech^2$ pulse shape.

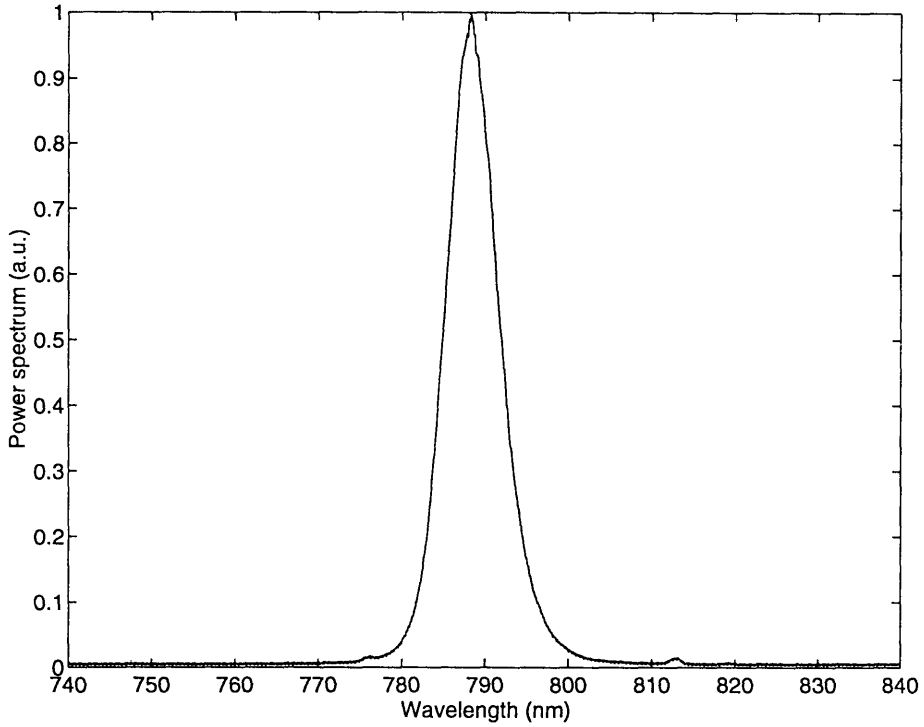

Figure 5-18: Spectrum of pulse from laser using SF10 POC. The spectral bandwidth is 7 nm. The resultant time-bandwidth product is 0.375.

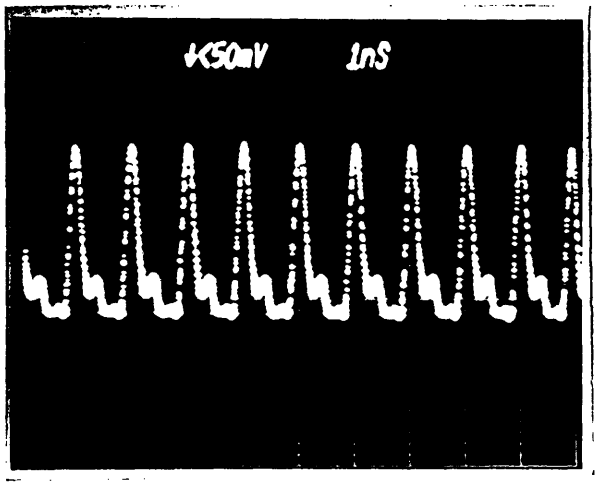

Figure 5-19: Pulse train at 1 GHz from laser using SF10 POC.

A_0B_0	3.2 mm
C_0D_0	0.5 mm
B_0O	2.18 cm
D_0C	12.5 cm
B_0O'	4.31 cm
D_0O'	11.35 cm
$(dn/d\lambda)^{sf10}_{.8\mu m}$	-.0495844 μm^{-1}
$(d^2n/d\lambda^2)^{sf10}_{.8\mu m}$	.175505 μm^{-2}
$(dn/d\lambda)^{Ti:Al_2O_3}_{.8\mu m}$	-.0267961 μm^{-1}
$(d^2n/d\lambda^2)^{Ti:Al_2O_3}_{.8\mu m}$	.0640994 μm^{-2}

Table 5.2: Values used to estimate dispersion in 1 GHz configuration using Equation 5-13.

negative dispersion regime. The experimental cavity length achieved was 15 cm which corresponded to operation at 1 GHz. The estimated dispersion in this configuration using Equation 5.38 and the experimental values provided in Table 5.2 was -30 fs^2. The autocorrelation, spectrum and pulsetrain recorded with the same diagnostics as described above are shown in Figures 5-17, 5-18 and 5-19. The pulsewidth is 111 fs assuming a $sech^2$ shape and the spectral bandwidth is 7 nm yielding a time-bandwidth product of 0.375. 600 mW of average power was measured at a pump power of 5.5W.

In both configurations modelocking is achieved operating close to the inner stability boundary of the cavity. Once CW performance is optimized, modelocking is achieved by adjusting the distance of the pump lens from the gain medium as well as its transverse position in relation to the gain medium. Self-starting operation was often observed, which we believe is qualitative proof of previous predictions of very strong saturable absorber action at the edges of the stability region [34]. When the laser was not self-starting, modelocking was inititated by a small mechanical perturbation. Once modelocked the laser remained modelocked for hours without any enclosure.

5.7 Further improvements

The above demonstrations serve to conclusively establish the potential of this novel, compact, high repetition rate KLM laser geometry. The simplicity, ease of use and stability of the KLM laser implemented is unprecedented, and we hope that it will significantly simplify the day-to-day use of such systems as well as their potential for commercial manufacture and sale. It is worth noting that owing to the reduced parameter space of the geometry deomonstrated, the search for the modelocked operating point is remarkably easier and faster than in the preceding standard X or Z fold KLM laser geometries.

Minimization of the amount of intracavity material has already been proven to be an important consideration for achieving short pulses [39, 38, 3]. Since it truly eliminates all superfluous components and intracavity glass, the demonstrated cavity geometry may be useful in achieving and exploring the sub 10 fs regime of operation for KLM Ti:Al_2O_3 lasers. Currently, the limitation on pulsewidth appears to be the inherent lateral spread of wavelengths in the gain medium. This is plausible because the estimated spread for the 18 nm bandwidth recorded in the 385 MHz configuration is $\sim$ 38 μm which is on the order of the $\sim$ 32 μm diffraction limited beam diameter of the pump in the gain crystal. Thus a focussed pump beam serves as a bandwidth limiting element which constrains attainable pulse durations from this laser. However, by shaping the pump beam and making it sufficiently elliptical, this effect can be minimized. Preliminary evidence for the improved bandwidth attainable by using an elliptically shaped pump mode, or simply increasing the size of the pump mode was already seen in the laboratory. However, care must be taken to maintain sufficient saturable absorber action when doing this. A more detailed investigation of the effect of nonlinearity on the intracavity mode may lead to the discovery of a suitable position for an intracavity slit which could serve as the intensity-dependent loss mechanism. This would increase the flexibility of the design by decoupling the saturable absorber action from the size of the pump beam.

As already demonstrated the cavity repetition rate is scalable merely by use of more dispersive materials as POCs. Clearly such materials will also limit the attainable pulsewidth by introducing large amounts of higher order dispersive terms. However pulsewidth may not be a crucial parameter in some applications of a high repetition rate pulsed source.

In both of the implemented configurations the spatial mode of the output beam was found to be elliptical with a 2:1 to 3:1 ratio. This is attributed due to imperfect compensation of astigmatism at the edge of the stability regions where KLM action occurs. A more careful analysis of the astigmatic properties of the cavity will allow proper compensation over a wider range in the stability region and thus reduce the ellipticity of the output beam. Note however that there is an inherent ellipticity in the output beam due to the lateral spread of spectral components throughout the laser. Of course, the spectral components at the output of the laser are collimated, and the situation is identical to the folded X or Z cavity when the output is taken at the dispersive end of the cavity. We estimate an upper bound for the lateral spatial spread of wavelengths over a 20 nm bandwidth in the 385 MHz configuration to be about 40 μm in the gain and about 560 μm at the output. This is small compared to the laser output mode size of about 2 mm in the vertical dimension. If, however, the magnitude of the spread in the current configuration is unacceptable, the output can be obtained from the gain side of the cavity or alternatively a prism pair external to the cavity could be used to superimpose the spectral compenents.

5.8 Dispersive resonator geometries

It is clear that based on the above concepts relating to dispersion compensation and its achievement through the use of cavity geometry, one can conceive of other designs for resonators that could provide negative dispersion. As explained earlier, the key point is that the resonator geometry and the intracavity prismatic interfaces must enforce

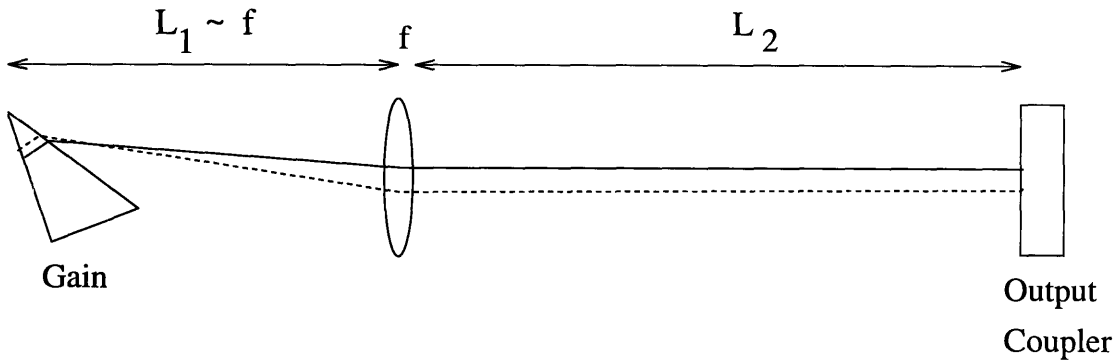

Figure 5-20: An alternative geometry for a dispersive resonator. The solid and dashed lines represent propagation axes corresponding to two distinct wavelengths. The prismatic element would serve as the gain medium in this geometry.

the spatial separation of the self-consistent propagation axes representing different Gaussian monochromatic modes. If this separation results in the propagation of relatively longer wavelengths through relatively more intracavity material, negative dispersion will be introduced. The magnitude of the negative dispersion introduced in this manner is entirely a function of the particulars of the cavity geometry and materials.

Figures 5-20 through 5-23 represent four alternative configurations for the generation of negative dispersion. Figure 5-20 shows a geometry using only one prismatic end element. If this element is chosen to serve as the gain medium the distance L_1 must be approximately equal to f, since the intracavity mode must come to a tight focus in the gain medium for sufficient power extraction. The distance L_2 is arbitrary. In this configuration the propagation axes would have to intersect very close to the prismatic gain element, (a distance f away from the lens on the side of the gain), in order to propagate self-consistently through the resonator. From the analysis of dispersion presented earlier, it is clear that the negative dispersion introduced is proportional to the distance from the prismatic gain to the point of intersection of the propagation axes. This is because this distance determines the separation of the

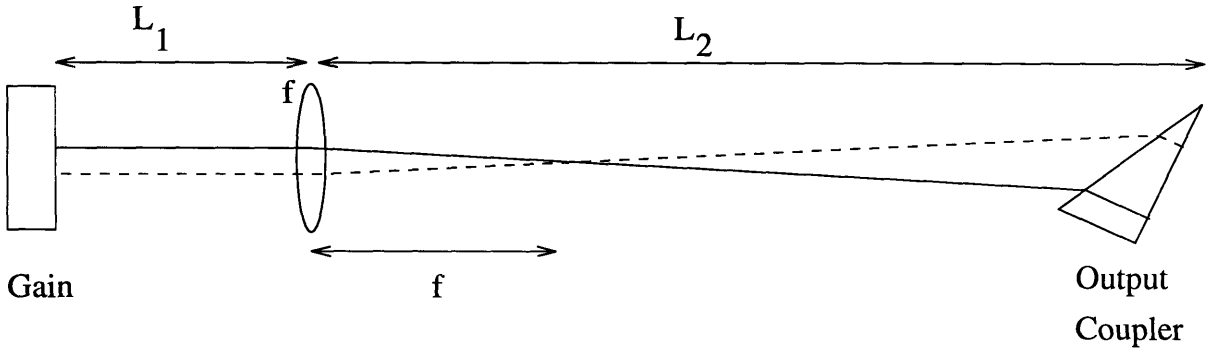

Figure 5-21: An alternative geometry for a dispersive resonator. The solid and dashed lines represent propagation axes corresponding to two distinct wavelengths. The prismatic element would be the output coupler in this geometry.

propagation axes within the material of the prismatic gain. Consequently the geometry of Figure 5-20 would not produce much negative dispersion because the point of intersection of propagation axes is in fact very close to the prismatic element.

Figure 5-21 swaps the end elements of Figure 5-20. Now the propagation axes would intersect at a distance f away from the lens but in the longer arm of the cavity. The amount of dispersion would be proportional to the distance (L_2 - f) in Figure 5-21.

Figure 5-22 is a combination of the earlier two geometries. In fact it is the geometry implemented in this thesis, with the curved mirror having been replaced with a lens. Under the assumption of materials with similar $dn/d\lambda$ being used for both end elements, the propagation axes intersect close to the center of the lens. In this case both arms of the laser will contribute to the total negative dispersion introduced. However, for the aforementioned reasons, clearly the contribution from the longer resonator arm will dominate.

Figure 5-23 shows a folded-X cavity geometry, familiar from earlier Ti:Al_2O_3 lasers, with both end mirrors replaced by prismatic output couplers. Note that this figure was also drawn under the assumption that the gain and prismatic output coupler are made of materials with similar $dn/d\lambda$. Drawing a symmetry plane through the

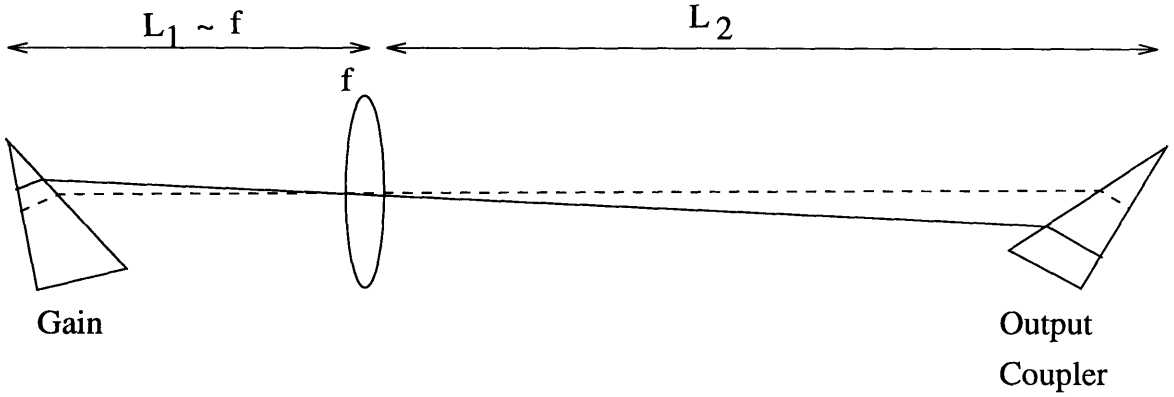

Figure 5-22: An alternative geometry for a dispersive resonator. The solid and dashed lines represent propagation axes corresponding to two distinct wavelengths. Prismatic elements would be used both for the gain medium and the output coupler in this geometry.

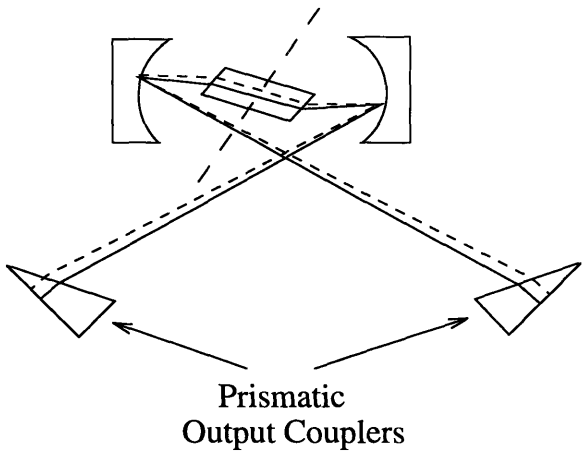

Figure 5-23: An alternative geometry for a dispersive resonator. The solid and dashed lines represent propagation axes corresponding to two distinct wavelengths. Each half of the resonator, on either side of the the line of symmetry drawn through the crystal, is identical to the resonator described and implemented earlier.

resonator as shown, one realizes that each half of the resonator is in fact identical to the resonator that has been implemented in this thesis. From this analogy, the total cavity dispersion can be calculated as the sum of the dispersion arising from the two resonator halves. The magnitude of the negative dispersion introduced will be dominated by the length of the two cavity arms.

5.9 Conclusion

In conclusion, a novel, compact dispersion compensation scheme has been discussed and implemented. It uses prismatic end elements in order to achieve net negative intracavity dispersion using laser geometry alone, thus avoiding the introduction of prism pairs or special mirrors for dispersion compensation. It has been explained theoretically and demonstrated experimentally how cavities which can support the coexistence of monochromatic modes propagating along spatially separated axes can provide negative dispersion, and can be designed simply with the use of prismatic end elements. 111 fs pulses have been achieved at a repetition rate of 1 GHz and 54 fs pulses at a repetition rate of 385 MHz. The laser geometry is simple and easy to use with a minimal number of components. Such minimization of intracavity material may prove crucial for the generation of exceedingly short pulses. Use of a monolithic element for both angle dispersion and output coupling, as well as the avoidance of excess chirp due to passage through an output coupler substrate, are novel and useful features of the demonstrated configuration. Lastly, this configuration is readily adaptable to diode pumped materials.

This dispersion-compensation technique and laser geometry may have important implications for the development of compact and simple femtosecond sources. It is hoped that as was the case with the folded-X and Z cavity geometries, this scheme will soon spread from its first demonstration in Ti:Al_2O_3 to various broad-band diode-pumpable materials of great interest such as Cr:Forsterite, Cr^{4+}:YAG,

Cr^{3+}:$LiSrCaAlF_6$ and Cr^{3+}:$LiCaAlF_6$. It is believed that in conjunction with the convenience of diode-pump sources this geometry will enable the construction of a practical, compact and low-cost femtosecond technology.

Chapter 6

Cavity Dumped, femtosecond Kerr lens modelocked Ti:Al_2O_3 laser

6.1 Introduction

As described earlier, femtosecond laser systems are now widely used for the study of ultrafast phenomena in physics, chemistry and biology. Time-resolved spectroscopy has become an invaluable tool for studying processes that happen on sub-picosecond time scales. Carrier dynamics in semiconductor materials, transport in solid-state devices and interaction of molecules during important biological processes such as photosynthesis are just a few of the phenomena that occur on femtosecond timescales.

An optimum laser source for such studies in ultrafast nonlinear spectroscopy should possess a short pulse duration, wavelength tunability, sufficient pulse energy to permit the investigation of nonlinear effects, and sufficient repetition rate to permit the use of signal averaging techniques for high sensitivity detection. Since femtosecond lasers are often used by specialists in fields other than lasers, system simplicity and reliability are also important considerations. Finally, of course a cost-effective

system is always desirable.

The broad gain bandwith of the femtosecond Ti:Al_2O_3 medium has made possible the development of sources with extremely short pulse durations as reviewed earlier [3, 5, 105]. The Kerr Lens Modelocked (KLM) Ti:Al_2O_3 laser is unprecedented in its simplicity, and reliability. Unlike their predecessors the femtosecond-dye lasers, Ti:Al_2O_3 and other solid-state lasers are widely tunable which is an extremely valuable feature for the spectroscopist. The pulse energies of $\sim$ 5 - 10 nJ per pulse available directly from Ti:Al_2O_3 lasers are far in excess of the pulse energies of $\sim$ 100 pJ available previously from femtosecond dye lasers. For all of these reasons solid-state lasers and in particular Ti:Al_2O_3 lasers are rapidly replacing dye laser technology and becoming an established tool in laboratories investigating ultrafast phenomena.

Despite all of their advantages however, the performance of KLM Ti:Al_2:O_3 lasers is often inadequate for the requirements of the nonlinear spectroscopist. Nonlinear effects rely on high peak intensity of excitation. Since

$$P_{peak} \sim E_{pulse}/\tau_{pulse} \tag{6.1}$$

where E_{pulse} is the pulse energy, and τ_{pulse} the pulse duration, the greater the pulse energy and the shorter the pulse duration, the stronger the nonlinear signal attainable. The output energies ($\sim$ 10 nJ) and pulse durations ($\sim$ 100 fs) from typical Ti:Al_2O_3 lasers yield peak powers that are only in the vicinity of 0.1 MW. While this is significantly higher than the peak powers in the kW range previously attainable from dye lasers, it is still insufficient for the study of many nonlinear phenomena. Significantly, the peak powers directly attainable from the Ti:Al_2O_3 oscillator are not sufficient for the generation of a white-light continuum which is often an important tool for the nonlinear spectroscopist [54, 78, 25].

Several complicated schemes to amplify femtosecond pulses from Ti:Al_2O_3 sources have therefore been demonstrated. These developments will be overviewed in more detail in the next section. However, at the time of this work there did not exist a

simple scheme for enhancing pulse peak powers achievable directly from the oscillator. It is for this reason that a cavity dumped femtosecond KLM Ti:Al_2O_3 oscillator was developed and forms the subject of this chapter. Using cavity dumping, a significant fraction of the intracavity pulse energy can be switched out in a single modelocked pulse. Since the dumping process is non resonant and broad-band, the original oscillator pulse duration can be preserved. Consequently, as demonstrated in this thesis, the technique of cavity dumping can be used to enhance pulse peak power by a factor of about 10 over that achievable directly from the oscillator. The cavity-dumped source is also attractive because it preserves laser tunability and provides a variable repetition rate.

The organization of this chapter is as follows. Section 6.2 reviews existing schemes for amplifying femtosecond pulses and places the cavity-dumped oscillator in context. Section 6.3 discusses the technique of cavity dumping. Section 6.4 describes the cavity dumped KLM Ti:Al_2O_3 oscillator and presents the experimental results. Section 6.5 discusses experimental limitations as well as the future potential of the cavity-dumped femtosecond Ti:Al_2O_3 oscillator.

6.2 Amplification of femtosecond pulses

Amplification of femtosecond pulses is a complicated problem. Several undesirable linear and nonlinear optical effects need to be considered in designing an amplifier which is able to sufficiently amplify a femtosecond pulse without altering its temporal shape or spatial profile. Linear optical aberrations, group velocity dispersion, self-phase-modulation, gain saturation, amplified spontaneous emission, pump nonuniformity and fluctuations are all important deleterious effects in a femtosecond amplification system [55].

Since femtosecond dye lasers were not tunable and produced pulse peak powers only in the kW range, several techniques to extend the energy and tunability of

these pulses have been developed. The characteristics of the amplification scheme are strongly linked to the characteristics of the pump source for the amplifier stages. Therefore amplification schemes have used a variety of pumping schemes to achieve different results. Pulses from a colliding pulse modelocked (CPM) dye laser were invariably the seed for the amplifier. These pulses are in the 50 fs range with pulse energies of about 100 pJ at repetition rates of 100 MHz. A Q-Switched Nd:YAG system was the first system used to amplify such pulses and it produced 1 mJ, 90 fs pulses at a 10-20 Hz repetition rate [24, 44]. The amplifier consisted of four dye-gain stages, several saturable absorber stages and a grating pair for cancellation of dispersion originating in the amplifier. Pumping a dye amplifier with two gain stages using a regeneratively amplified YAG laser synchronized to the CPM seed oscillator, has produced 100 fs pulses at repetition rates of about 1 KHz and pulse energies of 1 to 5 mJ [18]. One of the most popular dye laser amplification systems is the copper vapor laser-pumped, multi-pass, single-stage dye-amplifier which produces 35 - 70 fs pulses with 1 μJ pulse energy at a repetition rate of 8 kHz [56].

The emergence of the Ti:Al_2O_3 medium has proven to be a great advance not only for femtosecond lasers but also for femtosecond amplification technology. Ti:Al_2O_3 is an excellent amplification medium owing to its high energy storage capacity, long upper state lifetime ($\sim$ 3 μs) and high thermal conductivity. As a result, alongside ongoing efforts to reduce the achievable pulse durations from Ti:Al_2O_3 oscillators, much effort has been directed toward the amplification of such pulses in Ti:Al_2O_3 amplifiers.

The technique for amplification most commonly used has been that of chirped pulse amplification or CPA [110]. In this technique, femtosecond pulses from the oscillator are intentionally chirped before entrance into the amplifier system, in order to allow amplification of pulse energy by large amounts without reaching peak power levels that correspond to damage thresholds of the amplifier components. Pulses exiting the amplifier can be recompressed to durations close to those measured directly

from the seed oscillator. Of the several milestones which can be identified in the development of this technology only a few representative works will be mentioned here.

Amplification of synchronously pumped dye-laser pulses in a regenerative Ti:Al_2O_3 amplifier produced 300 mJ of energy in 22 ps pulses at 1 KHz [116]. The first amplification of a self-modelocked Ti:Al_2O_3 laser using a regenerative Ti:Al_2O_3 amplifier was demonstrated in 1990 to produce 105 fs pulses at peak powers of 10 GW and repetition rates of 20 Hz [116]. Subsequently kilohertz and multikilohertz operation of regenerative amplifier systems at the mJ and 100 μJ level respectively were also demonstrated [92]. Due to the superior energy storage properties of the Ti:Al_2O_3 amplifier medium, μJ energies at a repetition rates as high as 400 kHz have been produced in a cw-argon pumped regenerative amplifier system [77] .

Impressive optimizations in CPA systems using regenerative amplifiers have recently made possible the amplification of 20 fs pulses up to the 500 mJ level at 10 Hz [7]. This corresponds to a pulse peak power of several terrawatts. Multipass amplifiers have also been optimized in order to amplify 18 fs pulses to microjoule levels at kHz repetition rates [106].

The above described advances in amplifier technology are undoubtedly impressive and of great interest for many applications. However, the requirement of multiple stages and/or multiple pump lasers makes all of these oscillator-plus-amplifier systems complex, high-maintenance and relatively expensive. Further, the repetition rates of many of these sources is low enough to limit detection sensitivity for ultrafast measurements since signal averaging and phase sensitive detection techniques benefit from repetition rates of several KHz. Finally the repetition rate of all such systems is fixed and thus limits their versatility as sources for nonlinear spectroscopy.

A cavity-dumped femtosecond Ti:Al_2O_3 oscillator has the potential for rectifying many of these drawbacks. As will be explained in detail in the following section, cavity dumping is a technique by which output pulse energies from a modelocked

oscillator can be significantly enhanced at the expense of pulse repetition rate. An intermediate energy level (50 - 100 nJ) Ti:Al_2O_3 system with MHz repetition rates can therefore be implemented exploiting this technique. Since the dumping process is non resonant and broad-band, the oscillator pulse duration is maintained, resulting in peak powers in the MW range. The threshold for many interesting nonlinear phenomena is indeed in the 1 MW peak power range. Such a source would therefore be very simple and useful for the nonlinear spectroscopist who does not desire to build a complex oscillator-plus-amplifier system.

Further, the cavity-dumped source is also attractive because it provides a variable repetition rate. The pulse repetition rates directly from Ti:Al_2O_3 lasers are often too high for ultrafast measurements that require high pulse peak intensities. The resultant average powers that the samples are subjected to are excessive and can cause thermal damage. Sometimes pulse repetition rates from the oscillator need to be intentionally reduced using "pulse-picking" schemes in order to provide enough time for thermal relaxation of samples. Consequently, a source with a variable repetition rate in the MHz range is quite desirable for the spectroscopist facing such problems from a standard Ti:Al_2O_3 oscillator.

6.3 Cavity dumping

Cavity Dumping is a technique by which the output coupling from a laser cavity is suddenly switched to a very large value, resulting in the "dumping" of all or a large fraction of the intracavity pulse energy into an output pulse. Since the intracavity pulse energy is inversely proportional to the output coupling this technique can result in large enhancements of pulse energy in the presence of sufficiently low transmission output couplers. The period for which the output coupling is switched to a high value should ideally be exactly one cavity round trip time in order to ensure maximum energy in the "dumped" pulse. Though the technique can be used for continuous

wave, Q-switched or modelocked lasers this discussion will focus on the modelocked case which is relevant to this thesis.

Electro-optic or acousto-optic techniques can be used for cavity dumping. Electro-optic dumping is usually achieved by introduction of an electro-optic Pockels cell and a polarizer into the cavity. Switching the voltage across the Pockels cell by the "half-wave voltage" then results in dumping of the cavity energy. Since half-wave voltages for common Pockels cell materials are in the range of several hundred volts, it is difficult to achieve electro-optic dumping at MHz repetition rates. Consequently the technique of acousto-optic dumping pictured generically in Figure 6-1 was used.

An acousto-optic cavity dumper consists of a travelling wave acousto-optic modulator (AOM), made of a fused silica cell and attached to a piezoelectric transducer (PZT) driven by a source of radiofrequency (RF) pulses. When the dumper is turned on, the RF pulse source sets up acoustic travelling waves in the dumper cell. These acoustic waves modify the local index of the dumper medium by the photoelastic effect and thus produce a phase grating off which the laser beam diffracts. The diffracted beam comprises the cavity dumped output.

The cavity dumper used in this thesis consisted of a Spectra Physics model 344S high efficiency dumper cell and a Spectra Physics model 454 cavity dumper-driver consisting of an RF oscillator and pulse generator. The dumper cell was composed of fused silica and was 2.5 mm thick. The RF oscillation frequency is chosen to be high ($\sim$ 779 MHz), in order to enable amplitude modulation by pulses on the timescale of the laser round trip time which is about 10 ns. Further, the high frequency of the acoustic wave also increases the diffraction angle for the output beam and makes it easier to extract from the cavity.

As shown in Figure 6-1 the dumper cell is placed in the focus of a pair of curved mirrors. This is done to ensure that the laser beam is tightly focussed when it interacts with the acoustic wave, since the transit time in the cell for the leading edge of the travelling acoustic wave from one edge of the beam to the other sets the rise time

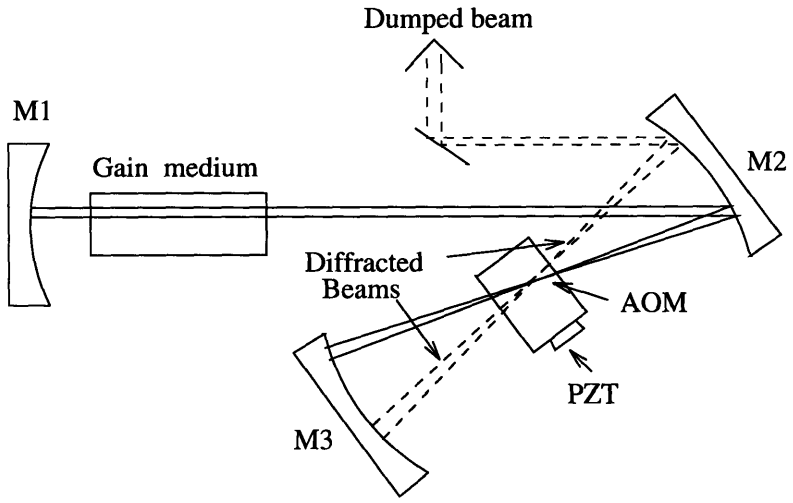

Figure 6-1: Typical arrangement for an acousto-otpic cavity dumper set up in a double pass configuration.

of the cavity dumped output. Notice also that the dumper is used in a double pass configuration which enhances the achievable diffraction efficiency. This can be proved by the derivation of a simple expression for the dumped laser output beam.

If the incident electric field on the dumper is:

$$E_{in}(t) = E_0 cos(\omega t) \tag{6.2}$$

then after one pass through the dumper the diffracted field is

$$E_d(t) = \sqrt{\kappa} E_0 cos(\omega - \Omega)t \tag{6.3}$$

where κ is the one pass dumper efficiency and Ω is the frequency of the acoustic signal. The remaining undiffracted intracavity beam is:

$$E_{ic}(t) = \sqrt{(1-\kappa)} E_0 cos(\omega t) \tag{6.4}$$

After reflection from the mirror M3 both beams are refocused into the modulator

where they interact again with the acoustic wave. Some of the diffracted beam will rejoin the intracavity beam and some of the intracavity beam will be diffracted once more so that the total diffracted output composing the dumped beam is:

$$E_{dump}(t) = \sqrt{(1-\kappa)}\sqrt{\kappa}E_0 cos(\omega-\Omega)t + \sqrt{\kappa}\sqrt{(1-\kappa)}E_0 cos(\omega+\Omega)t \quad (6.5)$$

$$= 2\sqrt{\kappa}\sqrt{(1-\kappa)}E_0 cos(\Omega t)cos(\omega t) \quad (6.6)$$

$$= 2\sqrt{\kappa}\sqrt{(1-\kappa)}E_{in}(t)cos(\Omega t) \quad (6.7)$$

Thus the intensity of the output is

$$I_{dump}(t) = \frac{1}{2\eta}\left|E_{dump}(t)\right|^2 \quad (6.8)$$

$$= \frac{1}{2\eta}\left[4\kappa(1-\kappa)\left|E_{in}(t)\right|^2 cos^2\Omega t\right] \quad (6.9)$$

$$= \frac{1}{2\eta}\left[2\kappa(1-\kappa)\left|E_{in}(t)\right|^2 (1+cos2\Omega t)\right] \quad (6.10)$$

$$= I_{in}(t)2\kappa(1-\kappa)(1+cos2\Omega t) \quad (6.11)$$

where η is the impedance of free space. From this expression it is clear that 100% dumping efficiency occurs in the double pass configuration configuration when the single pass efficiency κ is only 50% ie. $\kappa = 0.5$. In practice double pass efficiencies from acousto-optic dumpers are in the 70% range. Note that the modulation period of the dumped ouptut is on the nanosecond timescale which is several orders of magnitude longer than the femtosecond timescale of the dumped pulses. Thus for all practical purposes the amplitude of the dumped pulses can be considered constant.

When cavity dumping a modelocked laser, the timing between the modelocked pulses and the acoustic burst must be synchronized as pictured schematically in Figure 6-2. One acoustic burst is shown in an expanded view in Figure 6-3. Reflected light from an intracavity prism was fed to a photodetector and preamplifier assembly. This electronic output was used to trigger the cavity dumper in order to achieve the desired synchronization between the travelling acoustic bursts in the dumper and the

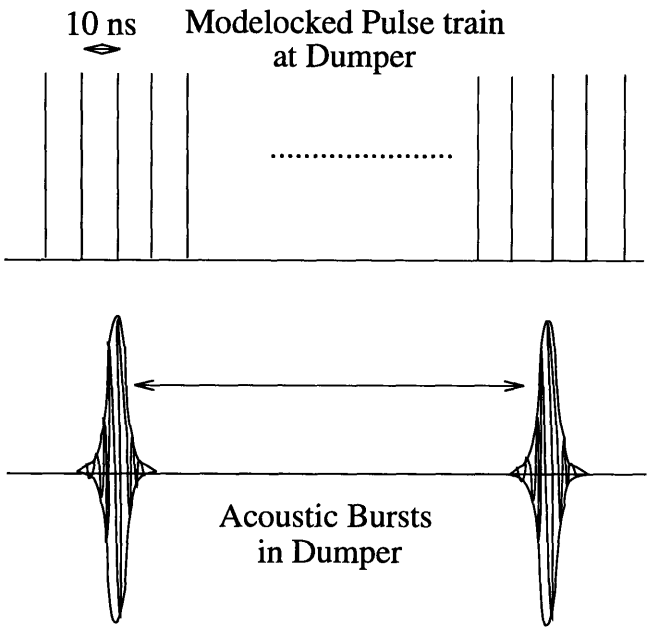

Figure 6-2: The acoustic bursts in the dumper are synchronized to the modelocked pulse train circulating in the laser.

intracavity pulse train. Fine tuning of the phase of the RF wave and the timing of the central peak were also possible and necessary in order to obtain the maximum contrast between the main dumped pulse and the neighbouring pulses.

6.4 Experimental results

A schematic of the laser cavity implemented is shown in 6-4. The gain medium was a short, 0.8 cm length, Brewster-angled Ti:Al_2O_3 crystal with a doping density of approximately 0.2 % wt.. The crystal was placed in an astigmatically compensated Z-fold formed by two 10 cm radius of curvature mirrors. The astigmatic compensation angle was 22 degrees. The laser was pumped by all lines of an Argon laser focused into the crystal using a 12.5 cm focal length lens. A 3.5% output coupler and a high reflector formed the two ends of the cavity. Four LAKL21 prisms provided second-order dispersion compensation while maintaining low third-order dispersion [38]. The

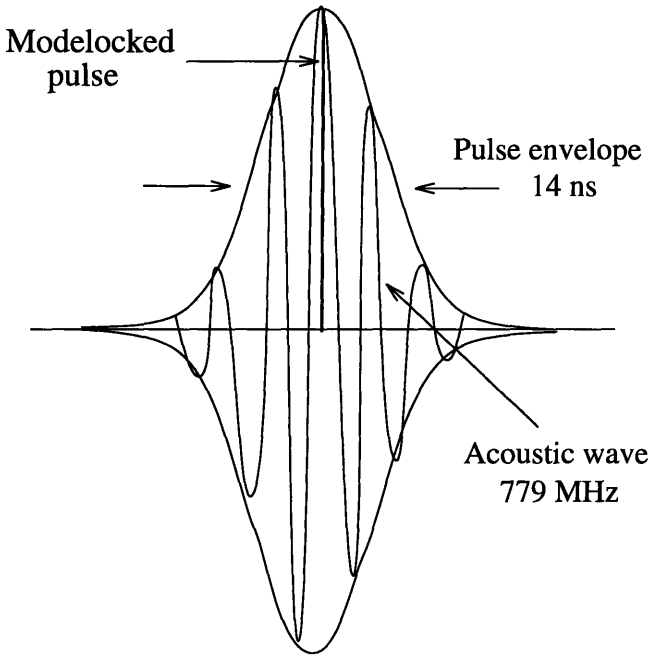

Figure 6-3: The acoustic wave at a carrier frequency of 779 MHz is modulated by an RF envelope of about 14 ns pulse width. The timing of the envelope peak and the phase of the acoustic wave are adjustable.

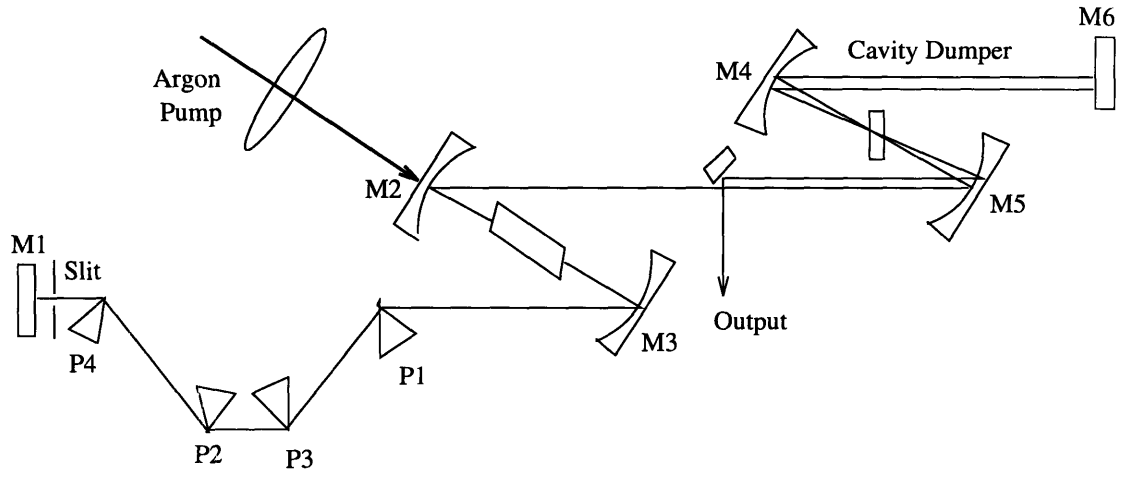

Figure 6-4: Schematic for cavity dumped femtosecond KLM Ti:Sapphire laser.

tip-to-tip distance for each prism pair was 20 cm. A slit of variable width was placed at one end of the cavity to enhance the fast saturable absorber, KLM effect. Kerr-lens modelocking was initiated by inducing a small mechanical perturbation in the laser.

The acousto-optic cavity dumper, Spectra Physics model 344S described in the previous section was placed at Brewster's angle in a second Z-fold. The cavity dumped output could be obtained at variable repetition rates as high as 950 kHz. The available repetition rates were discrete and determined by the driving electronics for the cavity dumper. Figure 6-5 and 6-6 show the dynamics of the intracavity laser pulse train during the dumping process at 952 kHz and at 454 kHz which were the two rates of operation most often used in this investigation. However, stable dumping was achieved at repetition rates of 95 kHz and 45 kHz also, as shown in Figures 6-7 and 6-8. At all of these repetition rates, each time a dumping event occurs the intracavity pulse train drops in intensity. After dumping, the intracavity pulse train recovers to its unperturbed level in approximately 500 ns. The recovery time was a function of the dumping efficiency and the pump power of the laser.

The typical dumping efficiency of approximately 50% was obtained by careful

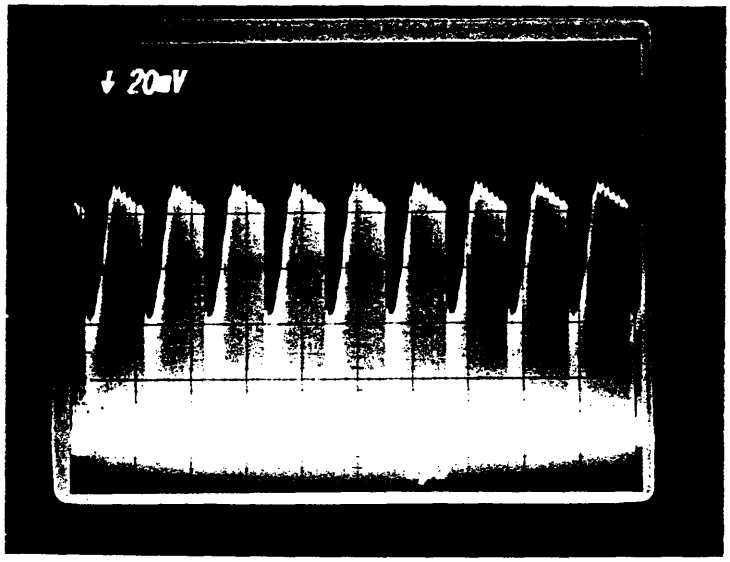

Figure 6-5: Intracavity laser pulse train during dumping at 952 KHz.

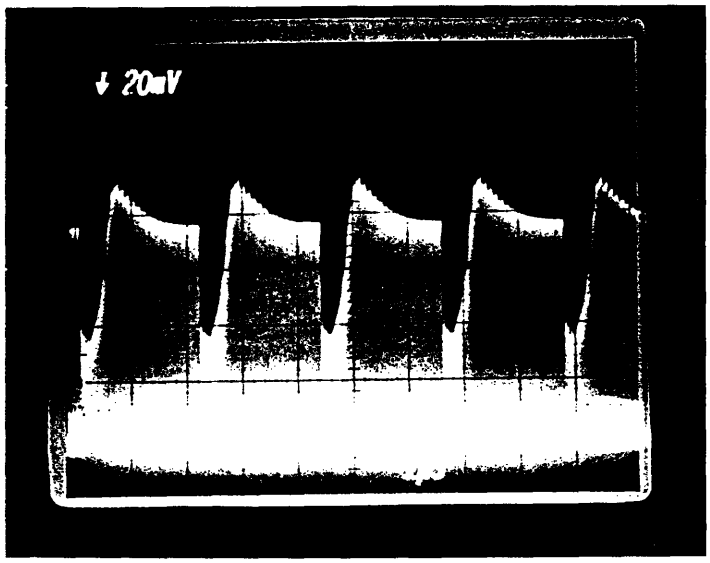

Figure 6-6: Intracavity laser pulse train during dumping at 454 KHz. Note the overshoot of the pulse train during recovery which is characteristic of the recovering laser undergoing relaxation oscillations.

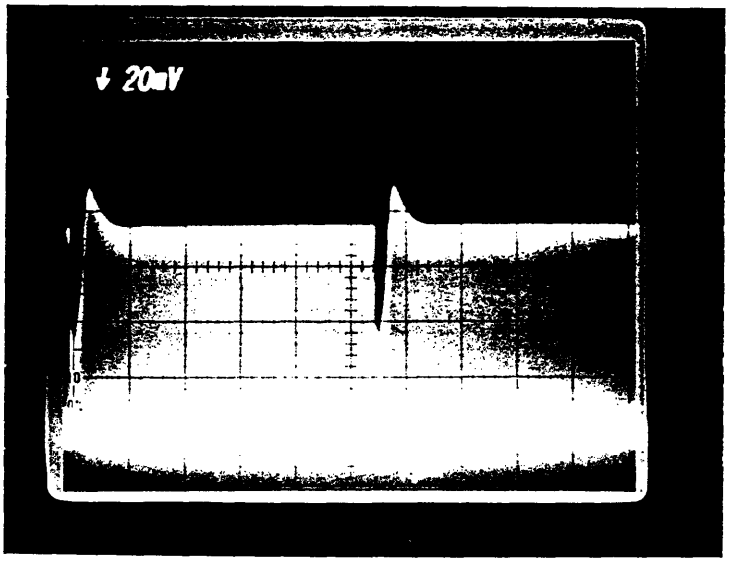

Figure 6-7: Intracavity laser pulse train during dumping at 95.2 KHz.

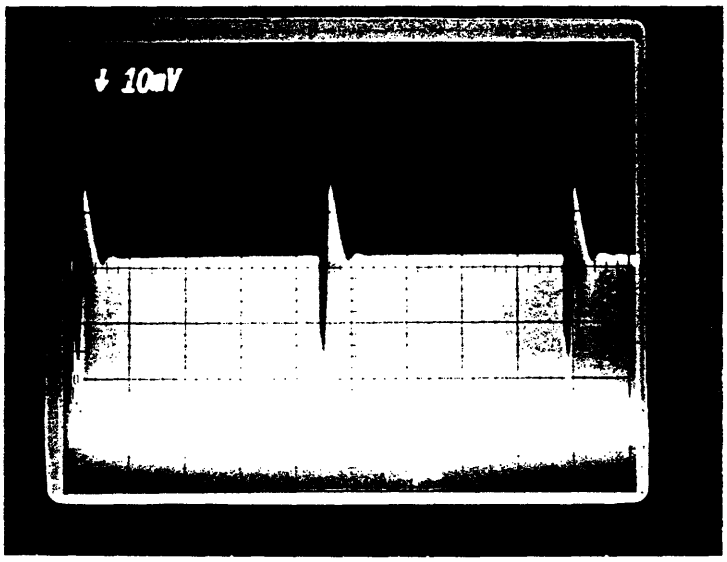

Figure 6-8: Intracavity laser pulse train during dumping at 45.4 KHz.

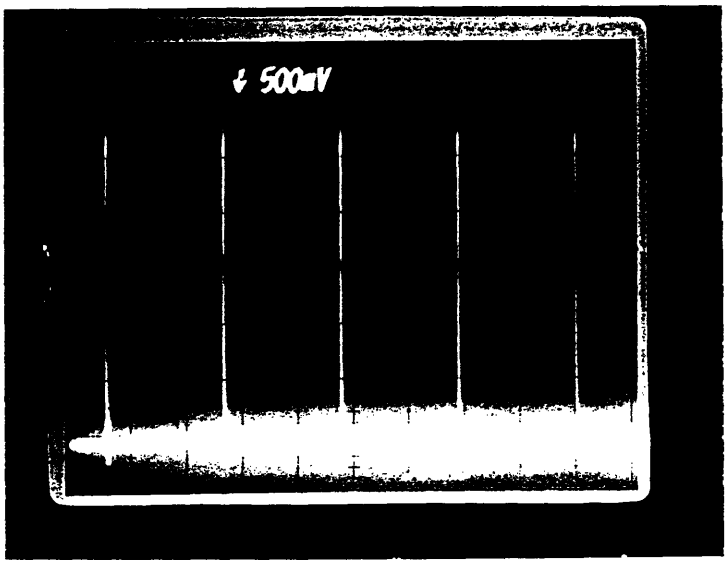

Figure 6-9: Dumped output pulse train. The contrast ratio between the main pulse and adjacent pulses is about 20:1.

alignment and optimization of the cavity dumper. The laser beam was made to traverse the dumper as close to the RF transducer as possible and the timing and phase controls on the cavity dumper-driver were adjusted for maximum dumped power. The transverse position of the dumper was also an important parameter that needed careful adjustment to obtain a strong interaction between the acoustic wave and the laser beam. An infrared camera was used to view and optimize the intensity of the dumped output beam.

Figure 6-9 shows the dumped output pulses. The contrast ratio between each dumped output pulse and its neighbouring pulses is 20:1. This high contrast ratio was achieved by adjusting the timing and phase of the acoustic burst such that the peak of the acoustic wave coincides with a modelocked pulse(see Figure 6-3). Since the cavity round trip time ($\sim$ 10 ns) is about 1.5 times the FWHM of the burst envelope ($\sim$ 7ns), such adjustment ensures that the next modelocked pulse falls almost outside the acoustic burst envelope.

Figure 6-10 shows the background-free autocorrelation of the a dumped laser pulse with an energy of 100 nJ. A 500 μm KDP crystal was used in the autocorrelator. 100

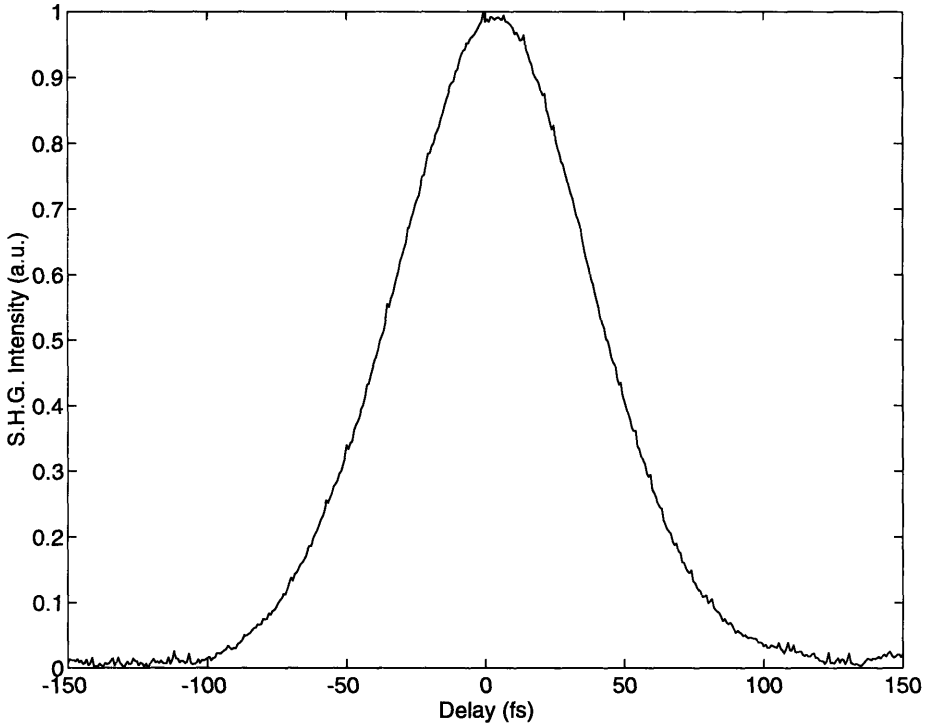

Figure 6-10: Autocorrelation of 100 nJ dumped output pulse. The pulse width is 50 fs assuming a sech^2 shape.

nJ was the highest dumped pulse energy observed from this system. The pulse width is 50 fs assuming a sech^2 pulse shape. The laser was pumped at 8.8 W to yield 100 nJ of energy per pulse. The corresponding dumped peak power is about 1 MW which is an order of magnitude in excess of the peak powers available directly from the oscillator. The shot-to-shot stability of the cavity dumped oscillator is comparable to that of the unperturbed oscillator, with pulse energy fluctuations of less than 5%.

Two SF10 prisms are used for dispersion compensation outside the laser cavity. The prisms are necessary to compensate for residual chirp on the the pulse since it is extracted at a point in the cavity where it is far from transform limited. Murnane et. al. have discussed the large ($\sim$ 30%) variations in pulse duration that occur as a pulse travels around a femtosecond laser cavity [38]. The external prism pair is also useful for precompensating chirp acquired during passage through the autocorrelator and other diagnostic equipment. The distance between these prisms was optimized experimentally.

Figure 6-11 shows the spectrum of the pulse. The bandwidth is 22 nm FWHM corresponding to approximately 1.5 times the transform limit. The spectrum of the dumped pulse is identical to the spectrum of pulses obtained at the output of the oscillator. Thus the dumping process does not introduce any spectral filtering of the pulse at the 50 fs level.

The traces of Figures 6-6 and 6-5 show that the laser continues to modelock stably throughout the dumping process. As discussed in chapter 2, in the steady state, Kerr-lens modelocking depends upon a balancing of nonlinear saturable absorption and self phase modulation against gain bandwidth limiting and dispersion. When the pulse energy is reduced immediately after dumping, the nonlinear saturable absorption and self phase modulation are significantly decreased; however the laser remains stably modelocked because the pulse broadening effects of bandwidth limiting and negative dispersion are not too severe.

The cavity dumping process also produces transient dynamics in the pulse energy.

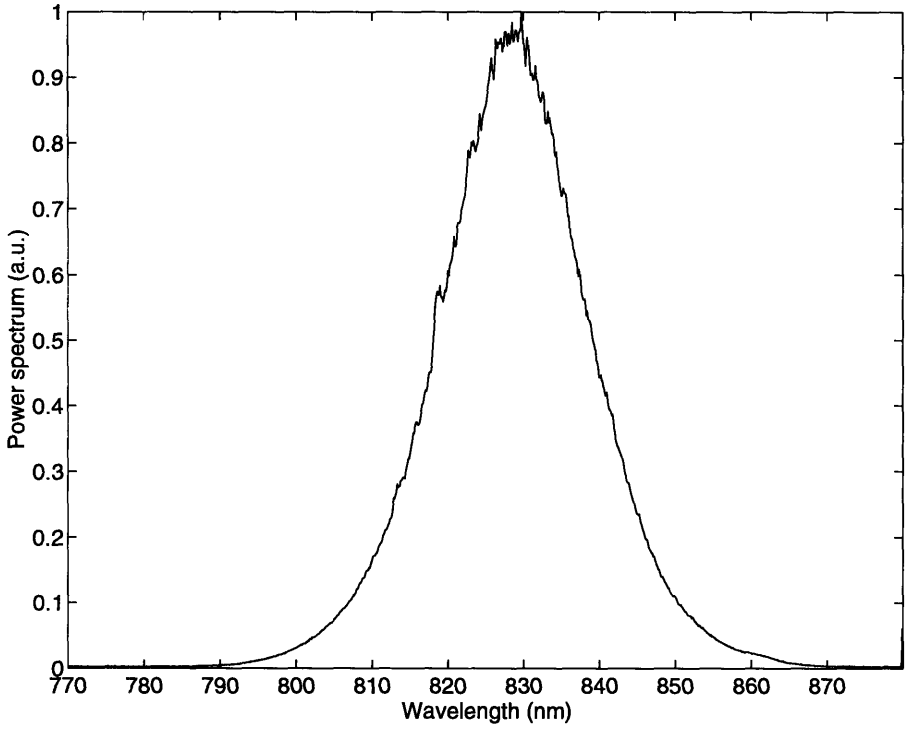

Figure 6-11: Spectrum of 100 nJ dumped output pulse. The spectral bandwidth is 22 nm, and the center wavelength is 830 nm.

Figures 6-6 and 6-5 exhibit a relaxation oscillation induced overshoot of the pulse energy above its steady state level. When the laser is perturbed by the dumping process, the coupling between the population inversion and the intracavity pulse energy results in oscillation of both quantities until a steady state is re-established. In our system the oscillations are highly-damped because of the large (3.5 %) output coupling. The amplitude and period of the relaxation oscillation are a function of the dumping efficiency (loss perturbation), the pump power, and cavity Q. This phenomena is of interest because it suggests that cavity dumping might be used to induce Q-switching or relaxation oscillation enhancement of the available output pulse energies from solid-state lasers. This behavior contrasts with previous studies of cavity dumping in dye laser systems, where the use of gain energy storage techniques to enhance pulse energy is not possible.

From the above results it is clear that cavity dumping maintains the performance advantages of modelocked Ti:Al_2O_3 lasers in terms of pulse duration, spectrum, stability, and tunability while providing a significant increase in pulse peak power with a variable pulse repetition rate. The approach also maintains system-simplicity by avoiding the use of a separate amplifier and/or separate pump laser.

6.5 Further improvements and advances

The limitation on the energy currently available from this source arises because of multiple pulse instabilities that occur at high pulse energies due to saturation of the KLM saturable absorber action. When intracavity pulse energies become excessively large ($\sim$ 200 nJ) the corresponding pulse peak powers are also very high and all intracavity nonlinear effects become magnified. When saturable absorber action and self-phase modulation become too severe it is more advantageous for the laser to redistribute the available intracavity energy among several pulses. Thus multiple pulsing instabilities become frequent as was observed in this work. This phenomenon

has also been predicted theoretically [34] and observed by other researchers [5].

Since the maximum peak intensity attainable in a single pulse is determined by the strength of the KLM nonlinearity, reducing the nonlinearity by techniques such as defocusing the beam within the crystal could reduce multiple pulse instabilities; however, this approach would make the laser harder to start. In this scenario the use of an active starting mechanism could prove useful.

It is well known that lowering the output coupling from a cavity dumped laser results in a significant enhancement of the available dumped pulse energies. This is because the intracavity power scales inversely with the output coupling. However the tendency toward multiple pulse operation in the limited the demonstrated system to an output coupling at 3.5%. Lowering the output coupler to 1% increased the cavity Q, but did not enhance the dumped energies since it reduced the pump level at which multiple pulse instabilities occured.

The more fundamental limit on the pulse energies ultimately achievable from this oscillator, is the optical damage threshold of both the crystal and the cavity dumper. Damage thresholds are not well documented in the literature though they are estimated to be in the 100 - 200 GW/cm^2 range for both sapphire and fused-silica. Since the peak powers in the demonstrated laser are already on the order of 150 GW/cm^2 it is questionable how much further acousto-optic dumping techniques can be pushed. In this context, electro-optic dumping is an alternative that cannot be ignored. However, while electro-optic dumping is characterized by high dumping efficiencies and optical damage is not an issue (since there is no need to focus into the dumper), the problem arises in attaining the 100 kHz repetition rate range. Using existing electro-optic dumping technologies this is very hard to achieve. Group velocity dispersion introduced by electro-optic dumpers (which are usually composed of several centimeters of rather dispersive materials such as lithium tantalate or deuterated KDP) is another significant problem that must be contended with.

It is worth mentioning that since the demonstration in this thesis of the feasibility

of the cavity-dumped Ti:Al_2O_3 source, ultrafast spectroscopists in the Netherlands have reproduced this technique in an exceedingly short pulsed oscillator [86]. They have generated 13 fs dumped pulses with 60 nJ of energy per pulse corresponding to peak powers of 5 MW. Using their source they have been able to generate a white light continuum in a fiber. The spectrum of the pulses after passage through the fiber extends from 500 nm to 1000 nm. Such a white-light continuum generated directly from an oscillator is a significant breakthrough in the development of convenient sources for spectroscopy. Further, compression of the output spectrum from the fiber has produced 7.5 fs pulses which are the shortest pulses produced from a solid-state source to date. These advances are very encouraging for they support the relevance and versatility of the cavity dumped source for ultrafast studies.

Chapter 7

Conclusion

This thesis has dealt with various aspects of femtosecond pulse generation in solid-state lasers. The research reflects the key forces that have driven and shaped the field during the past four years. The main contributions of the thesis are now summarized as follows:

The technique of Microdot mirror modelocking has been demonstrated to be a flexible and convenient way to modelock a variety of solid-state lasers. Microdot mirror modelocking was used to modelock a laser-pumped Ti:Al_2O_3 system to produce 190 fs pulses. It was also extended to a lamp-pumped Nd:YLF system to produce 2.3 ps pulses with 800 mW of output power. Microdot mirror modelocking has the advantages of modularity, compactness, tunability and convenience. It suffers from the drawbacks of introducing additional dispersion into the laser cavity. While sub 50 fs systems cannot be implemented with this technique, long pulse and lamp-pumped systems can definitely benefit from its use. The technique itself can be improved by refining the microdot mirror fabrication process. More detailed modeling of the effects (on linear and nonlinear resonator modes) of introducing the microdot mirror assembly into a specific cavity could also prove useful.

An iterative numerical procedure to model self-focusing in a resonator was written. It is based on the simple description of self-focusing as a nonlinear scaling of the

Gaussian beam q-parameter [8, 40]. While it does not account for complex effects such as astigmatism and thermal lensing it provides an intuitive and convenient tool for understanding the behavior of nonlinear resonators. It has been used to characterize the linear and nonlinear behaviour of a simple resonator configuration closely related to the compact laser geometry also implemented in this thesis.

A compact, gigahertz, KLM femtosecond oscillator was developed using a novel method for dispersion compensation. 111 fs pulses were produced at a repetition rate of 1 GHz and 54 fs pulses at a repetition rate of 385 MHz. A novel and compact method of dispersion compensation technique based on the spatial separation of propagation axes arising from the geometry of the resonator was conceived, analyzed and implemented. The above-mentioned iterative model for modeling self-focusing in a laser cavity was also used in the design of the compact femtosecond laser.

Features of this oscillator that require further study include the elimination of astigmatic effects in the resonator and the minimization of bandwidth limiting coming from the spectral spread of wavelengths in the crystal. With these improvements, the gigahertz oscillator could have the potential of producing sub-10 fs pulses in a convenient and cost-effective manner, due to the minimization of intracavity material that is inherent to its design. This design also eliminates the need for space-consuming prisms and experimentally demonstrates novel and heretofore unrecognized concepts about the dispersive properties of resonators. It is hoped that this will stimulate the development of other novel and compact geometries for KLM lasers. In combination with diode-pumpable materials, it is hoped that the techniques demonstrated will have a significant impact on the development of a compact and reliable femtosecond technology.

Finally, a cavity-dumped femtosecond Ti:Al_2O_3 source has also been developed and demonstrated to provide an order of magnitude increase in available pulse energies directly from an oscillator. 100 nJ pulses were achieved with pulse durations of 50 fs at variable repetition rates as high as 1 MHz. The cavity-dumped laser provides

a variable-repetition rate, intermediate-energy, simple and cost-effective source for femtosecond studies. It fills an important gap, between stand-alone oscillators and complex oscillator plus amplifier systems, in the energy spectrum of available sources. Generation of a white-light continuum [86] has already been demonstrated directly from a cavity-dumped oscillator. This constitutes a significant advance in providing simple and reliable sources that are suitable for use in nonlinear spectroscopy. Further studies into the causes of multiple-pulse formation, intracavity pulse dynamics during dumping and the scaling of mode-sizes within the resonator, may lead to the production of still higher pulse energies and peak powers using acousto-optic dumping techniques. Electro-optic dumping techniques should also be considered as an alternative.

Appendix A

This appendix details the derivation of the differential equation for dq, the change in the q parameter, upon propagation through an infinitesimal length dz, for a medium with a parabolically varying index profile ie.

$$n = n_0 \left(1 - 2r^2/h_{sf}^2\right) \tag{A.1}$$

As described in Chapter 3, a length dz of this medium possesses an ABCD matrix analagous to a GRIN lens [36] defined by

$$\begin{pmatrix} A & B \\ C & D \end{pmatrix} = \begin{pmatrix} 1 - \frac{dz^2}{2h_{sf}^2} & \frac{dz}{n_0} \\ -\frac{n_0}{h_{sf}^2}dz & 1 - \frac{dz^2}{2h_{sf}^2} \end{pmatrix} \tag{A.2}$$

Let the input to the infinitesimal distance be q and the output be q'. Let us also define:

$$q = r_1/r_2 \tag{A.3}$$

$$q' = r_1'/r_2' \tag{A.4}$$

we can write that

$$q' = \frac{Aq + B}{Cq + D} \tag{A.5}$$

$$= \frac{Ar_1 + Br_2}{Cr_2 + Dr_2} \tag{A.6}$$

$$= \frac{r_1'}{r_2'} \tag{A.7}$$

Clearly from Equation A.7 we have that

$$r_1' = Ar_1 + Br_2 \tag{A.8}$$

$$r_2' = Cr_1 + Dr_2. \tag{A.9}$$

Using the above equations, recalling that

$$dq = q' - q \tag{A.10}$$

$$dr_1 = r_1' - r_1 \tag{A.11}$$

$$dr_2 = r_2' - r_2 \tag{A.12}$$

and neglecting terms of second order in dz, we have that

$$\frac{dr_1}{dz} = \frac{r_2}{n_0} \tag{A.13}$$

and

$$\frac{dr_2}{dz} = -\frac{n_0 r_1}{h_{sf}^2} \tag{A.14}$$

Consequently we can write,

$$\frac{dq}{dz} = \frac{d}{dz}\frac{r_1}{r_2} \tag{A.15}$$

$$= \frac{1}{r_2}\frac{dr_1}{dz} - \frac{r_1}{r_2^2}\frac{dr_2}{dz} \tag{A.16}$$

$$= \frac{1}{r_2}\frac{r_2}{n_0} + \frac{r_1}{r_2^2}\left(\frac{n_0 r_1}{h_{sf}^2}\right) \tag{A.17}$$

$$= \frac{1}{n_0} + q^2\frac{n_0}{h_{sf}^2}. \tag{A.18}$$

We can also write that

$$\frac{d}{dz}(1/q) = -1/q^2\frac{dq}{dz} = -1/q^2\frac{1}{n_0} - \frac{n_0}{h_{sf}^2} \tag{A.19}$$

Substituting p = 1/q we have,

$$\frac{dp}{dz} = -\frac{p^2}{n_0} - \frac{n_0}{h_{sf}^2} \tag{A.20}$$

$$= \frac{-p_r^2 + p_i^2 - 2jp_rp_i}{n_0} - \frac{n_0}{h_{sf}^2}. \tag{A.21}$$

Taking the real and imaginary parts of the above relation we finally arrive at the coupled differential equations quoted in Chapter 3 namely,

$$\frac{dp_r}{dz} = -\frac{p_r^2}{n_0} + \frac{(\sigma p_i)^2}{n_0} \tag{A.22}$$

$$\sigma\frac{dp_i}{dz} = -\sigma p_i\frac{2p_r}{n_0} \tag{A.23}$$

$$\tag{A.24}$$

where the scaling factor σ is defined as,

$$\sigma \equiv \sqrt{1 - \frac{P}{P_{cr}}} \tag{A.25}$$

$$P_{cr} \equiv \frac{a\lambda^2}{8\pi n_0 n_2} \tag{A.26}$$

If we had carried out an identical derivation to describe linear propagation through an infintesimal distance dz of a material with index n_0 we would have got the same equations with the modification $\sigma p_i \longrightarrow p_i$. This is the basis for the description of self-focusing by a simple scaling of imaginary part of the complex parameter 1/q. Following the scaling of p_i, the mathematical treatment of linear and nonlinear propagation is identical.

Appendix B

```
\ ======================================================
\ #      ABCD Matrix Gaussian beam propagation         #
\ #                                                    #
\ ======================================================
\ ABCD.PGM
\ All distances are in centimeters
\ Wavelengths are in centimeters

\ ************************************
\ * Variable Definitions for all words *
\ ************************************
Integer
    scalar n            500 n :=          \ Number of slices - resolution
    scalar Ne           10 Ne :=          \ Number of elements in the laser
    scalar posindex      1 posindex :=    \ Running index for position in laser
    scalar nslices       1 nslices :=     \ Index for position within elements
    scalar count         0 count :=       \ Variable for counting
    scalar nbpoints      0 nbpoints :=
Real
    scalar d            1. d :=             \ Distance
    scalar k            1. k :=             \ slope
    scalar lambda       .00008 lambda :=    \ Wavelength
    scalar MA           1. MA :=            \ A
    scalar MB           0. MB :=            \ B
    scalar MC           1. MC :=            \ C
    scalar MD           1. MD :=            \ D
    scalar zeta         0 zeta :=           \ scale factor
    scalar power
    scalar Pcrit                            \ Critical power
    scalar n0           1.5 n0 :=           \ linear index
    scalar n2           .1 n2 :=            \ nonlinear index
    scalar l_one        1.0 l_one :=
    scalar l_two        1.0 l_two :=
    scalar l_three      1.0 l_three :=
    scalar incr         0.0 incr :=
    scalar start        0.0 start :=        \ initial values for plotsize
    scalar flens        0.0 flens :=
    scalar d_one        0.0 d_one :=
    scalar d_two        0.0 d_two :=
    scalar f_lens       0.0 f_lens :=
    scalar nsteps1      250.0 nsteps1 :=
    scalar nsteps2      10.0 nsteps2 :=
    scalar theta         0.0 theta :=
    scalar mirad         0.0 mirad :=
    scalar temp          0.0 temp :=
```

```
    dim[ 2 , 2 ] array Mlaser                \ Total Matrix of laser
    dim[ n ] array mode                      \ Mode radius
    dim[ n ] array position                  \ Distance in laser
    dim[ 50 ] array modesize                 \ Size of mode at a mirror
    dim[ 50 ] array xaxis                    \ length of arm
Complex
    scalar q           1. q :=           \ q parameter
    scalar q_nl_in     1. q_nl_in  :=    \ q at the input of the nl medium
    scalar q_nl_out    1. q_nl_out :=    \ q at the output of the nl medium
    scalar q_nl_diff   1. q_nl_diff :=   \ q difference between in and out
    scalar q_nl_step   1. q_nl_step :=   \ q step between in and out of the
                                         \ nl medium.
    dim[ Ne , 2 , 2 ] array laser        \ Array of matrices
    dim[ Ne , 2 , 2 ] array laserforw     \ Array of matrices - forward
    dim[ Ne 1 - , 2 , 2 ] array laserrev \ Array of matrices - reverse


\ ************************************************
\ * Definitions of Matrices for different elements *
\ ************************************************

: Freespace           \ [ d -- Mfs ]
    d :=
    complex
    Matrix[ 1. 1. z=x+iy , d ; 0. , 1. ]
;
: Flat                \ [  --  Mflat ]
    complex
    Matrix[ 1. 1. z=x+iy , 0. ; 0. , 1. ]
;

: Thinlens            \ [ f -- Mtl ]
    d :=
    complex
    Matrix[ 1. 1. z=x+iy , 0. ; -1. d / , 1. ]
;
: Material            \ [ d n0 -- Mmat ]
    n0 :=
    n0 / d :=
    complex
    Matrix[ 1. n0 z=x+iy , d ; 0. , 1. ]
;
: NL.Material            \ [ d n0 n2 -- Mmat ]
    n2 := n0 :=
    n0 / d :=
    complex
    Matrix[ 1. n0 z=x+iy , d 1. z=x+iy ; 0. , 1. n2 z=x+iy ]
;
: Mirrorsag            \ [ mirad , theta -- Mmirsag ]
    cos 2. * / d :=
    complex
    Matrix[ 1. 1. z=x+iy , 0. ; -1. d / , 1. ]
;
: Mirrortan             \ [ r, theta -- Mmirtan]
  cos * 2. / d :=
  complex
  Matrix[ 1. 1. z=x+iy , 0. ; -1 d / , 1. ]
;
```

```
: Brewsterhilo           \ [n -- Brewsterhilo]
  n0 :=
  complex
  Matrix[ 1. n0 / 1. z=x+iy , 0. ; 0. , n0 n0 * ]
;
: Brewsterlohi           \ [n -- Brewsterlohi]
  n0 :=
  complex
  Matrix[ n0 1. z=x+iy , 0. ; 0. , 1 n0 n0 * / ]
;

\ ****************************************
\ * Words to manipulate q                *
\ ****************************************

: Radius           \ [ q -- R(q) ]
    inv zreal inv
;
: Waist           \ [ q -- w(q) ]
    inv zimag abs pi * inv lambda * sqrt
;
: Bparam          \ [ q -- b(q) ]
    waist
    dup * pi * lambda /
;
: qinitial         \ [ r, w --- q]
    2 ** pi * inv lambda * neg
    swap inv swap z=x+iy inv
;
: Bil.transf      \ [ q matrix -- q' ]
    swap q :=
    dup [ 1 , 1 ] q *
    over [ 1 , 2 ] +
    swap dup [ 2 , 1 ] q *
    swap [ 2 , 2 ] +
    /
;

\ ****************************************
\ * Round trip matrix calculation        *
\ ****************************************
: Mult     \ [ M1 M2 -- M1.M2 ]
    << * | + >>
;
: Closure         \ [ M -- q ]
    dup [ 1 , 1 ] zreal MA :=
    dup [ 1 , 2 ] zreal MB :=
    dup [ 2 , 1 ] zreal MC :=
    [ 2 , 2 ] zreal MD :=
    MD MA - 2 ** MB MC * 4 * + 0 z=x+iy sqrt neg
    MA MD - +
    MC / 2 /
    dup zimag 0 = if
        cr ." Unstable cavity !!!"
    then
;
: Laserforw.matrix    \ [ M1, .... , Mn, n -- Mlaserforw]
    Ne :=
    Ne 1 + 1 do       \ Do Ne times
```

```
        Laserforw xsect[ Ne 1 + i - , ! , ! ] :=
    loop
;
: Laserrev.matrix    \ [ Mn-1, .... , M1,-- Mlaserforw]
    Ne 1 do       \ Do ( Ne - 1 ) times
        Laserrev xsect[ i , ! , ! ] :=
    loop
;

: Laserrt.matrix          \
   real matrix[ 1 , 0 ; 0 , 1 ]
   Ne 1 + 1 do        \ Do Ne times
        Laserforw xsect[ i , ! , ! ] zreal dup . mult
   loop
   Ne 1 do            \ Do (Ne - 1) times
        Laserrev xsect[ Ne i - , ! , ! ] zreal dup . mult
   loop
   0. z=x+iy
;

: Laser.matrix     \ [ M1 , ... , Mn , n -- Mlaser ]
    Ne :=
    Ne 1 + 1 do
        Laser xsect[ Ne 1 + i - , ! , ! ]  :=
    loop
    real matrix[ 1 , 0 ; 0 , 1 ]
    Ne 1 + 1 do
        Laser xsect[ i , ! , ! ]  zreal mult
    loop
    Ne 2 do
        Laser xsect[ Ne 1 + i - , ! , ! ] zreal mult
    loop
    0. z=x+iy
;
: Pcritical                           \ [ lambda , n0 , n2 ---- pcrit ]
    * 8 * pi * inv swap 2 ** * 5.35 * \ the fudge factor a = 5.35
;
\ ***********************************
\ * Words for Nonlinear propagation  *
\ ***********************************
: Enter.nonlinear                  \ [qinput, power, pcrit  -- scaled q]
     / neg 1 + sqrt zeta :=
     zeta swap inv swap
     over zimag * swap zreal swap z=x+iy inv
;
: Exit.nonlinear                  \ [ qinput -- scaled q]
     zeta inv
     swap inv swap
     over zimag * swap zreal swap z=x+iy inv
;
: Propagate.nonlinearly     \ [ linearmatrix, qinput, power, pcrit ]
                            \ [ ---- qoutput ]
    Enter.nonlinear
    swap
    Bil.transf
    Exit.nonlinear
;
: Plot.bulk         \ [ qinput, length, n - mode[]]
    n0 :=
    1_one :=
    dup
```

```
    0 l_one position []fill
    position n0 / + waist
    mode :=
;
: Plot.bulk.nl      \ [ qinput, length, n, power, pcrit -- mode []]
   pcrit :=
   power :=
   n0 :=
   l_one :=
   dup
   0 l_one position []fill
   n 1 + 1 do
     power pcrit enter.nonlinear
     position [ 2 ] n0 / +
     exit.nonlinear
     dup waist mode [ i ] :=
   loop
;
\*************************************
\         Far field divergence         *
\*************************************
: ffdiv  \ [ qinput, n, power, pcrit, l_one, l_two, l_three -  mode[]]
    l_three :=
    l_two :=
    l_one :=
    pcrit :=
    power :=
    n0 :=
    0 l_one l_two + l_three + position []fill
    1 posindex :=
    l_one position [ 2 ]  / 1 + 1 do
        position [ 2 ] +
        dup waist mode [ posindex ] :=
        posindex 1 + posindex :=
        loop
    power pcrit enter.nonlinear
    l_two position [ 2 ] / 1 + 1 do
        position [ 2 ] n0 / +
        dup waist mode [ posindex ] :=
        posindex 1 + posindex :=
        loop
    exit.nonlinear
    l_three position [ 2 ] / 1 + 1 do
       position [ 2 ] +
        dup waist mode [ posindex ] :=
        posindex 1 + posindex :=
        loop
;
\ ****************************************
\ * Words to plot beam in cavity starting  *
\ * with calculated self-consistent q      *
\ ****************************************
: Plot.beam.forward     \  [ q1 -- q2 ]
    1 posindex :=
    0.
    Ne 1 + 1 do                          \ Total length of laser
        Laser [ i , 1 , 2 ] zreal Laser [ i , 1 , 1 ] zimag * +
    loop
    0. swap position []fill              \ Autoscale pos. array
```

```
    Ne 1 + 1 do
        Laser [ i , 1 , 1 ] zimag n0 :=      \ Linear index
        Laser [ i , 1 , 2 ] zreal 0. = if    \ Thin element ?
            Laser xsect[ i , ! , ! ] zreal Bil.transf
        else
            Laser [ i , 1 , 2 ] zimag 0. = if   \ Linear element
                Laser [ i , 1 , 2 ] zreal n0 *  \ "Real" length
                position [ 2 ] / dup 1 modulo - 1 + nslices :=
                                        \ Assign slices to element
                nslices ramp 1 - position [ 2 ] * n0 / over +
                                                \ Propagate through slices
                waist
                mode sub[ posindex , nslices ] :=  \ Move to next elt
                posindex nslices + 1 - posindex :=
                Laser xsect[ i , ! , ! ] zreal Bil.transf
\ q at end of element
            else
                Power
                lambda
                Laser [ i , 1 , 1 ] zimag
                Laser [ i , 2 , 2 ] zimag
                Pcritical dup Pcrit :=
                enter.nonlinear
                Laser [ i , 1 , 2 ] zreal n0 *
                position [ 2 ] / dup 1 modulo - 1 + nslices :=
                nslices ramp 1 - position [ 2 ] * n0 / over +
                waist zeta sqrt *
                mode sub[ posindex , nslices ] :=
\ Move to next elt
                posindex nslices + 1 - posindex :=
                Laser xsect[ i , ! , ! ] zreal Bil.transf
                exit.nonlinear
            then
        then
    loop
;
: Plot.beam.reverse                     \  [ q1 -- q2 ]
    n posindex :=
    0.
    Ne 1 + 1 do                          \ Total length of laser
        Laser [ i , 1 , 2 ] zreal Laser [ i , 1 , 1 ] zimag * +
    loop
    0. swap position []fill              \ Autoscale pos. array
    Ne 1 + 1 do                          \ Localized element ?
        Ne i - 1 + count :=
        Laser [ count , 1 , 1 ] zimag n0 :=
        Laser [ count , 1 , 2 ] zreal 0. = if     \ Thin element ?
            Laser xsect[ count , ! , ! ] zreal Bil.transf
        else
            Laser [ count , 1 , 2 ] zimag 0. = if  \ Linear element ?
                Laser [ count , 1 , 2 ] zreal n0 *
                position [ 2 ] / dup 1 modulo - 1 + nslices :=
                nslices ramp 1 - position [ 2 ] * n0 / over +
                waist  rev[ 1 ]
                mode sub[ posindex nslices - 1 + , nslices ] :=
                                                \ Move to next elt
                posindex nslices - posindex :=
                Laser xsect[ count , ! , ! ] zreal Bil.transf
            else
                Power
                lambda
                Laser [ count , 1 , 1 ] zimag
```

```
                Laser [ count , 2 , 2 ] zimag
                Pcritical dup Pcrit :=
                enter.nonlinear
                Laser [ count , 1 , 2 ] zreal n0 *
                position [ 2 ] / dup 1 modulo - 1 + nslices :=
                nslices ramp 1 - position [ 2 ] * n0 / over +
                waist zeta sqrt * rev[ 1 ]
                mode sub[ posindex nslices - 1 + , nslices ] :=
                                                  \ Move to next elt
                posindex nslices - posindex :=
                Laser xsect[ count , ! , ! ] zreal Bil.transf
                exit.nonlinear
            then
        then
    loop
;

\ ************************************
\ * Words to compute q on a roundtrip  *
\ * without plotting anything          *
\ ************************************
: compute.forward     \  [ q1 -- q2 ]
    1 posindex :=
    0.
    Ne 1 + 1 do                         \ Total length of laser
        Laser [ i , 1 , 2 ] zreal Laser [ i , 1 , 1 ] zimag * +
    loop
    0. swap position []fill             \ Autoscale pos. array
    Ne 1 + 1 do                         \ Localized element ?
        Laser [ i , 1 , 1 ] zimag n0 :=
        Laser [ i , 1 , 2 ] zreal 0. = if   \ Thin element ?
            Laser xsect[ i , ! , ! ] zreal Bil.transf
        else
            Laser [ i , 1 , 2 ] zimag 0. = if  \ Linear element
                Laser xsect[ i , ! , ! ] zreal Bil.transf
            else
                Power
                lambda
                Laser [ i , 1 , 1 ] zimag
                Laser [ i , 2 , 2 ] zimag
                Pcritical dup Pcrit :=
                enter.nonlinear
                Laser xsect[ i , ! , ! ] zreal Bil.transf
                exit.nonlinear
            then
        then
    loop
;
: compute.reverse                       \  [ q1 -- q2 ]
    n posindex :=
    0.
    Ne 1 + 1 do                         \ Total length of laser
        Laser [ i , 1 , 2 ] zreal Laser [ i , 1 , 1 ] zimag * +
    loop
    0. swap position []fill              \ Autoscale pos. array
    Ne 1 + 1 do                          \ Localized element ?
        Ne i - 1 + count :=
\        ." element # " count . cr
        Laser [ count , 1 , 1 ] zimag n0 :=
        Laser [ count , 1 , 2 ] zreal 0. = if      \ Thin element ?
            Laser xsect[ count , ! , ! ] zreal Bil.transf
        else
```

```
            Laser [ count , 1 , 2 ] zimag 0. = if  \ Linear element ?
                Laser xsect[ count , ! , ! ] zreal Bil.transf
            else
                Power
                lambda
                Laser [ count , 1 , 1 ] zimag
                Laser [ count , 2 , 2 ] zimag
                Pcritical dup Pcrit :=
                enter.nonlinear
                Laser xsect[ count , ! , ! ] zreal Bil.transf
                exit.nonlinear
            then
        then
    loop
;
: Display.mode
    mode r1 :=
    mode neg r2 :=
    position x :=
    r1 [ n 2 - ] dup r1 [ n 1 - ] := r1 [ n ] :=
    r2 [ n 2 - ] dup r2 [ n 1 - ] := r2 [ n ] :=
;
\ *********************************
\ * Words for nonlinear iteration *
\ *********************************
: nl.plot    \ [ q_nl_in -- q_nl_out ]
    dup q_nl_in :=
    plot.beam.forward
    display.mode
    r1 [ n 2 - ] dup r1 [ n 1 - ] := r1 [ n ] :=
    r2 [ n 2 - ] dup r2 [ n 1 - ] := r2 [ n ] :=
    r3 [ n 2 - ] dup r3 [ n 1 - ] := r3 [ n ] :=
    r4 [ n 2 - ] dup r4 [ n 1 - ] := r4 [ n ] :=
;
: nl.smart     \ [ q_nl_in number -- q_nl_out ]
    swap q_nl_in :=
    1 + 1 do
        q_nl_in
        compute.forward
        compute.reverse
        q_nl_out :=
        q_nl_in q_nl_out - zmag cr ." Error: " .
        q_nl_out inv zimag z=0+iy inv q_nl_in :=
    loop
    q_nl_in nl.plot
;

\ ***************************************
\ * Words to simulate particular cavitiy *
\ * configurations                       *
\ ***************************************
\ Simple lens cavity with xtal
: test                      \  [ flens, l_one, l_two --- ]
    l_two :=
    l_one :=
    flens :=
    0 power :=
    flat
    .3 1.76 3.e-16 nl.material
    l_one .3 1.76 / - freespace
    flens thinlens
```

```
    l_two freespace
    flat
    6 laser.matrix
    closure
    dup q_nl_in :=
    plot.beam.forward
    display.mode
    r1 r3 :=
    r2 r4 :=
;

\ Simple lens cavity without xtal
: lineartest                    \  [ flens, l_one, l_two --- ]
    l_two :=
    l_one :=
    flens :=
    0. power :=
    flat
    l_one freespace
    flens thinlens
    l_two freespace
    flat
    5 laser.matrix
    closure
    dup q_nl_in :=
    plot.beam.forward
    plot.beam.reverse
    q_nl_out :=
;
\ Garden variety four mirror x cavity
: garden                          \ [ l_one, l_two, d_one, d_two ]
    d_two :=
    d_one :=
    l_two :=
    l_one :=
    0 power :=
    flat l_one freespace 5 thinlens
    d_one freespace
    2.1 1.76 3.e-16 nl.material
    d_two freespace
    5 thinlens l_two freespace flat
    9 laser.matrix
    closure
    dup q_nl_in :=
    plot.beam.forward
    display.mode
    r1 r3 := r2 r4 :=
    plot.beam.reverse
    q_nl_out :=
    display.mode
    r1 [ n 2 - ] dup r1 [ n 1 - ] := r1 [ n ] :=
    r2 [ n 2 - ] dup r2 [ n 1 - ] := r2 [ n ] :=
    r3 [ n 2 - ] dup r3 [ n 1 - ] := r3 [ n ] :=
    r4 [ n 2 - ] dup r4 [ n 1 - ] := r4 [ n ] :=
;
```

Appendix C

This appendix provides details of a part of the derivation of dispersion for the compact laser geometry demonstrated in Chapter 5. Figure 5-12 is reproduced here for convenience. In this figure the central wavelength for which the prism is cut has been assumed. It was shown in chapter 5 that $P_1(\lambda)$, one component of the wavelength dependent optical path length $P(\lambda)$ through the cavity was given as a function of the angle $\theta(\lambda)$, defined in the above figure, as

$$P_1(\theta) = X sin\theta(\lambda) + Y sin\theta(\lambda) \tag{C.1}$$

We want to derive a convenient expression for

$$\frac{dP_1}{d\theta} = X cos\theta(\lambda) - Y sin\theta(\lambda) \tag{C.2}$$

Referring to Figure C-1, notice first that for any wavelength,

$$\begin{aligned} ZR &= ZQ cos\theta(\lambda) && \text{(C.3)} \\ &= (X - Y tan\theta(\lambda)) cos\theta(\lambda) && \text{(C.4)} \\ &= X cos\theta(\lambda) - Y sin\theta(\lambda) && \text{(C.5)} \\ &= \frac{dP_1}{d\theta} && \text{(C.6)} \end{aligned}$$

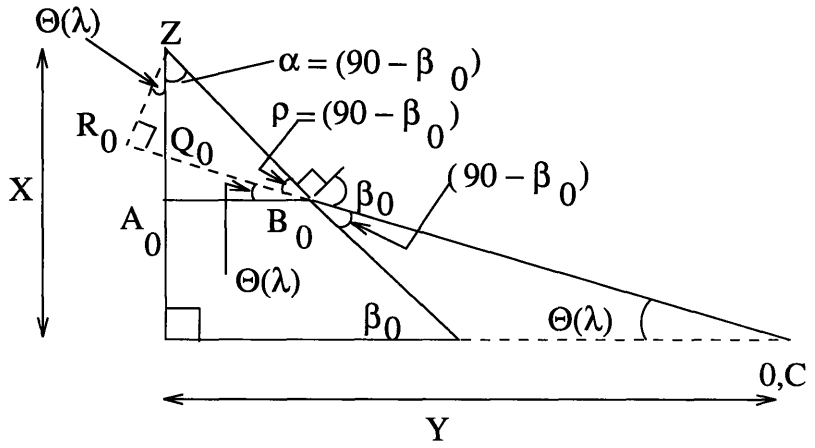

Figure C-1: Detailed geometry for calculation of path length in one part of unfolded cavity of Figure 5-11.

Further, for the central wavelength, λ_0 at which the crystal is assumed we are attempting to show that

$$ZR_0 = A_0B_0 \tag{C.7}$$

To see this notice that since both,

$$\alpha = 90 - \beta_0 \tag{C.8}$$

and

$$\rho = 90 - \beta_0 \tag{C.9}$$

the two lengths ZQ_0 and Q_0B_0 are equal. Now, examining the triangles ZQ_0R_0 and $Q_0A_0B_0$, we find that they are clearly congruent, which proves that

$$ZR_0 = A_0B_0 \tag{C.10}$$

Bibliography

[1] S. A. Akhmanov, R. V. Khokhlov, and A. P. Sukhurukov. *Laser Handbook*, chapter E3, page 1150. North-Holland, Amsterdam, 3rd edition, 1972.

[2] G. F. Albrecht, M. M. Eggleston, and J. J. Ewing. Measurements of $Ti^{3+}Al_2O_3$ as a lasing material. *Optics Communications*, 52:401–404, 1985.

[3] M. T. Asaki, C. P. Huang, D. Garvey, J. Zhou, H. C. Kapteyn, and M. M. Murnane. Generation of 11 fs pulses from a self-mode-locked Ti:sapphire laser. *Optics Letters*, 17:977–79, 1993.

[4] Norman P. Barnes and Donald J. Gettemy. Temperature variation of the refractive indices of Yttrium Lithium Fluoride. *Journal of the Optical Society of America, B.*, 70:1244, 1980.

[5] B. E. Lemoff and C. P. J. Barty. Generation of high-peak-power 20-fs pulses from a regeneratively initiated, self-mode-locked Ti:sapphire laser. *Optics Letters*, 17:1367–69, 1992.

[6] B. E. Lemoff and C. P. J. Barty. Cubic-phase-free dispersion compensation in solid-state ultrashort-pulse lasers. *Optics Letters*, 18:57–59, 1993.

[7] C. P. J. Barty, B. E. Lemoff, and C. L. Gordon III. Compact, multiterawatt laser systems: an ultrashort pulse approach. In *Proceedings of the Conference on Lasers and Electro-Optics*. OSA Technical Digest Series, May 1994.

[8] Pierre-A. Belanger and Claude Pare. Self-focussing of Gaussian beams: an alternate derivation. *Applied Optics*, 22:1293–95, 1982.

[9] K. Bergman, H. A. Haus, E. P. Ippen, and M. Shirasaki. Squeezing in a fiber interferometer with a Gigahertz pump. *Optics Letters*, 19:290–92, 1994.

[10] C. Le Blanc, G. Grillon, J. P. Chambaret, A. Migus, and A. Antonetti. Compact and efficient multipass Ti:sapphire system for femtosecond chirped-pulse amplification at the terawatt level. *Optics Letters*, 18:140–42, 1993.

[11] K. J. Blow and D. Wood. Mode-locked lasers with nonlinear external cavities. *Journal of the Optical Society of America B*, 5:629, 1988.

[12] T. Brabec, P. F. Curley, Ch. Spielmann, E. Wintner, and A. J. Schmidt. Hard-aperture Kerr-lens mode locking. *Journal of the Optical Society of America B*, 10:1029–1034, 1993.

[13] A. G. Bulushev, E. M Dianov, and O. G. Okhotnikov. Self-starting mode-locked laser with a nonlinear ring resonator. *Optics Letters*, 16:88–90, 1991.

[14] L. Dahlstrom. Passive mode locking and Q-switching of high-power lasers with the optical Kerr effect modulator. *Optics Communications*, 5:157, 1972.

[15] A. J. DeMaria, D. A. Stetser, and H. Heynau. Self mode-locking of lasers with saturable absorbers. *Applied Physics Letters*, 8:174, 1966.

[16] M. DiDomenico, H. M. Marcos, J. E. Geusic, and R. E. Smith. Generation of ultrashort optical pulses by mode locking the YAG:Nd laser. *Applied Physics Letters*, 8:180, 1966.

[17] W. Dietel, J. J. Fontaine, and J. C. Diels. Intracavity pulse compression with glass: a new method of generating pulses shorter than 60 fs. *Optics Letters*, 8:4–6, 1983.

[18] I. N. Duling, T. Norris, T. Sizer, P. Bado, and G. Mourou. Kilohertz synchronous amplification of 85 fs optical pulses. *Journal of the Optical Society of America*, B2:616, 1985.

[19] J. M. Evans, D. E. Spence, W. Sibbett, B. H. T. Chai, and a. Miller. 50 fs pulse generation from a self-mode-locked Cr^{3+}:$LiSrAlF_6$ laser. *Optics Letters*, 17:1447–49, 1992.

[20] J. J. Fontaine, W. Dietel, and J. C. Diels. Chirp in a mode-locked ring dye laser. *IEEE Journal of Quantum Electronics*, 19:1467–69, 1983.

[21] R. L. Fork, C. H. Brito Cruz, P.C. Becker, and C. V. Shank. Compression of optical pulses to six femtoseconds by using cubic phase compensation. *Optics Letters*, 12:483–85, 1987.

[22] R. L. Fork, B. I. Greene, and C. V. Shank. Colliding pulse modelocked laser. *Applied Physics Letters*, 38:671, 1981.

[23] R. L. Fork, O. E. Martinez, and J. P. Gordon. Negative dispersion using pairs of prisms. *Optics Letters*, 9:150–52, 1984.

[24] R. L. Fork, C. V. Shank, and R. Yen. Amplification of 70 fs optical pulses to gigawatt powers. *Applied Physics Letters*, 41:223, 1982.

[25] R. L. Fork, C.V. Shank, C. Hirlimann, and R. Yen. Femtosecond white-light continuum pulses. *Optics Letters*, 8, 1983.

[26] G. Gabetta, D. Huang, J. Jacobson, M. Ramaswamy, and J. G. Fujimoto. Femtosecond pulse generation in Ti:sapphire using a Microdot mirror mode locker. *Optics Letters*, 16:1756–58, 1991.

[27] G. Gabetta, D. Huang, J. Jacobson, M. Ramaswamy, H. A. Haus, E. P. Ippen, and J. G. Fujimoto. Femtosecond pulse generation in Ti:Al_2O_3 using nonlinear

intracavity elements. In *Proceedings of the Conference on Lasers and Electro-Optics*. OSA Technical Digest Series, May 1991.

[28] D. Georgiev, J. Herrmann, and U. Stamm. Cavity design for optimum nonlinear absorption in Kerr-lens mode-locked solid-state lasers. *Optics Communications*, 5:368–375, 1992.

[29] J. Goodberlet, J. Jacobson, J. Wang, J. G. Fujimoto, and T. Y. Fan. Ultrashort pulse generation with Additive Pulse Modelocking in solid-state lasers. In C. B. Harris, E. P. Ippen, G. A. Mourou, and A. Zewail, editors, *Ultrafast Phenomena VII*, 1990.

[30] J. Goodberlet, J. Wang, J. G. Fujimoto, and P. A. Schulz. Femtosecond passively modelocked Ti:Al_2O_3 laser with a nonlinear external cavity. *Optics Letters*, 14:1125–27, 1989.

[31] J. P. Gordon and R. L. Fork. Optical resonator with negative dispersion. *Optics Letters*, 9:153–55, 1984.

[32] L. E. Hargrove, R. L. Fork, and M. A. Pollack. Locking of He-Ne laser modes induced by synchronous intracavity modulation. *Applied Physics Letters*, 5:4, 1964.

[33] H. A. Haus and E. P. Ippen. Self-starting of passively mode-locked lasers. *Optics Letters*, 16:1331, 1991.

[34] H. A. Haus, E. P. Ippen, and J. G. Fujimoto. Structures for Additive pulse modelocking. *Journal of the Optical Society of America B*, 16:1502–04, 1991.

[35] H. A. Haus, E. P. Ippen, and J. G. Fujimoto. Analytic theory of Kerr lens modelocking. *Journal of the Optical Society of America B*, 28:2086–2096, 1992.

[36] Hermann A. Haus. *Waves and Fields in Optoelectronics*. Prentice-Hall Inc., Englewood Cliffs, NJ, 1st edition, 1984.

[37] M. Hofer, M. E. Fermann, F. Haberl, and M. H. Ober. Modelocking with cross-phase and self-phase modulation. *Optics Letters*, 16:502–504, 1991.

[38] C. P. Huang, M. T. Asaki, S. Backus, M. M. Murnane, H. C. Kapteyn, and H. Nathel. Generation of 17 fs pulses from a self-mode-locked Ti:sapphire laser. *Optics Letters*, 17:1289–91, 1992.

[39] C. P. Huang, H. C. Kapteyn, J. W. McIntosh, and M. M. Murnane. Generation of transform limiited 32 fs pulses from a self-mode-locked Ti:sapphire laser. *Optics Letters*, 17:2139–41, 1992.

[40] David Huang, Morrison Ulman, Lucio H. Acioli, Hermann A. Haus, and James G. Fujimoto. Self-focusing-induced saturable loss for laser mode locking. *Optics Letters*, 17:511–13, 1992.

[41] I. N. Duling III. All-fiber ring soliton laser mode locked with a non-linear mirror. *Optics Letters*, 16:539, 1991.

[42] E. P. Ippen. Principles of passive modelocking. *Applied Physics B*, 58:159–170, 1994.

[43] E. P. Ippen, H. A. Haus, and L. Y. Liu. Additive pulse mode locking. *Journal of the Optical Society of America B*, 6:1736, 1989.

[44] E. P. Ippen and C. V. Shank. Subpicosecond spectroscopy. *Picosecond Phenomena*, 41:223, 1982.

[45] E. P. Ippen, C. V. Shank, and A. Dienes. Passive modelocking of the CW dye laser. *Applied Physics Letters*, 21:348, 1972.

[46] J. M. Jacobson, K. Naganuma, H. A. Haus, and J. G. Fujimoto. Femtosecond pulse generation in a Ti:Al_2O_3 laser by using second and third-order intracavity dispersion. *Optics Letters*, 17:1608–10, 1992.

[47] James D. Kafka, Michael L. Watts, and Jan-Willem Pieterse. Picosecond and femtosecond pulse generation in a regeneratively modelocked Ti:sapphire laser. *IEEE Journal of Quantum electronics*, QE-28:2151–2162, 1992.

[48] W. Kaiser, editor. *Topics in Applied Physics: Ultrashort Laser Pulses.* Springer-Verlag, 1988.

[49] U. Keller, W. H. Knox, and H. Roskos. Coupled-cavity Resonant Passive Mode-locked Ti:sapphire laser. *Optics Letters*, 15:1377–79, 1990.

[50] U. Keller, K. D. Li, B. T. Khuri-Yakub, and D. M. Bloom. High-frequency acousto-optic mode locer for picosecond pulse generation. *Optics Letters*, 15:45–47, 1990.

[51] U. Keller, G. W. tHooft, W. H. Knox, and J. E. Cunningham. Femtosecond pulses from a continuously self-starting passively mode-locked Ti:sapphire laser. *Optics Letters*, 16:1022, 1991.

[52] U. Keller, T. K . Woodward, D. L. Sivco, and A. Y. Cho. Coupled-cavity resonant passive mode-locked Nd:Yttrium Lithium Flouride laser. *Optics Letters*, 16:390, 1991.

[53] E. L. Kerr. Self-focusing in the aberrationless limit. *Physical Review A*, 4:1195, 1971.

[54] W. H. Knox. Generation and kilohertz-rate amplification of femtosecond optical pulses around 800 nm. *Journal of the Optical Society of America. B*, 4:1771–1776, 1987.

[55] W. H. Knox. Femtosecond optical pulse amplification. *IEEE Journal of Quantum Electronics*, 24:388–397, 1988.

[56] W. H. Knox, M. C. Downer, R. L. Fork, and C. V. Shank. Amplification of femtosecond optical pulses and continuum generation at a 5 kHz repetition rate. *Optics Letters*, 9:552–54, 1984.

[57] Walter Koechner. *Solid-State Laser Engineering.* Springer Verlag, Berlin, Heidelberg, 2nd edition, 1988.

[58] A. G. Kostenbauder. Ray-pulse matrices: A rational treatment for dispersive optical systems. *IEEE Journal of Quantum Electronics*, 26:1148–57, 1990.

[59] P. Lacovara, L. Esterowitz, and R. Allen. Flash-lamp pumped Ti:Al_2O_3 laser using flourescent conversion. *Optics Letters*, 10:273–275, 1985.

[60] E. G. Lariontsev and V. N. Serkin. Possibility of using self-focusing for increasing contrast and narrowing of ultrashort light pulses. *Soviet Journal of Quantum Electronics*, 5:796–800, 1975.

[61] P. LiKamWa, B. H. T. Chai, and A. Miller. Self-mode-locked Cr^{3+}:$LiCaAlF_6$ laser. *Optics Letters*, 17:1438–40, 1992.

[62] J. M. Liu and J. K. Chee. Passive modelocking of a CW Nd:YLF laser with a nonlinear external cavity. *Optics Letters*, 15:685, 1990.

[63] K. X. Liu, C. J. Flood, D. R. Walker, and H. H. van Driel. Kerr lens mode locking of a diode-pumped nd:yag laser. *Optics Letters*, 17:1361–63, 1992.

[64] L.Y. Liu, J. M. Huxley, E. P. Ippen, and H. A. Haus. Self-starting Additive Pulse Modelocking of a Nd:YAG laser. *Optics Letters*, 15:553, 1990.

[65] Vittorio Magni, Giulio Cerullo, and Sandro De Silvestri. ABCD matrix analysis of propagation of gaussian beams through Kerr media. *Optics Communications*, 96:348–355, 1993.

[66] Vittorio Magni, Giulio Cerullo, and Sandro De Silvestri. Closed form Gaussian beam analysis of resonators containing a Kerr medium for femtosecond lasers. *Optics Communications*, 101:365–370, 1993.

[67] T. H. Maiman. Optical Maser action in ruby. *British Communication of Electronics*, 7:674, 1960.

[68] G. P. A. Malcolm and A. I. Ferguson. Self-mode-locking of a diode-pumped Nd:YLF laser. *Optics Letters*, 16:1967–69, 1991.

[69] O. E. Martinez, R. L. Fork, and J. P. Gordon. *Journal of the Optical Society of America B*, 9:156, 1984.

[70] O. E. Martinez, R. L. Fork, and J. P. Gordon. Theory of passively mode-locked lasers for the case of a nonlinear complex-propagation constant. *Journal of the Optical Society of America B*, 2:753, 1985.

[71] Oscar Eduardo Martinez. Matrix formalism for pulse compressors. *IEEE Journal of Quantum Electronics*, 24:2530–36, 1988.

[72] Oscar Eduardo Martinez. Matrix formalism for dispersive cavities. *IEEE Journal of Quantum Electronics*, 25:296–299, 1989.

[73] R. Mellish, P. M. W. French, and J. R. Taylor. All-solid-state diode-pumped c.w. femtosecond Cr:LiSrAlF$_6$ laser. In *Proceedings of the Ultrafast Phenomena Topical Meeting*. OSA Technical Digest Series, May 1994.

[74] M. Mocker and R. Collins. Mode competition and self-locking effects in a Q-switched ruby laser. *Applied Physics Letters*, 7:270, 1965.

[75] L. F. Mollenauer and R. H. Stolen. The soliton laser. *Optics Letters*, 9:13–15, 1984.

[76] P. F. Moulton. Spectroscopic and laser characteristics of Ti:Al_2O_3. *Journal of the Optical Society of America B*, 52:125–133, 1986.

[77] T. B. Norris. Femtosecond pulse amplification at 250 kHz with a ti:sapphire regenerative amplifier and application to continuum generation. *Optics Letters*, 17:1009–11, 1992.

[78] G. R. Olbright and G.R. Hadley. Generation of tunable near-infrared amplified femtosecond laser pulses and time-correlated white-light continuum. *Journal of the Optical Society of America. B*, 6:1363–1369, 1987.

[79] F. Ouellette and M. Piche. Pulse shaping and passive mode locking with a nonlinear Michelson interferometer. *Optics Communications*, 60:99, 1986.

[80] A. Owyoung, R. W. Hellwarth, and N. George. *Phys. Rev. B*, 5:628, 1972.

[81] W. S. Pelouch, P. E. Powers, and C. L. Tang. Self-starting mode-locked ring-cavity Ti:sapphire laser. *Optics Letters*, 17:1581–83, 1992.

[82] O. G. Peterson, S. A. Tuccio, and B. B. Snavely. CW operation of an organic dye solution laser. *Applied Physics Letters*, 17:245, 1970.

[83] M. Piche. Beam reshaping and self-mode-locking in nonlinear resonators. *Optics Communications*, 86:156, 1991.

[84] M. Piche, N. McCarthy, and F. Salin. In *Digest of Annual Meeting of the Optical Society of America.* OSA Technical Digest Series, 1990.

[85] Bob Proctor and Frank Wise. Quartz prism sequence for reduction of cubic phase in a modelocked Ti:Al_2O_3 laser. *Optics Letters*, 17:1295–97, 1992.

[86] Maxim S. Pshenichnikov, Wim P. de Boeij, and Douwe A. Wiersma. Generation of 13-fs, 5 MW pulses from a cavity-dumped Ti:sapphire laser. *Optics Letters*, 19:572–74, 1994.

[87] M. Ramaswamy, A. S. Gouveia-Neto, D. K. Negus, J. A. Izatt, and J. G. Fujimoto. 2.3 ps pulses from a Kerr-lens modelocked, lamp-pumped Nd:YLF laser using a microdot mirror. *Optics Letters*, 18:1825–27, 1993.

[88] M. Ramaswamy, M. Ulman, J. Paye, and J. G. Fujimoto. Femtosecond cavity dumped Kerr Lens Modelocked Ti:sapphire laser. *Optics Letters*, 18:1822–24, 1993.

[89] M. Ramaswamy-Paye and J. G. Fujimoto. Compact, dispersion-compensated geometry for kerr lens modelocked lasers. In *Proceedings of the Conference on Lasers and Electr-Optics*. OSA Technical Digest Series, May 1994.

[90] M. Ramaswamy-Paye and J. G. Fujimoto. Compact, Dispersion-compensated geometry for Kerr Lens Modelocked lasers. *Optics Letters*, page Accepted for publication, 94.

[91] K. Sala, M. C. Richardson, and N. R. Isenor. Passive mode locking of lasers with the optical Kerr effect modulator. *IEEE Journal of Quantum Electronics*, QE-13:915, 1977.

[92] Francois Salin, Jeff Squier, and Gerard Mourou. Multikilohertz Ti:Al_2O_3 amplifier for high-power femtosecond pulses. *Optics Letters*, 16:1964–66, 1991.

[93] Francois Salin, Jeff Squier, and Michel Piche. Mode locking of Ti:Al_2O_3 lasers and self-focusing: a Gaussian approximation. *Optics Letters*, 16:1674–76, 1991.

[94] N. Sarukura, Y. Ishida, and H. Nakano. Compression of intracavity chirped pulses from a CW passive mode-locked Ti:sapphire laser. *Optics Communications*, 77:49, 1990.

[95] N. Sarukura, Y. Ishida, H. Nakano, and Y. Yamamoto. CW passive mode-locking of a Ti:sapphire laser. *Applied Physics Letters*, 56:814, 1990.

[96] N. Sarukura, Y. Ishida, H. Nakano, and T. Yanagawa. All solid-state CW passively mode-locked Ti:sapphire laser using a colored glass filter. *Applied Physics Letters*, 57:229, 1990.

[97] P. A. Schulz and S. R. Henion. 5 GHz mode locking of a Nd:YLF laser. *Optics Letters*, 16:1502–04, 1991.

[98] Alphan Sennaroglu, Clifford R. Pollack, and Howard Nathel. Generation of 48-fs pulses and measurement of crystal dispersion by using a regeneratively initiated self-mode-locked Chromium-doped Forsterite laser. *Optics Letters*, 18:826–28, 1993.

[99] Alphan Sennaroglu, Clifford R. Pollock, and Howard Nathel. Continuous-wave self-mode-locked operation of a femtosecond Cr^{4+}:YAG laser. *Optics Letters*, 18:390–92, 1993.

[100] C. V. Shank and E. P. Ippen. Subpicosecond dye laser. *Applied Physics Letters*, 24:373, 1974.

[101] M. Sheik-Bahae, A. A. Said, D. J. Hagan, M. J. Soileau, and W. W. Van Stryland. Self-focusing distributed lens model. *Optical Engineering*, 30:1228, 1991.

[102] B. K. Shevastyanov. Tunable laser based on $Al_2O_3Ti^{3+}$ crystal. *Soviet Physics of Crystallography*, 29:566–567, 1984.

[103] Anthony Siegman. *Lasers.* University Science Books, Mill Valley, California, 1986.

[104] D. E. Spence and P. N. Kean and W. Sibbett. 60-fsec pulse generation from a self-mode-locked Ti:sapphire laser. *Optics Letters*, 16:42–44, 1991.

[105] Ch. Spielmann, P. F. Curley, T. Brabec, E. Wintner, A. J. Schmidt, and F. Krausz. Design considerations for femtosecond Ti:sapphire oscillators. *Electron Letters*, 28:1532–34, 1992.

[106] Ch. Spielmann, M. Lenzner, P. F. Curley, E. Wintner, and F. Krausz. Amplification of sub-20-fs pulses at kHz repetition rates. In *Proceedings of the Conference on Lasers and Electro-Optics.* OSA Technical Digest Series, May 1994.

[107] L. Spinelli, B. Couillaud, N. Goldblatt, and D. K. Negus. Starting and generation of sub-100 fs pulses in Ti:Al_2O_3 by self-focusing. In *Digest of Conference on Lasers and Electro-optics.* OSA Technical Digest Series, May 1991.

[108] Jeff Squier, Francois Salin, Gerard Mourou, and Donald Harter. 100-fs pulse generation and amplification in Ti:Al_2O_3. *Optics Letters*, 16:324–26, 1991.

[109] A. Stingl, Ch. Spielmann, F. Krausz, and R. Szipocs. Generation of 11 fs pulses from a Ti:sapphire laser without the use of prisms. *Optics Letters*, 19:204–06, 1994.

[110] D. Strickland and G. Mourou. Compression of amplified chirped optical pulses. *Optics Communications*, 56:219–221, 1985.

[111] Orazio Svelto. *Principles of Lasers.* Plenum Press, New York, 3rd edition, 1989.

[112] Robert Szipocs, Karpat Ferencz, Christian Spielmann, and Ferenc Krausz. Chirped multilayer coatings for broadband dispersion control in femtosecond lasers. *Optics Letters*, 19:201–03, 1994.

[113] K. Tamura, J. Jacobson, E. P. Ippen, H. A. Haus, and J. G. Fujimoto. Unidirectional ring resonators for self-starting passively mode-locked lasers. *Optics Letters*, 18:220–22, 1993.

[114] An-Chun Tien, Railing Chang, and Jyhpyng Wang. Adjustable negative group-velocity dispersion in graded-index lenses. *Optics Letters*, 17:1177–79, 1992.

[115] E. B. Treacy. Use of grating pairs for dispersion compensation. *IEEE Journal of Quantum Electronics*, QE-5:454, 1969.

[116] G. Vaillancourt, T. B. Norris, J. S. Coe, P. Bado, and G. A. Mourou. Operation of 1 kHz pulse-pumped Ti:sapphire regenerative amplifier. *Optics Letters*, 15:317–19, 1990.

[117] J. A. Valdmanis, R. L. Fork, and J. P. Gordon. Generation of optical pulses as short as 27 fs directly from a laser balancing self-phase-modulation, group-velocity-dispersion, saturable-absorbtion and saturable-gain. *Optics Letters*, 10:131–33, 1985.

[118] Susan J. Walker, Hercules Avramopoulos, and Theodore Sizer II. Compact mode-locked solid-state lasers at 0.5 and 1 GHz repetition rates. *Optics Letters*, 15:1070–72, 1990.

[119] C. P. Yakymyshyn, J. E. Pinto, and C. R. Pollock. Additive pulse modelocked NaCl:OH^- laser. *Optics Letters*, 14:621, 1989.

[120] J. Zhou, G. Taft, C. Shi, H. C. Kapteyn, and M. M. Murnane. Intracavity pulse-duration measurements in a sub-10fs Ti:sapphire laser. In *Proceedings of the conference on Ultrafast Phenomena*, May 1994.